THE UNIVERSITY OF CHICAGO

THE ROLE OF SURFACE CHEMISTRY IN THE SHEAR JAMMING OF DENSE SUSPENSIONS

A DISSERTATION SUBMITTED TO
THE FACULTY OF THE DIVISION OF THE PHYSICAL SCIENCES
IN CANDIDACY FOR THE DEGREE OF
DOCTOR OF PHILOSOPHY

DEPARTMENT OF CHEMISTRY

BY
NICOLE M. JAMES

CHICAGO, ILLINOIS
MARCH 2019

To my high school chemistry teacher, Graham Dey.

"The crucial challenge is to learn how to read critically, analyze data, and formulate ideas–and most of all to enjoy the intellectual adventure enough to be able to do them easily and often." —Fareed Zakaria, *In Defense of a Liberal Education*

CONTENTS

LIST OF FIGURES vii

ACKNOWLEDGMENTS ix

ABSTRACT xi

1 INTRODUCTION 1
1.1 Particle Suspensions 2
1.2 Shear Thickening and Shear Jamming 4
1.3 Wyart-Cates Model 10
1.4 Thesis Overview 11
References 14

2 GENERAL METHODOLOGY 20
2.1 Rheology 20
2.1.1 Introduction to Steady State Shear Rheology 20
2.1.2 Rheology of Dense Suspensions: Avoiding Experimental Artifacts . . 23
2.2 Suspension Preparation 28
2.2.1 Preparing Small Quantities of Suspension with Precise ϕ 28
2.2.2 Preventing Particle Sedimentation 30
2.2.3 Washing and Drying Particles for Suspension Preparation 30
2.3 Generating a State Diagram 31
2.3.1 Fitting the Wyart-Cates Model 32
2.3.2 Solving for the State Diagram Boundaries 37
References 39

3 HYDROGEN BONDING ELICITS SHEAR JAMMING OF DENSE SUSPENSIONS 41
3.1 Introduction 41
3.2 Results and Discussion 42
3.3 Conclusions 56
3.4 Methods 57
3.4.1 Particle Synthesis 57
3.4.2 Suspension Preparation 57
3.4.3 Tensile Test Protocol 58
3.4.4 Steady State Rheology 59
3.4.5 State Diagram Preparation 59
3.4.6 AFM Procedure 59
References 61

4 TUNING INTERPARTICLE HYDROGEN BONDING IN SHEAR-JAMMING SUSPENSIONS: KINETIC EFFECTS AND CONSEQUENCES FOR TRIBOLOGY AND RHEOLOGY 65
4.1 Introduction 65

4.2 Results and Discussion 66
4.3 Conclusions 75
References 77

5 DISCONTINUOUS SHEAR THICKENING AND SHEAR JAMMING IN ANISOTROPIC SYSTEMS 80
5.1 Introduction 80
5.2 Results and Discussion 82
5.3 Conclusion 88
References 90

6 CONCLUSION 94
6.1 Summary 94
6.2 Outlook 97
References 99

LIST OF FIGURES

1.1 Highly non-Newtonian fluid mixtures 2
1.2 Shear-induced compression in the bulk 4
1.3 Lubrication forces between particles in a suspension 5
1.4 Discontinuous shear thickening: Shear rate vs. shear stress visualization 6
1.5 Cracking and fracture of a shear jammed cornstarch suspension 7
1.6 Jamming of frictionless and frictional hard spheres 8
1.7 Empirical determination of the shear jamming state diagram for cornstarch in water/glycerol 9
1.8 Mechanistic schematic of frictional shear thickening 10
1.9 State diagram developed using the Wyart-Cates model 12

2.1 Shear stress and strain 21
2.2 Rheology geometries 22
2.3 Manipulating the suspending solvent to avoid the rheometer rate limit 24
2.4 Complications in using timepoint data to determine DST suspension shear protocols 25
2.5 Hysteresis loops to determine steady state shear profile 26
2.6 Stress-controlled versus rate-controlled measurements for DST and SJ suspensions 27
2.7 Example flow curves and fitting from the Wyart Cates model 33
2.8 Experimentally-obtained flow curves for Wyart-Cates analysis 35
2.9 Shear thinning may complicate determination of the lower η plateau 36
2.10 Wyart-Cates model, stess versus rate flow curves 37
2.11 State diagram generated using the Wyart Cates Model 38

3.1 Particle characterization and flow curves 42
3.2 Tensile test for shear jamming 44
3.3 High-speed ultrasound imaging of PMMA/ITA suspension dynamics. 45
3.4 Steady-state rheology for PMMA/ITA suspensions with urea as a function of ϕ . 46
3.5 Shear jamming dependence on hydrogen bonding 48
3.6 Complete state diagram for PMMA/ITA with 0 M and 6 M urea. 49
3.7 The effect of aprotic solvents and ionic strength on shear jamming 51
3.8 Steady state rheology of cornstarch as a function of solvent composition 52
3.9 Connecting particle surface chemistry and interparticle friction 54
3.10 Steady-state rheology for 3-6μm diameter glass beads 55

4.1 Methodological schematic 66
4.2 Atomic force microscopy friction measurements 68
4.3 Time-dependent urea sorption and rheology 70
4.4 Atomic force microscopy of adhesion with and without urea present 74

5.1 Silica particle shape characterization 82
5.2 Rheological flow curves for silica particles of increasing aspect ratio 83
5.3 ϕ_0 and ϕ_m for silica particles of increasing aspect ratio 86
5.4 State diagrams for silica rods of increasing aspect ratio 87

6.1 Computer-generated representation of the chemical perspective of how particle surface chemistry influences flow behavior 96

ACKNOWLEDGMENTS

There are many people who played integral roles in this thesis and in my graduate school career. I would first like to thank my research advisor, Heinrich Jaeger. Heinrich is an incredible mentor, and he has made me a better scientist than I would have imagined I could ever be. I feel very fortunate to have had his guidance and support. Heinrich has fostered a friendly and welcoming lab environment, made better by everyone who is a part of it. Ivo Peters, Scott Waitukaitis, Qin Xu, Yifan Wang, Victor Lee, Endao Han, Kieran Murphy, Leah Roth, Jelani Hannah, Melody Lim, Rebecca Cheng, Liang Zhao, Arthur Mackeith, Isaac Harris, Jon Kruppe, Medha Goyal, and Huayue Xue: thank you all. Special thanks to Mike van der Naald for carrying the torch. The Nagel lab often feels like a part our group as well, and I would like to thank Sid Nagel, Irmgard Bischofberger, Michelle Driscoll, and Thomas Videbaek.

I would also like to thank my collaborators from ETH Zurich: Lucio Isa, Chiao-Peng Hsu, and Nicholas Spencer. Thank you for the interesting data and discussions!

My parents, Bob and Shelley James, and my extended family deserve thanks for their love and support. My mother fought hard to make sure I had opportunities to learn. My grandparents, Rita and Larry Dalton, are a lesson in unconditional love. I would especially like to thank my uncle Craig for his early encouragement to go to college.

I was fortunate to have many excellent teachers without whom I would not be here. My middle school teachers, Dean Deters and Doug Dougan, laid the groundwork to eventually convince me that I could–and should–go to college. This baton was picked up by all of my high school teachers, but special thanks goes to Kara McGuirk, Michael Lampert, Steve Holman, and Graham Dey, without whom I would not be a scientist. At Whitman College, I would like to thank Susan Babilon, Frank Dunnivant, Marion Goetz, Mark Juhasz, Allison Calhoun, Steve Hughes, Amy Blau, Dalia Rokhsana Biswas, and especially Tim Machonkin. Thank you for teaching me, inspiring me, and supporting me.

At the University of Chicago, I would like to thank Greg Engel for shaping how I ap-

proached navigating a research university. I would also like to thank Andrei Tokmakoff and Thomas Witten for their interest in and perspectives about my research. Bozhi Tian has tirelessly supported me in my career goals, for which I am deeply thankful. I would also like to thank John Phillips, Qiti Guo, and Justin Jureller for keeping everything running. Graduate school would have been much harder without you.

A big part of my life at the University of Chicago has involved teaching. Not every day spent in lab feels productive, but every day I spent teaching did. Being able to participate in both research and teaching every year has been a privilege. The Collaborative Learning in Chemistry program allowed me to formalize, test, and improve my teaching skills, and gave me the opportunity to work alongside some excellent people. Thank you to Britni Ratliff and Elizabeth Chandler for teaching me how to teach, and thank you to Nick Antos, Saieesh Rao, Jonathan Michelsen, and Ade Ayoola for being in the trenches with me.

Without the support and camaraderie of friends, I would not be here. Melanie Altaras: thank you for over 15 years of support and friendship. Sergio Garcia: thank you for always being there. Thank you to Jackson Cahn, Peter Griffin, Kayla Foster, Nathan Neff-Mallon, Johnny Zimmerman, Matt Goldfogel, Andrew Molina, Jesus Vasquez, Gab Arrowood, Clark van Horne, Arianna Cortesi, Brandon Fennell, Devin Petersen, Andy Ernst, Kieran Burkholder, Mzuri Handlin, E. W. Malachowsky, Moira Flanagan, Sara Massey, Dan Micheroni, Elizabeth Bain, and Michael Lueckheide. Mzuri Handlin, Tom Kuntz, John Otto, Tom Videbaek, and Kieran Murphy: thanks for the compassion, beer, and board games.

I struggle to find the words for how to thank my partner, Dmitriy Dolzhnikov. Dmitriy has always been immensely understanding, patient, compassionate, supportive, and loving. When I was (over)working in the lab and the classroom, it was Dmitriy behind the scenes who kept everything else running smoothly. I could not have imagined the selflessness he demonstrated when I broke both my hands as I started writing this thesis. In every way, he makes my life better. Спасибо, я тебя люблю.

To anyone reading this not named here: I'm sorry, you should be.

ABSTRACT

Suspensions are mixtures of solid particles in a fluid. If a suspension is dilute, the particles merely elevate the Newtonian viscosity. For dense suspensions, however, staggering and sometimes catastrophic effects can be observed, such as discontinuous shear thickening (DST) and shear jamming (SJ). In DST, the suspension viscosity jumps discontinuously, often by orders of magnitude, at a critical shear rate. In SJ, the viscosity can fully diverge under shear, leading to reversible, shear-induced solidification. These behaviors arise from particles being pushed into direct contact by shear, at which point they interact frictionally. This can form a particle network that provides solid-like qualities. However, phenomenological models did not clearly explain why aqueous cornstarch suspensions demonstrate this behavior while seemingly similar systems do not. In this thesis, we show that what differentiates aqueous cornstarch suspensions is the capacity to form interparticle hydrogen bonds. This elevates the interparticle friction and provides rigidity to the particle network. Armed with this knowledge, we demonstrate that other systems can easily be designed to display strong DST and SJ, provided one pays close attention to the chemistry of the solvated particle-particle interface. Extending these findings, we explore a unique repercussion of how hydrogen bonding elevates interparticle friction: adhesive interactions. Adhesion can be clearly observed in SJ systems, and works to increase friction. So far, adhesion has been neglected in simulations and its incorporation will likely aid in the quantitative agreement between simulations and experiments. Finally, we apply these findings to design a novel system with enhanced DST and SJ at reduced particle concentration. We show that concentrations necessary for DST and SJ are sensitively dependent on particle aspect ratio, which can be a valuable tool in tuning DST and SJ behavior for dynamically responsive material applications. Overall, this work integrates the chemical perspective of solvated solid interfaces with granular and soft matter physics. In this way we provide a framework to anticipate and prevent unwanted flow behaviors in processing applications, and contribute design recommendations for how to engineer DST and SJ for dynamically-responsive materials.

CHAPTER 1

INTRODUCTION

The principle states of matter are solid, liquid, and gas. Liquids and gases are fluids, which flow under applied stress in accordance with their viscosity. Solids may deform under shear in accordance with their shear modulus. The transitions between these states are typically controlled by temperature or pressure, which induce changes in how the constituent molecules are located with respect to one another. However, when materials are formed by combining matter of different phases, rich, counter-intuitive behaviors can arise. Take foams as an example: when an ultra-low-viscosity gas is mixed into a low-viscosity fluid, a foam can be formed that has solid-like attributes, holding its own shape under gravity (see Figure 1.1A). Alternatively, hard solid particles can be mixed into a fluid, forming a particle suspension. The material characteristics of these particle suspensions can depend sensitively on the nature of the particles and how they are handled: paint is a particle suspension designed to be higher in viscosity at rest to prevent drips, but to be lower in viscosity when brushed onto a surface to allow easy, even coverage. Conversely, another particle suspension, cornstarch in water, behaves fluid-like when handled gently but reacts as a solid when handled rapidly such as by punching or jumping (see Figure 1.1B).

Suspensions of particles in a fluid are highly diverse. The particles can be as small as several nanometers, or as big as hundreds of microns. The fluids can be pure or mixtures. Particles may be irregular in size or shape, deformable or hard, porous or solid. The bulk properties of the resulting concentrated suspension will depend sensitively on the delicate balance of the energies and properties associated with these characteristics. This often results in industrial hardship with the processing of these materials. However, it also provides rich opportunities for developing materials that are responsive to their environment. In this work we will focus on suspensions of great interest for dynamically responsive protective wear [2, 3]. Developing materials for these applications requires a detailed understanding of the relevant particle and solvent characteristics. This work examines these issues to

Figure 1.1: A. Whipped cream on hot chocolate. Whipped cream is a foam formed by mixing air into cream. Despite being comprised of fluids, the foam is solid-like at low stresses, allowing it to maintain its shape under gravity. Yet the foam still flows easily under shearing or extrusion. Image from pixabay. B. A concentrated suspension of cornstarch in water. At low shear stresses, the suspension behaves as a fluid. However, high shear forces transform the material into a solid that can support weight, such as a person running across the surface. Image from ref. [1].

provide a fundamental scientific understanding of the effect, as well as to explore parameters through which these effects can be tuned. These findings provide tools for optimizing the material response for both industrial processing needs and dynamically responsive material applications.

1.1 Particle Suspensions

Particle suspensions are dispersions of solid particles in a solvent. The suspending solvent is typically a simple Newtonian liquid or solution. If the solid particles are Brownian (diameter $d \lesssim 1\mu$m), the mixture may be referred to as a colloidal dispersion. If the particles are non-Brownian ($d \gtrsim 1\mu$m), the mixture is generally referred to as a suspension. However, this boundary is not clear cut and these terms are sometimes used interchangeably in the literature for particles near 1μm in size, such as cornstarch ($d \approx 15\mu$m).

The presence of solid particles in a simple, Newtonian solvent alters the viscosity of the mixture. This was first described by Einstein [4], who showed that the viscosity of the

suspension η is greater than that of the suspending solvent viscosity η_0 due to the enhanced energy dissipation from the rotation of the suspended particles. This can be described as

$$\eta = \eta_0 \cdot (1 + \frac{5}{2}\phi), \tag{1.1}$$

where ϕ is the volume fraction of solid particles: $\phi = \frac{V_{\text{particles}}}{V_{\text{particles}}+V_{\text{solvent}}}$. This equation is valid for suspensions of spherical particles that are sufficiently dilute, such that particle interactions can be neglected. When suspensions become concentrated enough that long-range particle interactions through the suspending medium cannot be ignored, higher order terms must be taken into account [5, 6].

At very high packing fractions, there is insufficient space for particles to move and the system becomes solid-like, or "jammed." The jamming point can vary depending on the nature or shape of the particles, but for randomly-packed, frictionless hard spheres, the jamming packing fraction ϕ_J is $\phi_{\text{RCP}} \approx 0.64$. The concept of jamming was originally developed for dry grains [7], but has been applied broadly to describe glass formation [8, 9], gelation [10], and recently, suspensions. This provides a phase transition framework to explain the tendency of a suspension to jam if sufficiently many particles are present.

For a concentrated suspension, the suspension viscosity η can be described relative to the particle jamming packing fraction ϕ_J through the Krieger-Dougherty relation [11]

$$\eta = \eta_0 \cdot (1 - \frac{\phi}{\phi_J})^{-\beta}, \tag{1.2}$$

where β is a parameter that depends on the particle characteristics [12]. The original Krieger-Dougherty formulation employed $\beta = 2.5\phi_J$, which upon binomial expansion recovers the Einstein equation (Equation 1.1). However, work by Maron and Pierce [13], which adopts $\beta = 2$, often better fits experimental results of moderately concentrated suspensions. Thus, β is typically taken to be close to or equal to 2.

These models predict that the presence of particles shifts the Newtonian viscosity to a

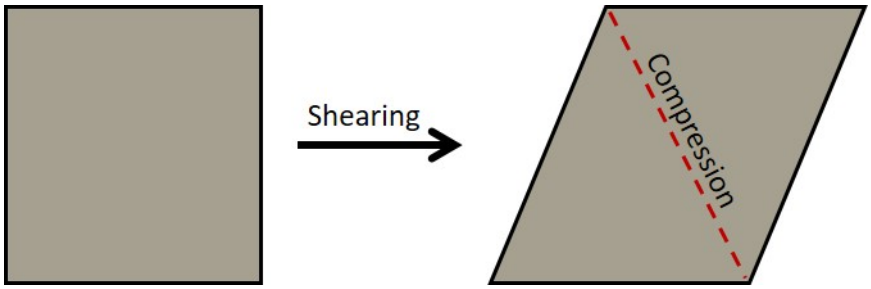

Figure 1.2: Shearing an object introduces a compressive axis in the bulk.

higher value. However, experiments show that in addition to this, dense suspensions are highly non-Newtonian in the sense that the viscosity not only depends on ϕ as shown in Equation 1.2, but also on the intensity of the applied shear. In particular, dense suspensions can exhibit viscosity decreases [14], increases [15], or solidification [15] as the imposed shear stress or rate increases. These effects are known as shear thinning, shear thickening, and shear jamming, respectively. Of primary interest to this work are shear thickening and shear jamming, discussed in the next section.

1.2 Shear Thickening and Shear Jamming

Shear thinning, arising from shearing particle aggregates that form due to interparticle attractions [16, 17], is conceptually simple: particle agglomerates must be torn apart for the suspension to flow. On the other hand, shear thickening is strikingly counter-intuitive: the more the system is sheared, the more resistive to flow it becomes [15]. Yet, it is ubiquitous in concentrated suspensions of hard spheres [17]. Mild shear thickening is typically observed in moderately concentrated suspensions of hard spheres, *e.g.* $\phi \approx 30\%$. This has been theorized to be due to the shear-driven formation of hydroclusters [18].

When suspensions are sheared, the compressive axis (see Figure 1.2) pushes particles together. For particles to approach each other, the fluid between them must be driven away, as depicted in Figure 1.3. As the interparticle distance h becomes small, the so-called lubrication forces required to squeeze out the fluid become quite high, described by

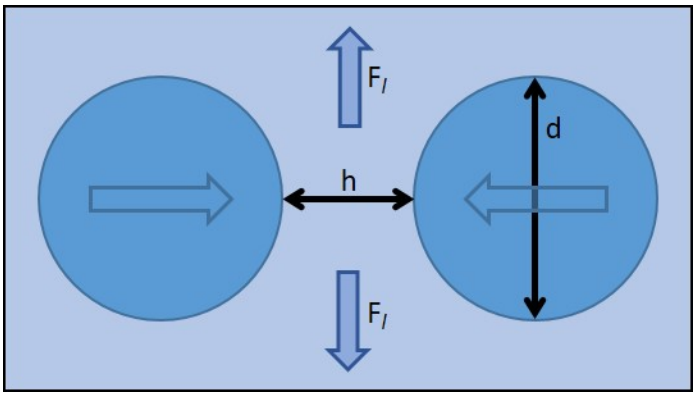

Figure 1.3: Pushing particles together in a fluid medium requires squeezing out the interstitial fluid. The forces F_l required to do so are called lubrication forces, and depend on the suspending solvent viscosity, interparticle distance h, and particle diameter d.

$$F_l = \frac{6\pi\eta d^2}{h}, \tag{1.3}$$

where d is the particle diameter [19]. An important early model for shear thickening was the hydrocluster model [18, 20, 21]. This model suggests that shearing forces particles into clusters along the compressive axis. These clusters are reversible yet somewhat stable since the lubrication force is not directional and a high force would also be required to pull the particles apart again. These transient clusters have an elevated packing fraction resulting in increased fluid stress and thereby increased energy dissipation and increased viscosity [21]. Experiments and simulations suggest that this mechanism may certainly describe mild shear thickening [18, 20, 12, 22, 23, 24, 25, 26, 27]. However, concentrated suspensions (*e.g.* $\phi \gtrsim 30\%$) often show much more significant, discontinuous jumps of several orders of magnitude in viscosity as a function of shear rate. A discontinuous jump with respect to shear rate corresponds to a slope of 1 on a log-log plot of viscosity vs. shear stress (as shown in Figure 1.4). This is known as discontinuous shear thickening (DST), a viscosity increase too severe for the hydrocluster model alone to explain [28, 40, 29, 1, 30, 31, 27, 32]. Furthermore, some suspensions can even undergo a reversible, shear-induced transition to a

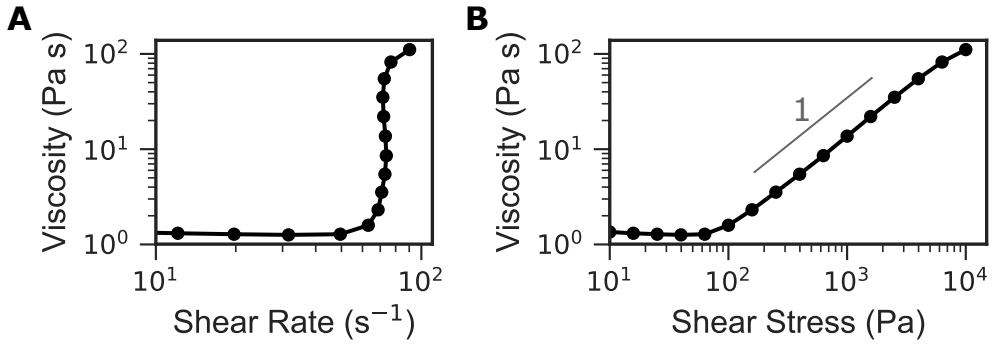

Figure 1.4: A. Discontinuous shear thickening for a suspension of poly(methylmethacrylate)/itaconic acid microspheres, plotted as a function of shear rate. B. The same data as in A, plotted as a function of shear stress. Visualized in this manner, discontinuous shear thickening corresponds to a slope of 1, indicated in gray.

solidlike state, where cracking and fracture occur. This is known as shear jamming (SJ).[1] This is shown in Figure 1.5 for a prototypical suspension: cornstarch in water.

To explain the severe viscosity increases observed in DST and SJ, insight can be taken from jamming–the process that provides rigidity for granular packings [7]. For a packing of particles above a critical packing fraction ϕ, there is insufficient space for particles to flow around each other. Thus, the packing behaves as a rigid, jammed solid. The packing fraction at which this occurs is known as the jamming packing fraction ϕ_J, also called the jamming point. For frictionless spheres, the jamming point $\phi_J = \phi_0$ is typically close to $\phi_{\mathrm{RCP}} \approx 0.64$. A state diagram depicting this for rigid spheres is shown in Fig 1.6A: if the system is prepared at $\phi < \phi_0$, the system flows. If the system is prepared at $\phi > \phi_0$, the system is arrested and does not flow. If the particles are deformable, shearing the jammed, $\phi > \phi_0$ suspension may result in yielding and in this way the system may become unjammed.

For frictionless particles (Figure 1.6A), there is no route to achieve a jammed state if $\phi < \phi_0$. However, if the particles are frictional, particles may be sheared into an anisotropic particle network of force chains that span the system and provide rigidity, resulting in jamming at packing fractions $\phi_J = \phi_m$ below that of the frictionless ϕ_0 [34]. This provides a route to jamming at even lower packing fractions, but only if shear is applied. This shear-

1 Some literature conflates DST and SJ. In this work, we differentiate between the flowing DST state and the solid-like, arrested SJ state that has a nonzero shear modulus.

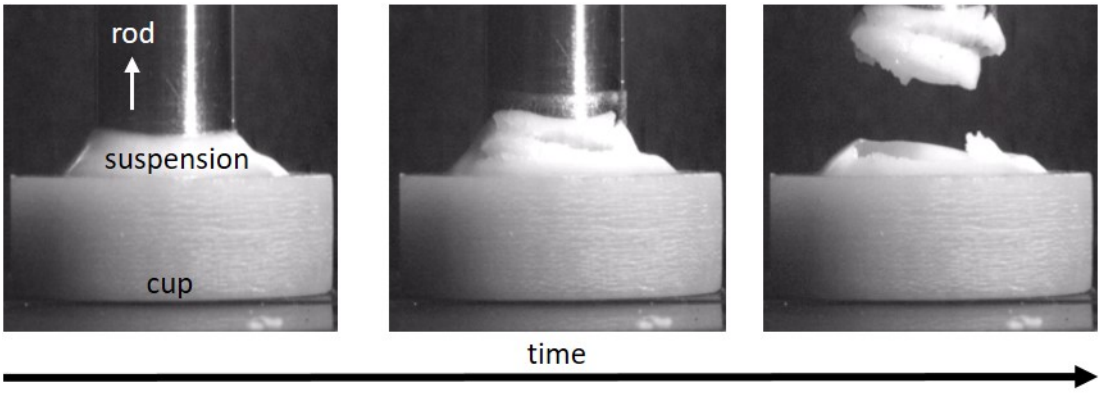

Figure 1.5: Shear jamming suspensions exhibit solidlike behavior such as cracking and fracture, such as shown here for a suspension of cornstarch in water/glycerol under tensile stress. Still frames are shown here from a video of a rod embedded in a cup of cornstarch suspension being withdrawn. As the rod is withdrawn, the suspension jams, cracks, and fractures into two pieces. Images reproduced from ref. [33]
.

driven jamming is depicted as the green region in Figure 1.6B, and appears to only be experimentally accessible for frictional particles.[2]

Shear jamming of dry grains thus describes a scenario where a packing could be prepared at $\phi < \phi_m$ which can flow at low stresses, but above a certain stress can suddenly become rigid and behave like a solid. The similarities between this behavior and the thickening and jamming behaviors observed in dense suspensions suggests the possible importance of frictional interparticle interactions in suspensions.

Indeed, numerous experiments [38, 39, 40, 30, 41, 31, 42] and simulations [28, 29, 43, 44, 45] have indicated that interparticle friction plays a strong role in DST. In addition, recent work has mapped out the lower bound of the SJ state diagram for cornstarch in water/glycerol suspensions [37], as shown in Figure 1.7.

Thus, a general conceptual understanding has developed [32] (depicted in Figure 1.8), whereby at low shear stresses, particles are lubricated and interact as though they are frictionless. As particles are sheared close together, the continuum mechanics description that

2 For finite systems, a shear jamming regime is available in frictionless systems as well [35, 36], but in such a case the packing fractions at which shear jamming is possible are so close to ϕ_0 as to leave the effect experimentally negligible.

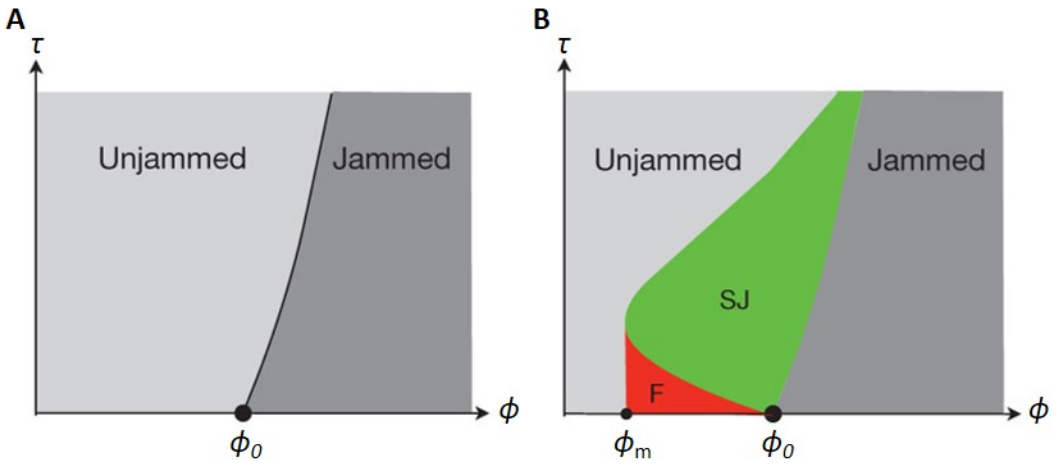

Figure 1.6: A. The jamming state diagram for frictionless dry grains. For infinitely hard spheres, the curve between the unjammed and jammed regimes becomes a vertical line. This is a simplified version of the state diagram developed by Liu and Nagel [7], image adapted from Bi *et al.* [34]. B. The jamming state diagram for frictional dry grains, which includes an additional route to achieving a jammed state: applied shear. This route gives rise to the shear jammed (SJ) regime, depicted in green. Bi *et al.* described the shear stresses approaching this state (red) as the fragile (F) regime, where intermediate behavior such as shear thickening may occur. Image adapted from Bi *et al.* [34].

describes lubrication forces breaks down, either due to surface roughness or because distances become on the scale of scale of molecules. As a result, the lubrication layer breaks and particles are effectively in contact, where they can experience friction. Then, force chains of particles stabilized by these frictional interactions can form. At particular packing fractions or stresses, these force chains may be constantly forming and buckling, imparting an improved resistance to flow which manifests as strong shear thickening such as DST. At higher packing fractions or stresses, these force chains may support applied stresses and form a network in the bulk, resulting in a stress-induced solidification that relaxes when the applied stress is removed and particle force chains relax. This is hypothesized to result in the observed reversible shear jamming. A quantitative model to describe this was pioneered by Matthieu Wyart and Michael Cates, and is known as the Wyart-Cates model [46]. This model is described in the following section. Subsequent models adapting a modified Wyart-Cates model have been developed [30, 45]. In this work we focus on the original form of the

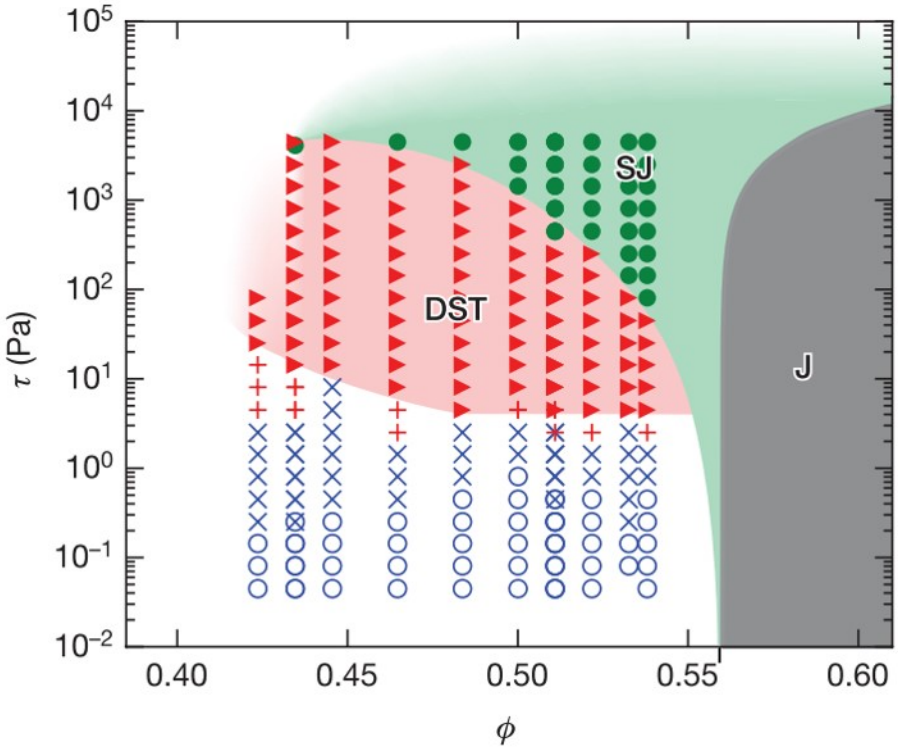

Figure 1.7: Empirical determination of the lower bound of the shear jamming state diagram for suspensions of cornstarch and water. The jammed (J) regime (gray) was determined experimentally as the packing fraction above which flowing suspensions could not be prepared. The SJ regime (green) was determined by the impact of a steel sphere with the suspension surface. The DST regime (red) was determined by steady state rheology. Data points indicate experimental measurements; blue markers indicate either Newtonian (∘) or mild shear thickening (x). Figure reproduced from Peters *et al.* [37].

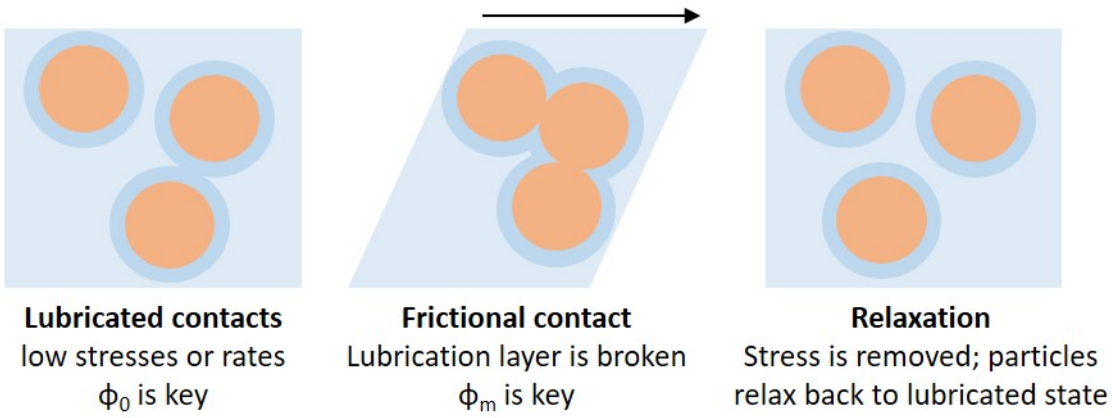

Figure 1.8: Mechanistic schematic of frictional shear thickening: At rest, particles are covered in solvent lubrication layers that prevent particles from coming into direct contact. The particles thus interact frictionlessly and the frictionless jamming point ϕ_0 governs the flow behavior. When the suspension is sheared, particles may be forced into close proximity and the lubrication layers rupture as particles come into direct contact. The particles then interact frictionally, and therefore the frictional jamming point ϕ_m governs the flow behavior. When the sheared is ceased, particles relax back into the lubricated (frictionless) state.

Wyart-Cates model, as it fits the data with the fewest parameters.

1.3 Wyart-Cates Model

The Wyart-Cates model [46] posits that the particles start off at rest or at low shear in the lubricated and thus frictionless state. Therefore, the jamming packing fraction ϕ_J is that of the frictionless case, distinguished as ϕ_0. As particles are sheared into contact, at a critical stress the lubrication barrier between particles is broken and particles form direct contacts, at which point they behave frictionally. The relevant jamming packing fraction thus suddenly switches from the frictionless ϕ_0 to the frictional ϕ_m. Because $\phi_m < \phi_0$, in this way the system can find itself sheared into a jammed state.

In this way, the system is transitioning between two Krieger-Dougherty relations (Equation 1.2), one for the frictionless, low-stress case:

$$\eta = \eta_0 \cdot (1 - \frac{\phi}{\phi_0})^{-\beta}, \tag{1.4}$$

and one for the frictional high-stress case:

$$\eta = \eta_0 \cdot (1 - \frac{\phi}{\phi_m})^{-\beta}. \tag{1.5}$$

The cross over between these two states is determined by the average number of particles in frictional contact, given by

$$f(\tau) = 1 - e^{-\frac{\tau}{\tau^*}}, \tag{1.6}$$

where τ^* is the critical stress corresponding to the breakdown of the particle lubrication layer. Based on this formulation, at $\tau = \tau^*$, the fraction of particles in frictional contact is $1 - e^{-1} \approx 63\%$. Using this critical stress to transition between the frictional and frictionless regimes, we can reformulate a Krieger-Dougherty relation with a stress-dependent effective jamming packing fraction, $\phi_J = \phi_{\text{eff}}$:

$$\eta = \eta_0 \cdot (1 - \frac{\phi}{\phi_{\text{eff}}})^{-\beta}, \tag{1.7}$$

where ϕ_{eff} is given by

$$\phi_{\text{eff}} = \phi_m(1 - e^{-\frac{\tau}{\tau^*}}) + \phi_0(e^{-\frac{\tau}{\tau^*}}). \tag{1.8}$$

At the low and high stress limits, this recovers the relevant ϕ_J: as $\lim_{\tau \to 0} \phi(\tau) = \phi_0$, and $\lim_{\tau \to \infty} \phi(\tau) = \phi_m$. In this way, the Wyart-Cates model describes the shear-induced cross over between these two states, and can be used to generate a state diagram such as the example diagram shown in Figure 1.6B.

1.4 Thesis Overview

The primary goal of this work was to address the issue: if the Wyart-Cates model for shear induced jamming is so general, depending only on the system's τ^*, ϕ_0, and ϕ_m, why do

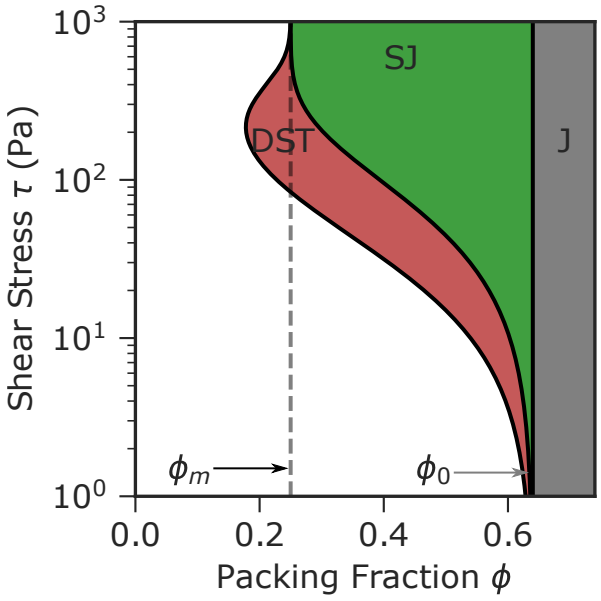

Figure 1.9: An example state diagram generated using the Wyart-Cates model with frictional jamming point $\phi_m = 0.25$, frictionless jamming point $\phi_0 = 0.64$, and critical stress $\tau^* = 100$ Pa. The green SJ region indicates shear jamming, the red DST region indicates discontinuous shear thickening, and the gray J region indicates jammed at rest.

so few experimental systems demonstrate this behavior? While DST behavior was quite general and common [17], experimental observations of reversible, shear-induced jamming were primarily limited to suspensions of cornstarch particles in water. Simply put, this work answers the question: what is special about cornstarch? In particular, What are the molecular-scale explanations that give rise to this behavior?

Chapter 2 introduces the experimental methods central to this work. Chapter 3 employs these methods to show that shear jamming can be elicited in non-starch systems by controlling the particle surface chemistry and suspension solvent characteristics to facilitate interparticle hydrogen bonding. This provides a chemical tool through which to tune interparticle friction and thus vary ϕ_0 and ϕ_m such that ϕ_m is appreciably smaller than ϕ_0, in order to allow for SJ under experimentally relevant conditions. Chapter 4 explores a unique repercussion of hydrogen bonding as a factor in the friction coefficient: that the interparticle interaction is also adhesive in nature. This work characterizes how stress-induced adhesion between particles that is reversible under kT couples with the friction coefficient to give rise

to enhanced shear jamming. Chapter 5 employs these findings to prepare a synthetic shear jammable system of variable shape. This work holds the particle and solvent chemistry constant and explores the role of particle shape, notably aspect ratio, as a parameter for tuning the particle loadings necessary for shear jamming. Chapter 6 summarizes the trajectory of this work and how it has developed the conceptual, foundational understanding of shear jamming as a unique characteristic of dense suspensions, and explored control parameters by which these systems can be engineered and optimized for enhanced industrial processing, and dynamically responsive material applications.

BIBLIOGRAPHY

[1] Eric Brown and Heinrich M Jaeger. Shear thickening in concentrated suspensions: phenomenology, mechanisms and relations to jamming. *Reports on Progress in Physics*, 77:046602, 2014.

[2] Colin D Cwalina, Charles M Mccutcheon, Richard D Dombrowski, and Norman J Wagner. Engineering enhanced cut and puncture resistance into the thermal micrometeoroid garment (TMG) using shear thickening fluid (STF) – Armor$^{\text{TM}}$ absorber layers. *Composites Science and Technology*, 131:61–66, 2016.

[3] Abhijit Majumdar, Bhupendra Singh Butola, and Ankita Srivastava. Optimal designing of soft body armour materials using shear thickening fluid. *Materials and Design*, 46:191–198, 2013.

[4] A Einstein. Über die von der molekularkinetischen Theorie der Wärme geforderte Bewegung von in ruhenden Flüssigkeiten suspendierten Teilchen. *Annalen der Physik*, 322(8):549–560, 1905.

[5] G K Batchelor. Brownian diffusion of particles with hydrodynamic interaction. *Journal of Fluid Mechanics*, 74:1–29, 1977.

[6] Robin C Ball and Peter Richmond. Physics and Chemistry of Liquids Dynamics of Colloidal Dispersions. *Physics and Chemistry of Liquids*, 9:99–116, 1980.

[7] Andrea Liu and Sidney R. Nagel. Jamming is not just cool anymore. *Nature*, 396:21–22, 1998.

[8] Corey S O'hern, Leonardo E Silbert, Andrea J Liu, and Sidney R Nagel. Jamming at zero temperature and zero applied stress: The epitome of disorder. *Physical Review E*, 68:011306, 2003.

[9] Andrea J Liu and Sidney R Nagel. The Jamming Transition and the Marginally Jammed Solid. *Annual Review of Condensed Matter Physics*, 1:347–369, 2010.

[10] P N Segrè, V Prasad, A B Schofield, and D A Weitz. Glasslike Kinetic Arrest at the Colloidal-Gelation Transition. *Physical Review Letters*, 86:6042–6045, 2001.

[11] Irvin M Krieger and Thomas J Dougherty. A Mechanism for Non-Newtonian Flow in Suspensions of Rigid Spheres. *Transactions of the Society of Rheology*, 3:137–152, 1959.

[12] John F Brady. The rheological behavior of concentrated colloidal dispersions. *The Journal of Chemical Physics*, 99:567–581, 1993.

[13] Samuel Maron and Percy Pierce. Application of Ree-Eyring Generalized Flow Theory To Suspensions Of Spherical Particles. *Journal of Colloid Science*, 11:80–95, 1956.

[14] C G De Kruif, E M F Van Iersel, A Vrij, and W B Russel. Hard sphere colloidal dispersions: Viscosity as a function of shear rate and volume fraction. *Journal of Chemical Physics*, 83:4717–4725, 1985.

[15] H A Barnes. Shear-Thickening ("Dilatancy") in Suspensions ofNonaggregating Solid Particles Dispersed in Newtonian Liquids. *The Journal of Rheology*, 33:329–367, 1989.

[16] V Trappe, V Prasad, Luca Cipelletti, P N Segre, and D A Weitz. Jamming phase diagram for attractive particles. *Nature*, 411:772, jun 2001.

[17] Eric Brown, Nicole A Forman, Carlos S Orellana, Hanjun Zhang, Benjamin W Maynor, Douglas E Betts, Joseph M Desimone, and Heinrich M Jaeger. Generality of shear thickening in dense suspensions. *Nature Materials*, 9:220–224, 2010.

[18] John F Brady and Georges Bossis. The rheology of concentrated suspensions of spheres in simple shear flow by numerical simulation. *Journal of Fluid Mechanics*, 155:106–129, 1985.

[19] Elisabeth Guazzelli, Jeffrey F. Morris, and Sylvie Pic. *A Physical Introduction to Suspension Dynamics*. Cambridge Texts in Applied Mathematics. Cambridge University Press, 2011.

[20] G. Bossis and J.F. Brady. The rheology of Brownian suspensions. *Journal of Chemical Physics*, 91:1866–1874, 1989.

[21] Norman J. Wagner and John F. Brady. Shear thickening in colloidal dispersions. *Physics Today*, 62:27, 2009.

[22] R S Farr, J R Melrose, and R C Ball. Kinetic theory of jamming in hard-sphere startup flows. *Physical Review E*, 55:7203–7211, 1997.

[23] David R Foss and John F Brady. Structure, diffusion and rheology of Brownian suspensions by Stokesian Dynamics simulation. *Journal of Fluid Mechanics*, 407:167–200, 2000.

[24] Brent J Maranzano and Norman J Wagner. The effects of particle size on reversible shear thickening of concentrated colloidal dispersions. *Journal of Chemical Physics*, 114:1693, 2001.

[25] Ehssan Nazockdast and Jeffrey F Morris. Microstructural theory and the rheology of concentrated colloidal suspensions. *Journal of Fluid Mechanics*, 713(1):420–452, 2012.

[26] A Kate Gurnon and Norman J Wagner. Microstructure and rheology relationships for shear thickening colloidal dispersions. *Journal of Fluid Mechanics*, 769:242–276, 2015.

[27] Arman Boromand, Safa Jamali, Brandy Grove, and João M Maia. A generalized frictional and hydrodynamic model of the dynamics and structure of dense colloidal suspensions. *Journal of Rheology*, 62:905–918, 2018.

[28] Ryohei Seto, Romain Mari, Jeffrey F Morris, and Morton M Denn. Discontinuous Shear

Thickening of Frictional Hard-Sphere Suspensions. *Physical Review Letters*, 111:218301, 2013.

[29] Romain Mari, Ryohei Seto, Jeffrey F Morris, and Morton M Denn. Shear thickening, frictionless and frictional rheologies in non-Brownian suspensions. *Journal of Rheology*, 58:1693–1724, 2014.

[30] John R Royer, Daniel L Blair, and Steven D Hudson. Rheological Signature of Frictional Interactions in Shear Thickening Suspensions. *Physical Review Letters*, 116:188301, 2016.

[31] Cecile Clavaud, Antoine Berut, Bloen Metzger, and Yöel Forterre. Revealing the frictional transition in shear-thickening suspensions. *Proceedings of the National Academy of Sciences*, 114:5147–5152, 2017.

[32] Jeffrey F Morris. Lubricated-to-frictional shear thickening scenario in dense suspensions. *Physical Review Fluids*, 3:110508, 2018.

[33] Nicole M James, Endao Han, Ricardo Arturo Lopez De La Cruz, Justin Jureller, and Heinrich M Jaeger. Interparticle hydrogen bonding can elicit shear jamming in dense suspensions. *Nature Materials*, 17:965–970, 2018.

[34] Dapeng Bi, Jie Zhang, Bulbul Chakraborty, and R P Behringer. Jamming by shear. *Nature*, 480:355–358, 2011.

[35] Olukayode Isaiah Imole, Nishant Kumar, Vanessa Magnanimo, and Stefan Luding. Hydrostatic and shear behavior of frictionless granular assemblies under different deformation conditions. *Kona*, 30:84–108, 2013.

[36] Thibault Bertrand, Robert P Behringer, Bulbul Chakraborty, Corey S O'hern, and Mark D Shattuck. Protocol dependence of the jamming transition. *Physical Review E*, 93:012901, 2016.

[37] Ivo R Peters, Sayantan Majumdar, and Heinrich M Jaeger. Direct observation of dynamic shear jamming in dense suspensions. *Nature*, 532:214–217, 2016.

[38] François Boyer, Elisabeth Guazzelli, and Olivier Pouliquen. Unifying Suspension and Granular Rheology. *Physical Review Letters*, 107:1885301, 2011.

[39] Neil Y C Lin, Ben M Guy, Michiel Hermes, Chris Ness, Jin Sun, Wilson C K Poon, and Itai Cohen. Hydrodynamic and Contact Contributions to Continuous Shear Thickening in Colloidal Suspensions. *Physical Review Letters*, 115:228304, 2015.

[40] Nicolas Fernandez, Roman Mani, David Rinaldi, Dirk Kadau, Martin Mosquet, Hélè Ne Lombois-Burger, Juliette Cayer-Barrioz, Hans J Herrmann, Nicholas D Spencer, and Lucio Isa. Microscopic Mechanism for Shear Thickening of Non-Brownian Suspensions. *Physical Review Letters*, 111:108301, 2013.

[41] Jean Comtet, Guillaume Chatté, Antoine Niguès, Lydéric Bocquet, Alessandro Siria, and Annie Colin. Pairwise frictional profile between particles determines discontinuous shear thickening transition in non-colloidal suspensions. *Nature Communications*, 8:1–7, 2017.

[42] Chiao-Peng Hsu, Shivaprakash N. Ramakrishna, Michele Zanini, Nicholas D. Spencer, and Lucio Isa. Roughness-dependent tribology effects on discontinuous shear thickening. *Proceedings of the National Academy of Sciences*, 115(20):5117–5122, 2018.

[43] Romain Mari, Ryohei Seto, Jeffrey F Morris, and Morton M Denn. Nonmonotonic flow curves of shear thickening suspensions. *Physical Review E*, 91:52302, 2015.

[44] Christopher Ness and Jin Sun. Shear thickening regimes of dense non-Brownian suspensions. *Soft Matter*, 12:914, 2016.

[45] Abhinendra Singh, Romain Mari, Morton M Denn, and Jeffrey F Morris. A constitutive model for simple shear of dense frictional suspensions. *Journal of Rheology*, 62:405, 2018.

[46] M Wyart and M E Cates. Discontinuous Shear Thickening without Inertia in Dense Non-Brownian Suspensions. *Physical Review Letters*, 112:098302, 2014.

CHAPTER 2

GENERAL METHODOLOGY

2.1 Rheology

Rheological measurements describe how a material such as a fluid or a gel responds to an applied force. Simply put, it "answers the question, 'What happens when I poke it?'" [1]. The result can be a modulus that describes resistance to deformation, or a viscosity that describes resistance to flow. Simple materials have constant or near-constant parameters describing their deformation or flow response. Complex materials, such as suspensions of particles in a fluid, can have variable, highly nonlinear responses. Characterizing these responses requires careful, highly controlled measurements to avoid experimental artifacts. This chapter provides a basic introduction to rheology, and details its application to the flow characteristics of dense suspensions.

2.1.1 Introduction to Steady State Shear Rheology

Deformation and flow properties are defined from ideal strain- or stress-induced deformations. Shear strain γ is defined as the deformation relative to the height of the object:

$$\gamma = \frac{\Delta x}{h}, \tag{2.1}$$

as shown in Figure 2.1. Shear stress is the pressure imposed on the surface area:

$$\tau = \frac{F}{A}, \tag{2.2}$$

as shown in Figure 2.1. Viscosity η measures a fluid's resistance to flow. Viscosity is a material parameter that conveys how much stress is required to induce a given rate of strain:

$$\tau = \eta \cdot \dot{\gamma}. \tag{2.3}$$

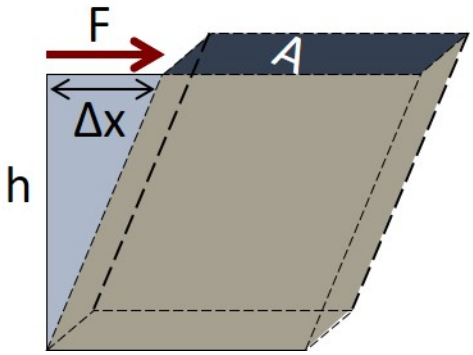

Figure 2.1: Schematic depicting shear deformating, resulting in shear stress (Equation 2.6) and shear strain (Equation 2.1). A is the surface area of the object, F is the imposed force, h is the height of the object and Δx is the induced deformation.

This equation is valid provided there are no residual, secondary flows due to fluid inertia. To ensure this is the case, all experiments must be conducted at low Reynold's number (Stoke's regime). The Reynolds number is a dimensionless parameter that provides information about if a system is viscous-dominated, where viscous dissipation causes flows to cease immediately when the applied force ceases, or inertia-dominated, where residual, secondary flows can persist after the applied force ceases due to solvent inertia. The Reynolds number R_e is simply the ratio of the inertial forces to the viscous forces:

$$R_e = \frac{\rho v L}{\eta}, \tag{2.4}$$

where ρ is the material density, v is the velocity, L is the relevant length scale, and η is the viscosity. Thus, $R_e < 1$ indicates the system is in the viscous-dominated Stoke's regime, and a $R_e > 1$ indicates the system is in the inertial regime. To avoid spurious shear thickening effects due to solvent inertia, care should be taken to ensure the system resides in the Stoke's regime for all rheological experiments.

Experimentally, viscosity can be measured by placing the fluid sample between two plates and rotating one plate, shown in Figure 2.2A. This is known as parallel plate geometry. By imposing the strain rate and monitoring the torque applied on the rotating plate (or vice-versa), the viscosity can be calculated. However, a limitation of parallel plate geometry is

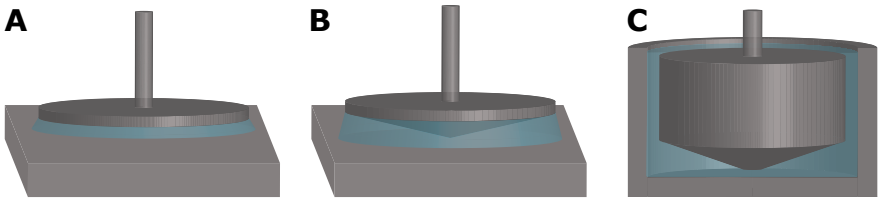

Figure 2.2: Schematic depicting the three most common rheology geometries. The fluid sample is represented in blue. A. Parallel plate geometry. B. Cone and plate geometry. C. Couette geometry, also referred to as cup-and-bob or concentric circle geometry.

that the imposed shear rate is radially dependent: fluid on the outer edge experiences a much higher shear rate than fluid close to the center of the plate. Thus, a mean shear rate can be determined by

$$\dot{\gamma}_{\text{mean}} = \frac{2}{3} \cdot \frac{\omega R}{H}, \tag{2.5}$$

where ω is the angular velocity ($\text{rad}\cdot\text{s}^{-1}$) at the edge of the plate, R is the plate radius (m), and H is the gap between plates (m). Likewise, a mean shear stress can be determined by

$$\tau_{\text{mean}} = \frac{4}{3} \cdot \frac{M}{\pi R^3}, \tag{2.6}$$

where M is the torque on the rotating plate (Nm). By calculating τ_{mean} and $\dot{\gamma}_{\text{mean}}$ in this way, an average viscosity can be found through Equation 2.3.

It is important to note, especially for sharp transitions, that the viscosity measured through parallel plate rheology is an average value for a distribution of shear rates and stresses. The cone and plate geometry, shown in Figure 2.2B overcomes this limitation by axially increasing the gap height such that the strain rate remains constant. The Couette cell, or cup-and-bob geometry, shown in Figure 2.2C, also overcomes this limitation by immersing a cylinder into the sample, and measuring the shear between the cylinder surface and the wall. However, as detailed in the following section, parallel plate geometry is often best for the rheology of dense granular suspensions.

2.1.2 Rheology of Dense Suspensions: Avoiding Experimental Artifacts

Dense suspensions present unique challenges to rheological measurements. As discussed in Section 2.1.1, parallel plate rheology has a radially dependent imposed shear. For many applications, this makes cone and plate or Couette cell geometries more attractive. However, in these geometries new challenges arise for dense suspensions.

The gap height in the center of the cone and plate geometry depends on the cone angle, but is generally on the order of tenths of a micron. Previous studies on dry granular systems indicate that the presence of the boundary introduces a depth dependence of the mechanical characteristics that vanishes after 5-8 particle layers [2]. Thus, to avoid boundary effects when measuring bulk rheological responses, the common rule of thumb is to allow for at least 10-20 particle diameters in the gap. Thus, cone and plate geometry is typically only suitable for suspensions of particles where the particle diameter is on the order of 10 nm or less.

The gap in the Couette cell geometry is on the order of 1 mm and thus avoids the boundary effect challenge for most particle systems. However, Couette cell geometry is experimentally difficult for shear jamming suspensions due to suspension solidification under the shear forces between the cylinder and the wall. In strongly shear jamming samples, insertion of the inner cylinder can prove impossible. Furthermore, Couette cell geometries often require large quantities of sample (10-20 mL), making it intractible for dense suspensions of expensive or in-house synthesized particles. For these reasons, parallel plate geometry is used for this work.

To avoid experimental artifacts, it is important to ensure the system is in the Stokes limit, lest inertially-induced residual or secondary flows increase the measured torque and thus artificially inflate the measured viscosity.[1] The system is in the Stokes regime if the Reynolds number R_e is less than 1. The general definition of the Reynolds number is given

1 A hall-mark of this sample inertia-dominated flow is that the viscosity scales as $\dot{\gamma}^{0.5}$. This is because τ scales as $\dot{\gamma}^2$ due to Newton's laws, and $\eta = \tau/\dot{\gamma}$ from Equation 2.3.

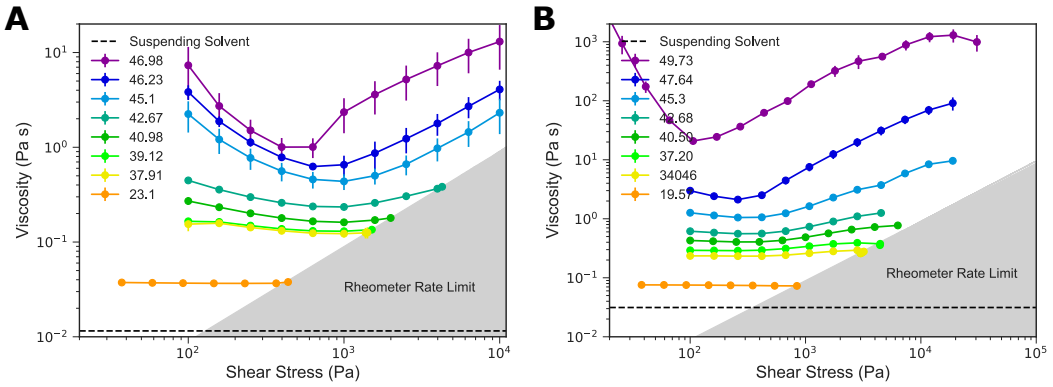

Figure 2.3: A. 500 nm silica particles suspended in 50% aqueous glycerol (v/v). For several packing fractions, the shear thickening regime is obscured by the rheometer rate limit, indicated in gray. B. The same particles as in A, suspended in 70% aqueous glycerol with 15 mM NaCl. The increased glycerol concentration elevates the suspension viscosity, and the NaCl screens interparticle charge repulsion, shifting the shear thickening regime to lower shear rates and stresses. These factors combined allow the full shear thickening regime to be visualized.

in Equation 2.4. For the specific case of steady state shear in parallel plate geometry, this becomes

$$R_e = \frac{\rho \dot{\gamma}_{\max} H^2}{2\pi R \eta}, \tag{2.7}$$

where ρ is the suspension density,[2] $\dot{\gamma}_{\max}$ is the shear rate at the edge of the plate, H is the gap height between the top and bottom plates, R is the plate radius, and η is the suspension viscosity.

In addition to the sample inertial effect, another limit on the maximum imposed shear rate is based on the instrumental limit: 40,000 s^{-1} for the Anton Paar MCR 301 model used throughout this work. If measurements run into the instrumental limit, the suspending solvent may be used to avoid the issue. Raising the suspending solvent viscosity may elevate the suspension viscosity such that lower rates are required to achieve the same shear stress. Alternatively, steps can be taken to tune the minimum shear stress required for shear thick-

2 Note that if a suspension is not density matched, the density of the suspension is not equal to the particle or solvent densities.

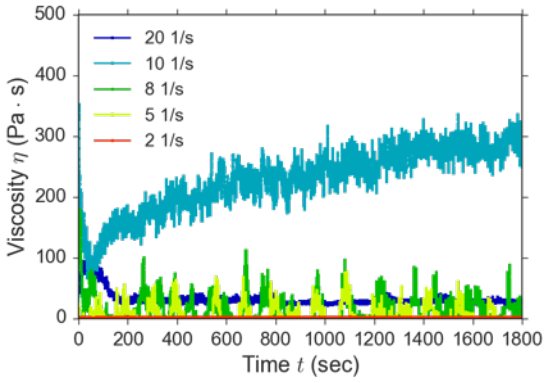

Figure 2.4: Viscosity over time at constant shear rate for a 56% suspension of PMMA/ITA particles in 69% aqueous glycerol (v/v). Data taken by summer REU fellow Rebecca Cheng.

ening τ_{min}, such as by increasing the ionic strength to shield interparticle repulsion and lower τ_{min} [3]. These strategies are shown in Figure 2.3 to aid the rheological characterization of 500 nm silica suspensions.

The lower instrumental limit is set by the torque resolution. On the Anton Paar MCR301 model, the torque resolution is 1 nN. By Equation 2.6, this corresponds to a minimum measurable τ_{mean} of $2.7 \cdot 10^{-2}$ mPa. While instrument inertia often influences lower experimental limits in transient measurements such as step tests or oscillatory rheology, this does not present challenges to steady state rheology where the system is sheared at a constant rate or stress for sufficiently long that it is able to establish a steady state.[3] However, this raises a new concern: how to be sure the waiting time is sufficiently long that a steady state has been achieved.

There are two main approaches to determining if a dense suspension has achieved a steady state on the rheometer: monitoring viscosity over time at a constant shear rate or stress, or performing hysteresis loops. For DST or SJ suspensions, fluctuations within the sample over time can make it difficult to interpret if the system has achieved a steady state by analyzing data over time (see Figure 2.4). Therefore, provided there are no reasons to expect the

3 The Anton Paar MCR 301 used in this work averages only the last 40% of data acquired during the waiting time, so transient effects from the initial setting of τ or $\dot{\gamma}$ are not included in the reported, time-averaged data point.

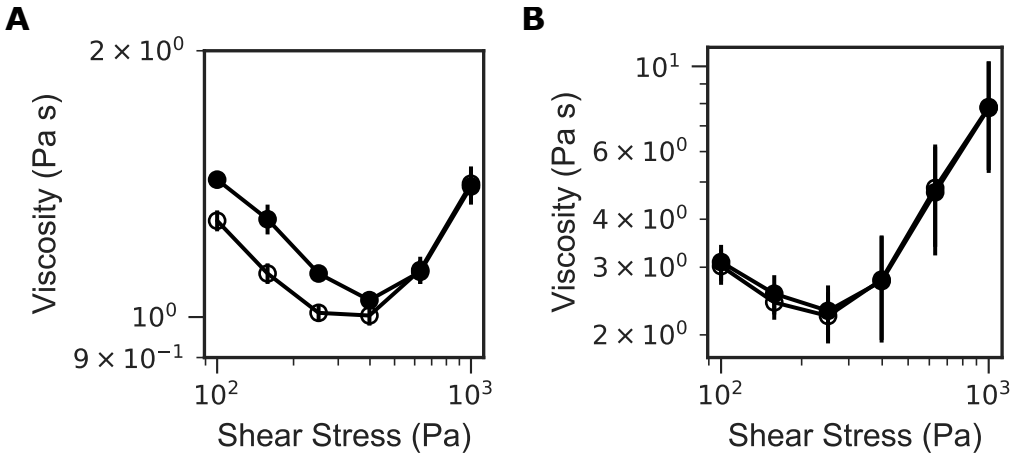

Figure 2.5: Hysteresis loops to determine shear profile waiting times to allow for the generation of a steady state for PMMA/ITA suspensions (69% aqueous glycerol (v/v)). Closed symbols indicate forward ramps, open symbols indicate backwards ramps. A. $\phi = 0.453$ suspension showing a steady state is established at high shear ($\tau > 400$ Pa), but hysteresis present at lower shear stresses ($\tau < 400$ Pa) indicating the waiting time is insufficient to establish a steady state. B. $\phi = 0.476$. No offset between the forwards and backwards ramps, indicating the waiting time is sufficient to establish a steady state over the entire τ range.

system to have a memory of prior conditions or treatment in the rheological response (*e.g.* as would a gel), performing forwards (increasing) and backwards (decreasing) ramps in shear stress or rate and determining that there is no hysteresis (see Figure 2.5) provides a facile method for confirming the waiting time is sufficient to establish a steady state.

A final note about performing rheological studies on suspensions that exhibit DST and/or SJ is one of shearing method. For Newtonian samples it is equivalent to control shear stress or shear rate, and in fact controlling the shear rate is often simpler and faster. However, because of the discontinuity in viscosity as a function of shear rate for DST suspensions (as shown in Figure 1.4), it is difficult to collect this data experimentally by controlling the shear rate. Figure 2.6 compares shear rate-controlled and shear stress-controlled data for a PMMA/ITA suspension. From Figure 2.6A, it is clear that shear stress control provides better data coverage in the shear thickening regime. Furthermore, SJ suspensions often show an initial region at the beginning of shear thickening where $d\log(\eta)/d\log(\tau)$ is slightly greater than 1, as seen by the slight "hump" or bowing of the data above the black line that

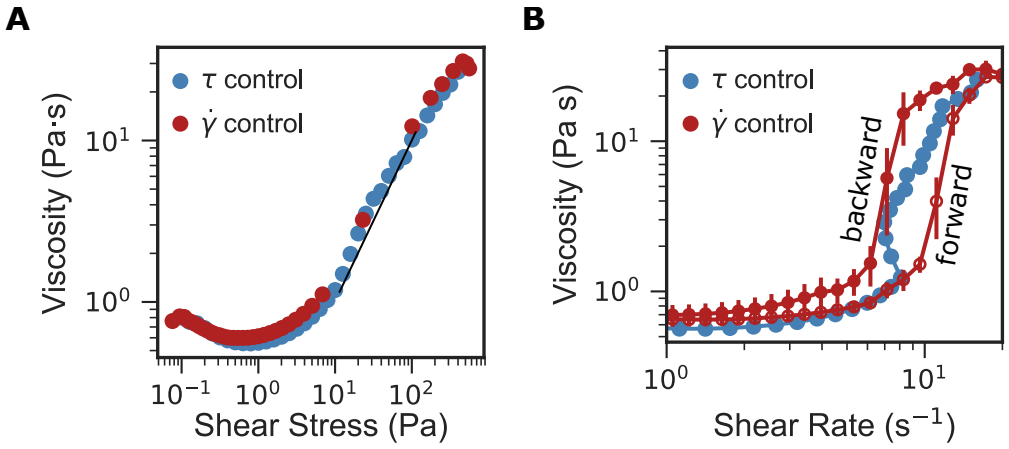

Figure 2.6: $\phi = 0.417$ cornstarch in density-matched water/glycerol as a stress-controlled experiment (blue) and as a rate-controlled experiment (red). A. Comparison of data coverage in the DST regime. The black line indicates a slope 1. B. The same data as in A plotted as a function of shear rate, with the addition of the forwards $\dot{\gamma}$-controlled ramp plotted to illustrate the hysteresis that arises over the s-shape curve under $\dot{\gamma}$-control due to $\eta(\dot{\gamma})$ not being single-valued. The s-shape can be clearly seen in the shear stress-controlled data plotted in this way, as opposed to the slight "hump in the shear-stress controlled data seen in part A. Data taken in collaboration with summer REU student Rebecca Cheng.

indicates a slope of 1, from $\tau \approx 10$ Pa to $\tau \approx 100$ Pa. This is consistent with predictions from the Wyart-Cates model [4]. As seen in previous work [5, 6, 7], $d\log(\eta)/d\log(\tau)$ is only greater than 1 for a small range in τ, after which the suspension returns to DST behavior ($d\log(\eta)/d\log(\tau) = 1$). This is likely due to slip of the jammed solid against the upper plate or other repercussions of the steady state nature of the measurement [8]. Since a curve with a region where $d\log(\eta)/d\log(\tau) > 1$ indicates an s-shaped curve with respect to shear rate (2.6B), this curve cannot be cleanly measured if shear rate is the control parameter because the viscosity is no longer single-valued with respect to rate.

This is shown clearly in 2.6B. Here, the same τ-controlled data as in 2.6A is plotted as a function of rate and shows the s-shape bend and the viscosity is not single-valued with respect to rate between $\tau \approx 7 - 9s^{-1}$. Because of this, significant hysteresis is seen in the $\dot{\gamma}$-controlled data. The forward, increasing ramp continues along the lower branch until the beginning of the s-shape, where the curve bends backwards with respect to rate. Because the rate-controlled forward ramp does not allow the shear rate to decrease, the data then

jumps directly from the lower branch upwards. On the backward (decreasing $\dot{\gamma}$) ramp, the reverse happens: the data follow the upper-branch of the s, until it meets the bend of the s-shaped region. Because the decreasing rate-controlled ramp does not allow the shear rate to increase, the data jumps down to the lower branch.

In summary, for strongly shear thickening or shear jamming suspensions, it is highly recommended to use shear stress control over the shear thickening regime for DST and SJ suspensions. This will improve data coverage in the DST regime, enable visualization of s-shaped flow curves, and avoid hysteresis.

2.2 Suspension Preparation

In this work, suspensions are generally prepared by mixing dry particles with the suspending solvent. However, because of how sensitively the flow properties depend on ϕ near ϕ_J (see Equation 1.2), care must be taken for prepared suspensions to have reproducible, well-controlled ϕ. This section details how to make reproducible suspensions for use in rheology measurements, how to minimize unwanted particle sedimentation, and how to wash and dry particles for later use in suspensions.

2.2.1 Preparing Small Quantities of Suspension with Precise ϕ

It is of paramount importance that dense suspensions are prepared with precisely controlled packing fractions. Additionally, based on particle cost and availability, it is often important to make suspensions in the smallest quantities necessary for the measurement. To achieve this, the solvent and particle quantities are measured on an analytical balance and converted to volumes through density. The density of prepared solvents is measured using a volumetric flask and a mass balance. The density is given by: $\rho = \frac{M}{V}$

Care should be taken, especially with highly viscous solvents, to ensure that bubbles are allowed to dissipate after the solution is stirred, before the density is measured. The density

of the particles can be measured by density matching.

To prepare small ($0.3 - 3$ mL) quantities of suspension, a 10 mL glass beaker is tared on an analytical balance and solvent is weighed directly into it. The equation for calculating the packing fraction for non-porous, non-absorbing particles [9] is given by

$$\phi = \frac{\frac{m_p}{\rho_p}}{\frac{m_p}{\rho_p} + \frac{m_s}{\rho_s}}, \tag{2.8}$$

where m_p is the mass of particles, ρ_p is the particle density, m_s is the solvent mass, and ρ_s is the solvent density. If the density of the particles and solvent is known, the target ϕ is specified, and the mass of solvent is measured, this equation can be used to solve for the mass of particles to add:

$$m_p = \frac{\phi \rho_p m_s}{\rho_s (1 - \phi)}. \tag{2.9}$$

Adding the particles second allows much finer control of the packing fraction, because particles can be added in ~ 0.0001 g quantities, whereas the suspending solvent mass is less well controlled based on the surface tension and drop size. This approach is more robust than trying to accurately measure small quantities of solvent using *e.g.* an Eppendorf micropipette, as these tools are not accurate over a wide range of solvent viscosities.

The particles can be slowly mixed into the solvent using a microspatula. If the suspension is highly viscous or shear jams, it can be helpful to fold the suspension over on itself repeatedly to mix. When the suspension is clearly homogeneous (which can take up to 5 minutes of stirring depending on the suspension), the sample should be covered with Parafilm and allowed to equilibrate for 45-60 minutes. This allows any surface processes or solvent absorption to equiibrate, lest the rheology data drifts over time as *e.g.* solvent is absorbed by the particles inducing a change in ϕ.

2.2.2 Preventing Particle Sedimentation

To avoid particle sedimentation, ρ_p and ρ_s should be as close as possible. For cornstarch suspensions, where $\rho_{\text{cornstarch}} \approx 1.6$ g/mL, the density of aqueous solvents can be adjusted by adding a heavy salt such as cesium chloride. The suspending solvents used in this work for cornstarch in water/glycerol are typically 50/50 water/glycerol by volume, with ~ 80 g of CsCl per 100g of water/glycerol. The exact density may vary slightly depending on the water content of the glycerol and CsCl, which are both hygroscopic and may absorb water from the air. This solution takes several hours to dissolve and may absorb water from the atmosphere over time. Thus, its density should be measured each day of experiments. Density may be easily measured by measuring 5 mL into a beaker with an Eppendorf pipette.[4]

For poly(methylmethacrylate)/itaconic acid (PMMA/ITA) particle suspensions, the particles ($\rho_{\text{PMMA}} = 1.18$ g/mL) may be density matched with glycerol ($\rho_{\text{glycerol}} = 1.2$ g/mL) concentration: 69% glycerol in water by volume has a density ≈ 1.18 g/mL, depending on the water content of the glycerol.

For silica suspensions, the particle density is so high ($\rho_{\text{silica}} \approx 2.5$ g/mL) as to make density matching the solvent unfeasible. To minimize the sedimentation due to the density mismatch, the viscosity of the solvent may be increased, for example by using 70% glycerol by volume.

2.2.3 Washing and Drying Particles for Suspension Preparation

Solution-processed particles must be dried prior to preparing suspensions using the procedure outlined in Section 2.2.1. This can be done gently by transferring the particle dispersion to a disposable Petri dish and allowing the solvent to evaporate over time, provided the particles

4 Note that Eppendorf pipettes are not designed to be used with high-viscosity fluids. Thus, it is recommended to calibrate the pipette with the suspending solvent of interest: initially measure the density using a volumetric flask. Then, weigh the mass of solvent delivered by the Eppendorf pipette using an analytical balance. Then, use the known density to determine what volume of solvent is delivered by the pippete. For 70% aqueous glyercol, the delivered volume is usually shifted by ~ 0.01 mL.

are dispersed in water or a volatile solvent. Particles dried in this way will typically be ready for use in 1-2 days, depending on the quantity of liquid present. A more concentrated dispersion with minimal liquid allows for faster drying. Particles can be more rapidly dried by heating in a vacuum oven, but care should be taken to ensure the particles do not melt, become deformed, or undergo any undesired chemical reactions at elevated heat. Starches can not be dried under heating as they have a propensity to degrade at elevated temperature.

Care should be taken to ensure that particles can be redispersed after drying in this way. Colloidal ($d < 1\mu$m) particles in particular could be at risk to irreversibly aggregate, especially if they are sterically stabilized. Redispersion can be confirmed by visualizing a dilute redispersion on an optical microscope if the particles are $d \gtrsim 1\mu$m, or by drying a dilute resuspension on a scanning electron microscope (SEM) puck and using the SEM to see if lone, evenly-dispersed particles (as apposed to large aggregate chunks) are present.

To wash particles after use in suspensions, the suspension can be diluted with a wash solvent (typically deionized water for aqueous suspensions) and the particles can be centrifuged down into a solid plug. The solvent supernatant can be decanted off. To ensure non-volatile solvent constituents such as CsCl or glycerol are removed, the particles can be redispersed in deionized water and centrifuged again. Washing particles three times in this way typically provides recycled, reusable particles. However, recycled particles should not be recombined with "pristine" particles. Slight differences in their flow behavior may be observed, possibly due to size selection[5], or aging of the surface.

2.3 Generating a State Diagram

As described in Section 1.3, the Wyart-Cates model [4] describes the shear-induced transition from frictionless, $\phi_J = \phi_0$ flow, to frictional, $\phi_J = \phi_m$ flow. This model can be used to gain information about the SJ regime from steady state rheology data. This section describes

5 if the particles are not completely centrifuged down, smaller particles may be lost in the discarded supernatant

how this was accomplished in this work. First, the model is fit to experimental data to find ϕ_0, ϕ_m, τ^*, and α. Then, the model can be solved for the state diagram boundaries using these parameters.

2.3.1 Fitting the Wyart-Cates Model

The Wyart-Cates model predicts that a suspension of packing fraction $\phi < \phi_m$ will have two Newtonian flow branches: a lower branch with viscosity dependent on $\phi_J = \phi_0$, and a higher branch with viscosity $\phi_J = \phi_m$. For packing fractions $\phi > \phi_m$, the high-shear system is solidified and thus does not have a finite viscosity: η diverges. This is shown in Figure 2.7A, in which flow curves are computationally generated using the Wyart-Cates model for values $\phi_0 = 0.64$, $\phi_m = 0.52$, $\tau^* = 100$ Pa, and $\alpha = 2$. Here it is clear that for $\phi < \phi_m = 0.52$, there are two Newtonian branches: one at $\tau \lesssim 5$ Pa, and one at $\tau \gtrsim 500$ Pa. At and above ϕ_m (*i.e.*, the blue and orange curves), the lower Newtonian plateau remains but the high viscosity diverges: the system shear jams.

If these flow curves were experimental results, we could fit them for ϕ_0, ϕ_m, and α. The upper and lower Newtonian plateaus diverge as they approach their respective ϕ_J, as shown in the inset to 2.7B, in accordance with the Krieger-Dougherty relation [10] (Equation 1.2). This data can be easily fitted for the relevant ϕ_J by scaling it such that

$$\eta_r^{-1/\alpha} = (\frac{\eta}{\eta_0})^{-1/\alpha} = \frac{-1}{\phi_J} \cdot \phi + 1. \tag{2.10}$$

This is illustrated in 2.7B, using the computer-generated data from 2.7A. Here, α can be found by linear-least-square analysis of the best linear line of fit to the data. Then, ϕ_J can be found from the slope of the line of best fit. Doing this for both the lower and upper Newtonian plateaus thus provides ϕ_0 (red) and ϕ_m (black) respectively. Now armed with these values, τ^* can be found by optimizing the Wyart-Cates model to fit the original flow curves, while varying τ^*. This can be done by substituting Equation 1.8 into Equation 1.7,

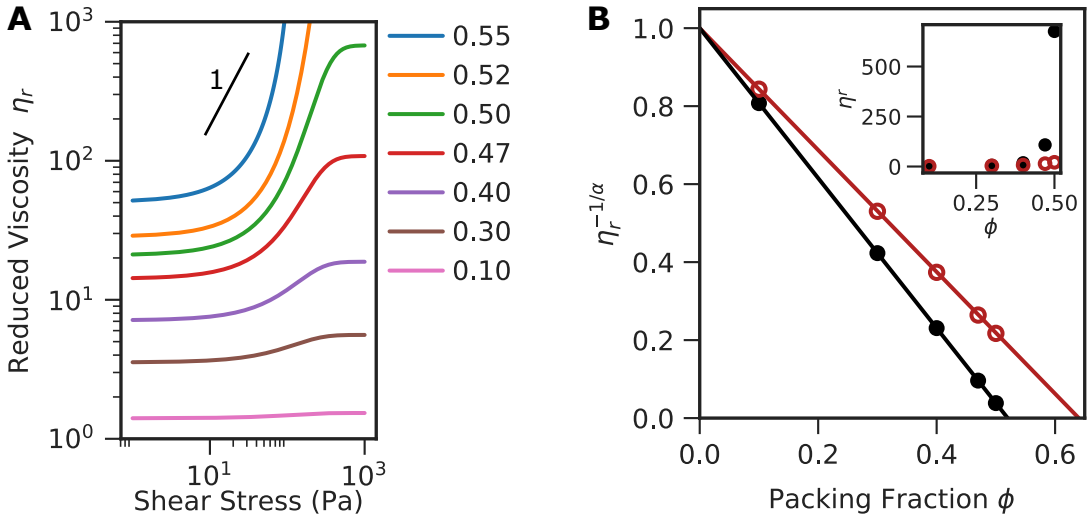

Figure 2.7: A. Flow curves computationally generated using the Wyart-Cates model with values $\phi_0 = 0.64$, $\phi_m = 0.52$, $\tau^* = 100$ Pa, and $\alpha = 2$. The legend indicates ϕ for each generated flow curve. The black line indicates a slope of 1. B. The upper (black) and lower (red) viscosity plateaus from A as a function of packing fraction, rescaled according to Equation 2.10 to enable the determination of ϕ_m and ϕ_0. Inset: unscaled upper (black) and lower (red) viscosity plateaus as a function of packing fraction, highlighting the difference in the viscosity divergence of the two Newtonian plateaus.

yielding

$$\eta = \eta_0 \cdot \left(1 - \frac{\phi}{\phi_m + e^{-\tau/\tau^*}(\phi_0 - \phi_m)}\right)^{-\alpha}, \tag{2.11}$$

where η_0 is the suspending solvent viscosity, which can be measured experimentally. Thus, by plugging in the previously-fit values of ϕ_0, ϕ_m, and α, we can use the experimental values of τ to generated calculated η. By varying τ^* and optimizing the η_{calc} against the experimentally-measured η values, τ^* can be found.

The example data shown in Figure 2.7 naturally fit perfectly for the values we used to generate the data from the model. Real experimental data, however, is often more complicated. Figure 2.8 shows experimental flow curves for wheat starch suspensions. Several deviations from the idealized Wyart-Cates flow curves are apparent. Perhaps most notably, it is unclear if there exists a true upper Newtonian plateau. Rather, most curves appear to posses a high-shear viscosity peak. This peak becomes more pointed as ϕ increases. Also, the

shear stress at the maximum viscosity is not constant: it tends to increase with increasing packing fraction.

In addition to these high-shear deviations, the low-shear viscosity may include a shear thinning regime, most apparent for the purple $\phi = 42.2\%$ curve at $\tau \lesssim 0.5$ Pa. In some suspension systems, this can completely obscure the lower Newtonian plateau. This is shown for a model system of attractive particles in Figure 2.9. In this way, shear thinning can artificially inflate the low-shear viscosity, which would result in a lower calculated ϕ_0. Thus, only flow curves where the lower Newtonian plateau can be cleanly observed should be used to fit for ϕ_0.

A signfiicant deviation from the Wyart-Cates model is that no packing fractions show the divergence seen in Figure 2.7 for the blue and orange curves at $\phi \gtrsim \phi_m$. For the wheat starch suspension shown in Figure 2.8, the purple 42.2% and dark blue 40.0% curves are at $\phi \gtrsim \phi_m$ and display strong shear jamming when manually manipulated or probed using other methods. Yet, the rheological experiments do not diverge as expected. Rather, they exhibit DST. We attribute this to complexities of the rheology measurement. The jammed suspension may slip against the upper rotating plate. The parallel plate geometry introduces a shear stress gradient, where at some radii the suspension may be jammed whereas at others it is in the DST regime. Additionally, the steady state nature of a rheological measurement is ill-suited to directly measure the transient phenomenon of shear jamming [8].

The fact that the viscosity divergence is not observed in experimental measurements can make it challenging to identify, purely from rheological data, if a suspension is shear jamming or not. However, this is very important to know if one wishes to determine ϕ_m from the data by using the Wyart Cates model. Packing fractions where $\phi > \phi_m$ must not be used, or an erroneously high ϕ_m will be determined. This creates a "chicken and egg" problem: one must know ϕ_m in order to know what data can be used to find ϕ_m. There are a few ways to develop an approximation of ϕ_m to guide what data to include in fitting.

One simple method is to manually manipulate the sample and feel for the characteristic

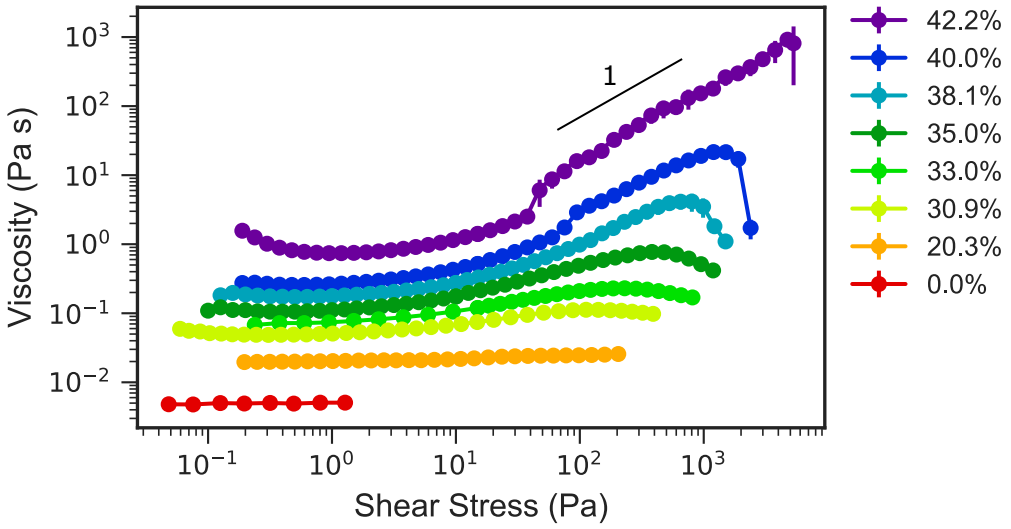

Figure 2.8: Wheat starch suspension flow curves. The legend indicates the particle packing fraction. The suspending solvent is water/glycerol, density matched with CsCl. The black line indicates a slope of 1.

resistance to upward pulling. If the packing fraction exhibits this resistance, then ϕ_m must be equal to or below this value. Quantitative measures of this type are described in Chapter 3, and can be used as well.

In practice, when one is very close to ϕ_m, it can be difficult to differentiate DST from SJ by manual manipulation. There are additional clues from the flow curves themselves. In Figure 2.8, the purple 42.2% and dark blue 40.0% flow curves exhibit a "step" region where $d\log(\eta)/d\log(\tau) > 1$ around 50-100 Pa. As discussed in Section 2.1.2, this slope is suggestive of SJ, and these packing fractions should not be used in the determination of ϕ_m.

Additionally, the low-ϕ, non-SJ suspensions have broad shallow peaks at high τ, whereas the higher packing fractions have abrupt terminations (especially for the dark blue 40.0%[6]). These are hallmarks that the suspension slipped (common with shear jamming), or was ejected from between the plates, both of which render the high-shear visocisities unusable in the determination of ϕ_m.

In this way, purely from careful observation of the rheological data we can determine that

6 The abrupt termination in the purple 42.4% data has been omitted as it obscures other curves.

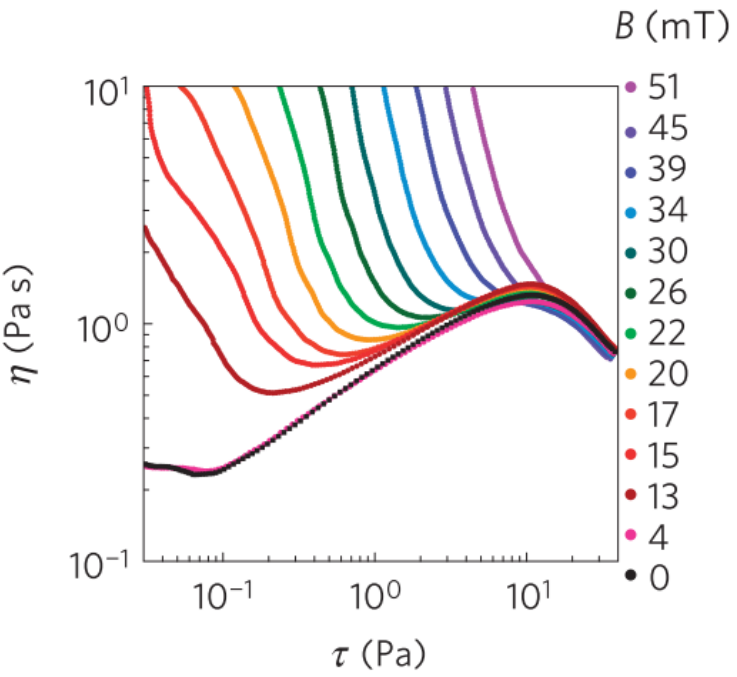

Figure 2.9: Experimental data showing that shear thinning can run into the shear thickening regime, obscuring the lower Newtonian plateau, for ferromagnetic rods as a function of magnetic field. Figure reproduced from [11]

the two highest packing fractions cannot be used in the determination of ϕ_m. However, the light blue 38.1% curve is ambiguous. It does not show a "step"-like region, but it has a more pointed high-shear viscosity peak. With packing fractions very close to shear jamming, it can be difficult to differentiate SJ and DST through manual manipulation. Thus, it is not clear from the data if the 38.1% suspension is or is not above ϕ_m. The more cautious and conservative approach would be to exclude it from fitting for ϕ_m, and take more data at $\phi < 38.1\%$ if needed.

Therefore, for the particular data shown in 2.8, it is recommended to only use the lower 5 curves to determine ϕ_m. Since the lower Newtonian plateau region can be cleanly resolved for all packing fraction, they may all be used to determine ϕ_0.

In using these curves, it is important to note that because the Wyart-Cates model does not generate low-shear thinning behavior or high-shear peaks, the optimization to determine τ^* should not include these regimes. Rather, when fitting τ^*, the data should be trimmed

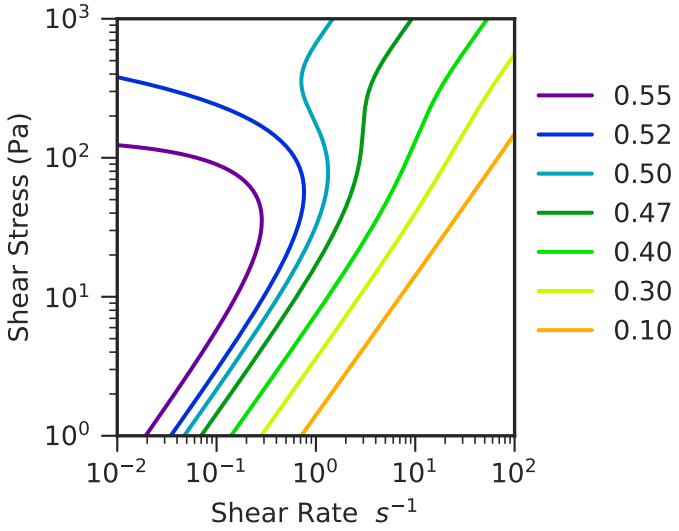

Figure 2.10: The same Wyart-Cates flow curves as generated in Figure 2.7, plotted as shear stress versus shear rate. The legend indicates ϕ for each generated flow curve.

to only include the shear stress ranges between the minimum viscosity corresponding to the lower plateau, and the maximum viscosity corresponding to the higher plateau. In principle, all η_{min} values should be on the same τ, and likewise for η_{max}.[7]

2.3.2 Solving for the State Diagram Boundaries

Armed with the fitting parameters ϕ_0, ϕ_m, α, and τ^*, it is possible to calculate the DST and SJ boundaries and generate a state diagram. To do so, consider the Wyart-Cates predictions for shear stress as a function of shear rate, shown in Figure 2.10. Here, if $\dot{\gamma} = 0$ at nonzero τ, that indicates shear jamming. Equation 2.11 can be expressed as a function of $\dot{\gamma}$ using Equation 2.3, yielding

$$\dot{\gamma} = \frac{\tau}{\eta_0}\left(1 + \frac{\phi}{\phi_m + (\phi_0 - \phi_m)e^{-\tau/\tau^*}}\right)^{-\alpha}. \tag{2.12}$$

The SJ boundary can be found by solving this equation for $\dot{\gamma} = 0$, which will generate

7 Note that this is not always true, particularly for charge stabilized particles where the τ_{min} will depend sensitively on the ionic strength of the solvent, which will in turn change with ϕ.

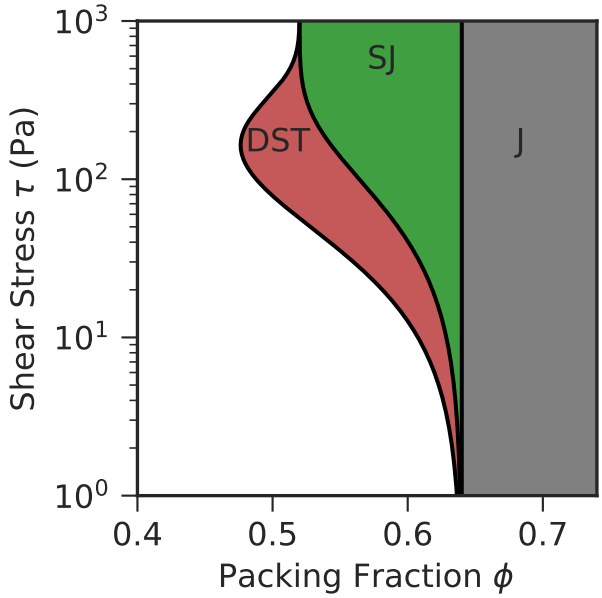

Figure 2.11: State diagram generated using $\phi_0 = 0.64$, $\phi_m = 0.52$, $\tau^* = 100$ Pa, and $\alpha = 2$, as in Figures 2.7 and 2.10.

two families of answers: one at $\tau = 0$, the trivial solution at rest. The relevant solution is for nonzero τ.

Discontinuous shear thickening occurs when there is a discontinuous increase in the viscosity or shear stress at a given shear rate, as shown in 1.4. Thus, the DST condition is that $d\log(\eta)/d\log(\dot{\gamma}) = d\log(\tau)/d\log(\dot{\gamma}) = \infty$. This can be inverted to give $d\log(\dot{\gamma})/d\log(\tau) = 0$, which can be easily solved. In this way, a state diagram can be generated such as that shown in Figure 2.11. In this model, the upper bound of SJ is not resolved. Rather, the model predicts SJ at all higher ϕ, and does not capture the "nose" shape depicted in Figure 1.6 [12]. The "nose" in the DST regime comes as a result of their being multiple solutions for this boundary over some ϕ.

BIBLIOGRAPHY

[1] Randy H Ewoldt, Michael T Johnston, and Lucas M Caretta. *Experimental Challenges of Shear Rheology: How to Avoid Bad Data*, pages 207–241. Springer New York, 2015.

[2] Leonardo E Silbert, Deniz Ertas¸ Ertas¸, Gary S Grest, Thomas C Halsey, Dov Levine, and Steven J Plimpton. Granular flow down an inclined plane: Bagnold scaling and rheology. *Physical Review E*, 64:051302, 2001.

[3] Brent J Maranzano and Norman J Wagner. The effects of particle size on reversible shear thickening of concentrated colloidal dispersions. *Journal of Chemical Physics*, 114:1693, 2001.

[4] M Wyart and M E Cates. Discontinuous Shear Thickening without Inertia in Dense Non-Brownian Suspensions. *Physical Review Letters*, 112:098302, 2014.

[5] R. Bandyopadhyay and A. K Sood. Chaotic dynamics in shear-thickening surfactant solutions. *Europhysics Letters*, 56:447–453, 2001.

[6] Zhongcheng Pan, Henri De Cagny, Bart Weber, and Daniel Bonn. S-shaped flow curves of shear thickening suspensions: Direct observation of frictional rheology. *Physical Review E*, 92:32202, 2015.

[7] Michiel Hermes, Ben M Guy, Wilson C K Poon, Guilhem Poy, Michael E Cates, and Matthieu Wyart. Unsteady flow and particle migration in dense, non-Brownian suspensions. *Journal of Rheology*, 60:905–916, 2016.

[8] Endao Han, Nicole M James, and Heinrich M Jaeger. Stress controlled rheology of dense suspensions using transient flows. *arXiv*, 2018.

[9] Endao Han, Nigel Van Ha, and Heinrich M Jaeger. Measuring the porosity and compressibility of liquid-suspended porous particles using ultrasound. *Soft Matter*, 13:3506–3513, 2017.

[10] Irvin M Krieger and Thomas J Dougherty. A Mechanism for Non-Newtonian Flow in Suspensions of Rigid Spheres. *Transactions of the Society of Rheology*, 3:137–152, 1959.

[11] Eric Brown, Nicole A Forman, Carlos S Orellana, Hanjun Zhang, Benjamin W Maynor, Douglas E Betts, Joseph M Desimone, and Heinrich M Jaeger. Generality of shear thickening in dense suspensions. *Nature Materials*, 9:220–224, 2010.

[12] Dapeng Bi, Jie Zhang, Bulbul Chakraborty, and R P Behringer. Jamming by shear. *Nature*, 480:355–358, 2011.

CHAPTER 3
HYDROGEN BONDING ELICITS SHEAR JAMMING OF DENSE SUSPENSIONS

3.1 Introduction

As discussed in Chapter 1, dense suspensions of hard particles in a liquid can exhibit strikingly counter-intuitive behavior, such as discontinuous shear thickening (DST) [1, 2, 3, 4, 5, 6, 7] and reversible shear jamming (SJ) into a state where flow is arrested and the suspension is solid-like [8, 9, 10, 11, 12]. A stress-activated crossover from hydrodynamic interactions to frictional particle contacts is key for these behaviors [2, 3, 4, 6, 7, 9, 13]. However, in experiments many suspensions show only DST, not SJ. Here we show that particle surface chemistry plays a central role in creating conditions that make SJ readily observable. We find the system's ability to form interparticle hydrogen bonds when sheared into contact elicits SJ. We demonstrate this with charge-stabilized polymer microspheres and non-spherical cornstarch particles, controlling hydrogen bond formation with solvents. The propensity for SJ is quantified by tensile tests [12] and linked to an enhanced friction by atomic force microscopy. Our results extend the fundamental understanding of the SJ mechanism and open avenues for designing strongly non-Newtonian fluids.

In suspensions, increasing the particle packing volume fraction ϕ will increase the viscosity η until, at some critical ϕ_J, the fluid jams and η diverges [1, 5, 6]. However, this is not the only route to solidification. Suspensions prepared in an unjammed state can also solidify under an applied shear stress. At fixed packing fraction $\phi < \phi_J$, increasing the applied shear

The research described in this chapter has been published in: James, N. M., Han, E., Lopez De La Cruz, R. A., Jureller, J. and Jaeger, H. M. Interparticle hydrogen bonding can elicit shear jamming in dense suspensions. *Nature Materials* 17, 965–970 (2018). E. Han performed the ultrasound experiments. R.A. Lopez De La Cruz performed the AFM experiments. J. Jureller assisted with the AFM experiments.

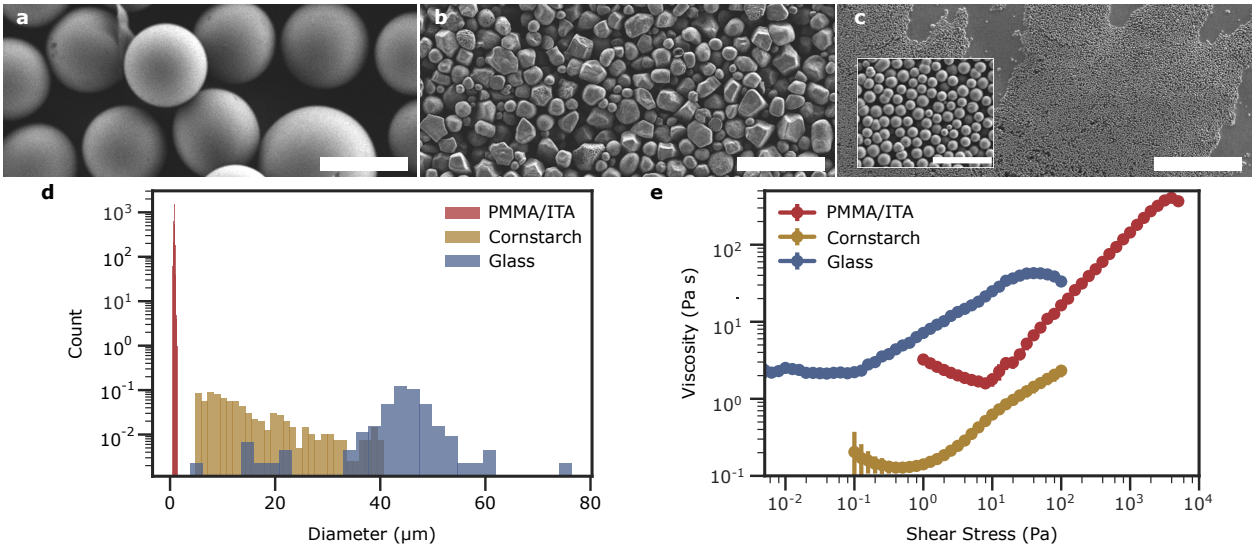

Figure 3.1: Particle characterization and flow curves. SEM images of three particle systems: (a) glass beads, (b) cornstarch, (c) PMMA/ITA. Scale bars indicate 50μm, except in the inset to (c), where the scale bar denotes 5 μm. (d) Histograms of particle size distribution obtained from image analysis. (e) Viscosity as a function of applied shear stress measured for PMMA/ITA suspended at volume fraction $\phi = 56.1\%$ in 69% aqueous glycerol, cornstarch suspended at $\phi = 43\%$ in 50% aqueous glycerol, and glass beads suspended at $\phi \approx 60\%$ in 100 cSt silicone oil. Error bars represent the standard deviation from 2-3 replicate measurements.

stress drives the suspension from a lubrication-dominated regime, through a DST regime, into a shear-jammed state with non-zero yield stress. This behavior was predicted for frictional particles [4, 14] and recently observed in experiments on dense suspensions [10, 11, 12, 15, 16]. Cornstarch in water is a prototypical suspension to exhibit such a transition from DST to SJ. However, while dense suspensions of hard, non-aggregating particles can generically exhibit pronounced DST at high packing fractions [17], shear jamming is far from ubiquitous and generally much harder to find. Which particle characteristics and dynamic driving conditions enable SJ of suspensions has so far been unresolved.

3.2 Results and Discussion

To address this, we examine three types of particles in suspension: commercially available glass and cornstarch, as well as sythesized poly(methyl-methacrylate)/itaconic acid (PMMA/ITA) microspheres [18] (see Methods). Comparing these systems allows us to test

the roles of size dispersion, shape, and material. Figure 3.1 compares the particle morphology and steady-state suspension rheology (see Methods). Prepared suspensions (see Methods) of all three systems exhibit strong, nearly discontinuous shear thickening (a slope of unity in a log-log plot of viscosity versus shear stress corresponds to a discontinuous jump in viscosity when plotted as a function of shear rate). Only the cornstarch and PMMA/ITA suspensions, however, exhibit SJ.

As a method to quickly identify SJ behavior when scanning across a wide range of suspension parameters, we take advantage of the finding that a shear-jammed state resists flow, and can fracture as a solid. In prior work, shear jamming was linked to rapidly-propagating fronts that transform a fluid suspension into a rigid state and are triggered by impact [8, 11], starting up Couette shear [10], or application of tensile stress [12]. In this case of tensile stress, the suspension surface is pulled upwards and the fronts propagate downward into the bulk of the suspension (see Methods). Stress is supplied by pulling on the suspension, and balanced by viscous stress at the position of the moving front, where the shear is localized [12]. To enter the SJ regime, both a minimum stress level (or, equivalently, a minimum shear rate) and a sufficiently high packing fraction are required. Although observing the propagating jamming fronts gives a wealth of information about SJ behavior, the setup in Figure 3.2a provides a simple alternative for verifying the occurrence of SJ, as the solidified suspension resists the upward motion, applying a normal force on the rod. This is similar to extensional rheology studies [19, 20], but rather than extracting the viscosity, here we use the normal force magnitude to identify solidification.

Suspensions that enter the SJ regime produce strikingly different forces during extension than non-SJ suspensions (Figure 3.2b). To characterize these differences, we plot in Figure 3.2c the pulling force, defined as the absolute value of the peak force in Figure 3.2b, as a function of packing fraction. Even at $\phi = 57\%$, the glass bead suspensions exhibit pulling forces no larger than those of oils near the same effective viscosity ($6{\cdot}10^4$ cSt silicone oil). On the other hand, both cornstarch and PMMA/ITA reach pulling forces of 8 N or more,

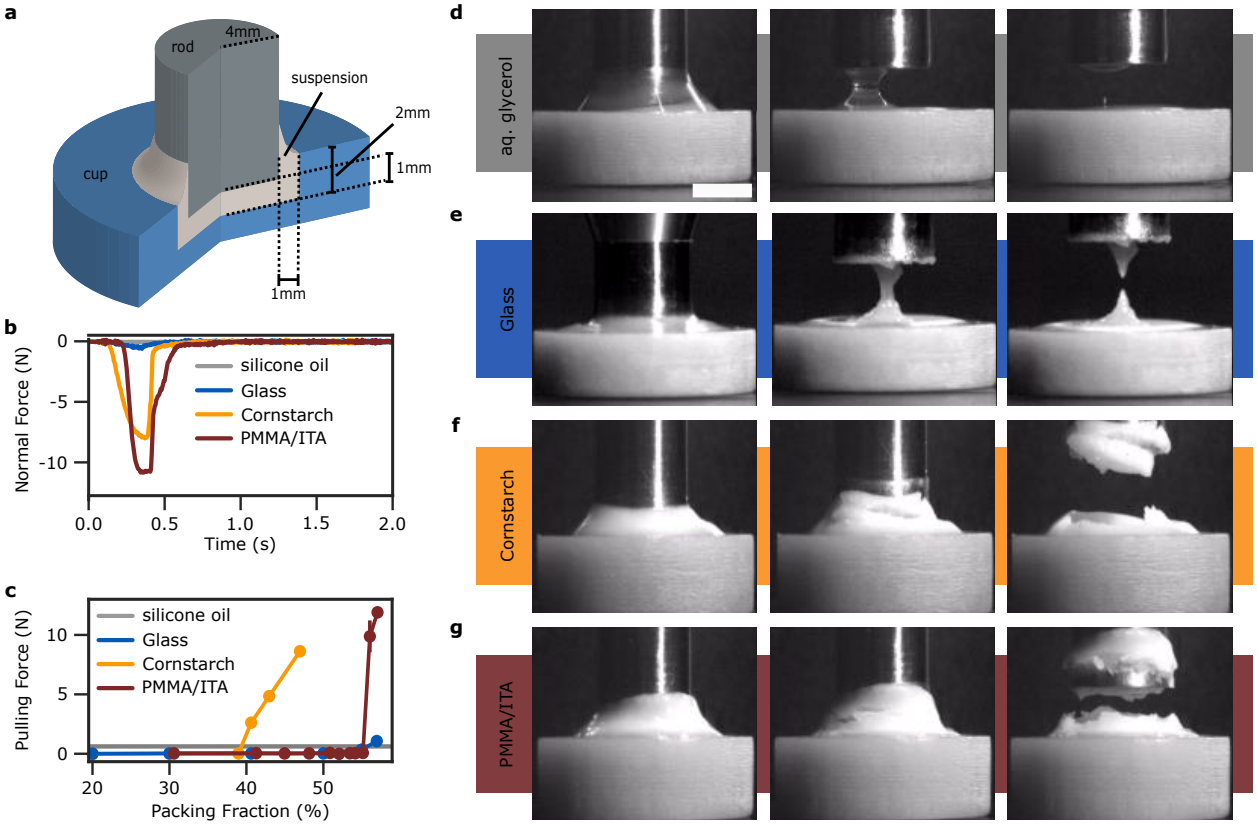

Figure 3.2: Tensile test for shear jamming. (a) Schematic of the tensile test cell, shown in cross-section. (b) Representative raw data for the suspensions shown in Figure 3.1e, showing the normal force measured by the rheometer as the rod, initially at rest, is pulled upward at a rate of 8 mm/s. (c) Magnitude of peak force from data in (b), as a function of volume fraction. High-viscosity ($6 \cdot 10^4$ cSt) silicone oil is shown for comparison. Error bars represent the standard deviation from 5 replicate measurements. (d-g) Images of the extensional behavior of glycerol, glass, cornstarch, and PMMA/ITA, corresponding to the data in (b) The scale bar in row (d) indicates 5 mm. In each row, the suspension is depicted prior to the start of the measurement, near the point of peak force and incipient failure, and after detachment of the fluid column.

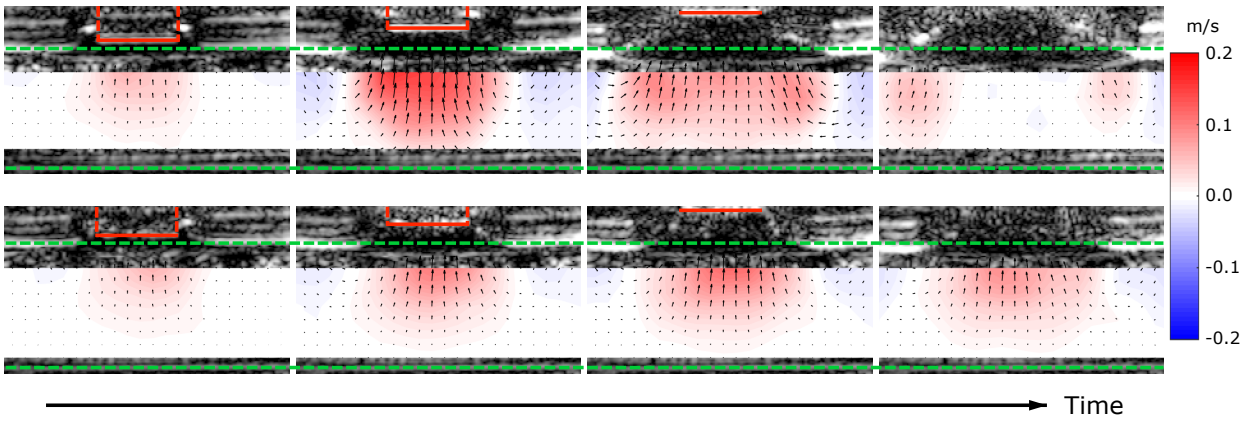

Figure 3.3: High-speed ultrasound imaging of PMMA/ITA suspension dynamics. Top row: $\phi > 56\%$ PMMA/ITA suspension. Bottom row: $\phi < 56\%$ PMMA/ITA suspension. Each row's sequence shows still frames of the suspension flow field under tensile stress. Velocity maps from particle image velocimetry are overlaid. The color field indicates vertical velocity, with red indicating upward motion, and blue indicating downward motion. In the top row, the jamming front corresponds to the perimeter of the jammed (red) region. The initial top and bottom boundaries of the suspension (before extension) are indicated by dashed green lines. Under extension, the bottom boundary remains stationary while the top boundary deforms upward with the rod. The rod pulling the suspension upward is indicated by the red line. The images are snapshots in time, showing the jamming front reaching and interacting with the bottom boundary until a non-moving, solid-like state is achieved, indicated by the large white, zero-velocity region. In the bottom row, only viscous flow is observed.

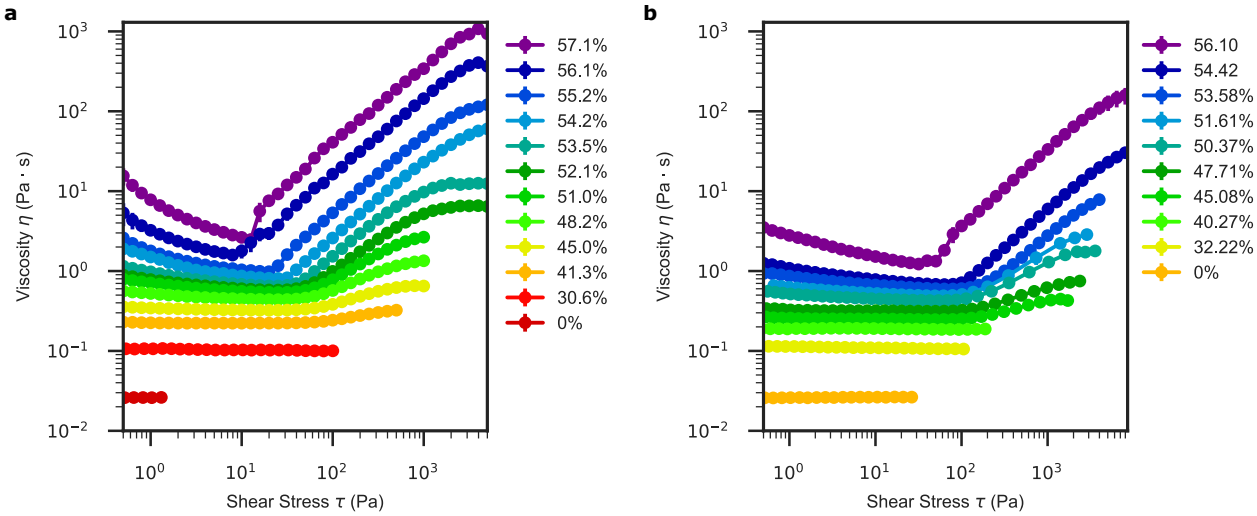

Figure 3.4: Steady-state rheology for PMMA/ITA suspensions with urea as a function of packing fraction. (a) PMMA/ITA in water/glycerol with 0 M urea. (b) PMMA/ITA in water/glycerol with 6 M urea. These data were used to calculate the state diagram (Figure 3.5), as described in the Methods. Error bars indicate the standard deviation of 3 replicate measurements.

corresponding to stresses in excess of 100 kPa. These stress levels are significantly larger than achievable under steady-state flow (Figure 3.1d) and are a quantitative indication of the solidification associated with SJ. For the data in Figure 3.2 the pulling speed of the rod was 8 mm/s and the onset of SJ is seen to occur at $\phi \approx 40\%$ and $\phi \approx 56\%$ for cornstarch and PMMA/ITA, respectively. As was done previously for cornstarch [12], we verified with high-speed ultrasound imaging that PMMA/ITA exhibits jamming fronts when ϕ is large enough to cross into the SJ regime, while less concentrated suspensions only produce viscous flow. These results are shown in Figure 3.3. Qualitatively, this can already be observed through visual inspection of the suspension column during extension (Figure 3.2d-g): non-SJ suspensions (Figure 3.2d-e) experience a neck and pinch-off detachment, whereas SJ suspensions (Figure 3.2f-g) show cleavage planes suggesting brittle fracture [20].

The results in Figure 3.1 and 3.2 rule out particle shape and size as primary drivers for SJ, since smooth, size-controlled PMMA/ITA microspheres around 0.8 μm in diameter exhibit SJ just as well and even more strongly than rough, irregular cornstarch particles with a median diameter near 11 μm. This apparent independence from particle geometry drives us to

examine more closely the roles of particle surface chemistry and solvent [21]. Starch particles have surface hydroxyl groups, while PMMA/ITA particles have surface carboxyl groups. In aqueous suspensions, this allows both starch and PMMA/ITA to form interparticle hydrogen bonds. Here we show that this chemical contribution to the nature of particle contacts can elicit SJ.

We investigate the effect of introducing a chaotropic agent, *i.e.* a compound such as urea that specifically interferes with hydrogen bonding, to the suspending solvent. Figure 3.4 shows steady state rheology data for PMMA/ITA suspensions at 0 M and 6 M urea. From these data it is clear that DST, while shifted to higher stresses and with a lower maximum viscosity, remains intact. These changes, however, signal significant changes in suspension shear jamming.

Figure 3.5a shows the pulling force as a function of urea concentration for $\phi = 56\%$ PMMA/ITA suspensions under a pulling speed of 8 mm/s. At this speed, shear jamming is eliminated above ~ 2 M urea. This threshold concentration corresponds to on the order of 10^{22} urea molecules per 100 mL of $\phi = 56\%$ suspension, commensurate with the number of hydrogen bonding sites in the system: the particle surface density of COOH groups is around 10nm^{-2} [18], which implies $\sim 10^{22}$ surface COOH groups for the 0.8 μm diameter particles in 100 mL of $\phi = 56\%$ suspension. Meanwhile, DST remains essentially unaffected by the presence of urea (Figure 3.5b), implying a shift of the DST-SJ boundary.

To understand this behavior we consider the state diagram for dense suspensions of frictional particles, which delineates different regimes as a function of packing fraction ϕ and applied shear stress τ. The diagram in Figure 3.5c was calculated using the model by Wyart and Cates [4], with parameter values extracted from steady-state measurements of the viscosity as a function of shear rate for different ϕ and urea concentrations (see Methods and Figures 3.2-3.5). For clarity, we do not plot the DST region for 6 M urea. The complete state diagram can be seen in Figure 3.6. A similar state diagram was obtained very recently in simulations by Morris and coworkers [22]. Besides ϕ_{J}, the packing fraction beyond which

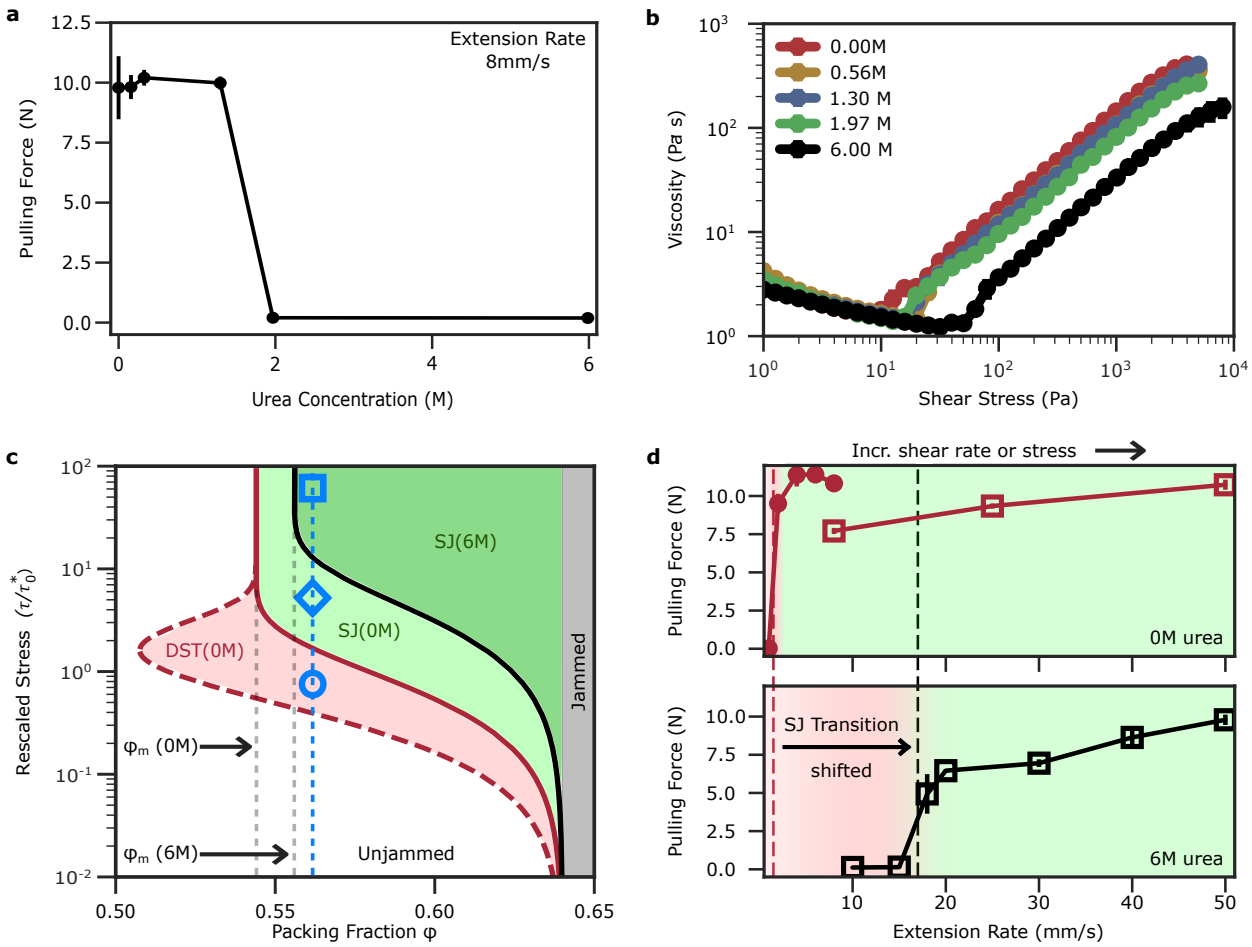

Figure 3.5: (a) Peak pulling force for $\phi = 56.0\%$ PMMA/ITA particles in 69% aqueous glycerol as a function of urea concentration. Error bars represent the standard deviation from 5 replicate measurements. (b) Steady-state rheometry data for the suspensions tested in (a), demonstrating that DST is shifted, but otherwise unaffected by the addition of urea. Error bars represent the standard deviation from 3 replicate measurements. (c) State diagram for dense suspensions of hard particles, showing the regions of DST (red), SJ (green), and frictionless, isotropic jamming (grey). The shear stress is normalized with the threshold stress τ_0^* at 0 M urea concentration. As urea concentration changed from 0 M to 6 M, ϕ_J is unchanged, but τ^* and ϕ_m both increase. As a result, the SJ region shrinks. The blue circle, square, and diamond qualitatively represent extension tests at $\phi = 56.0\%$ using different pulling speeds, thus probing distinct regimes of suspension response to applied shear stress. (d) Tensile tests conducted as a function of pulling speed for 56% PMMA/ITA in 69% aq. glycerol with 0 M urea (top) and 6 M urea (bottom). The step-like increase in pulling force indicates the location of the DST-SJ boundary at a given ϕ. Filled symbols represent from tensile tests performed with the rheometer, open symbols from tests using a linear actuator. While the latter can generate faster pulling speeds, it is less accurate and gives somewhat smaller peak force values. However, this does not affect the ability to track the shift in the onset of SJ to higher rates and thus higher shear stress values. Error bars represent the standard deviation of 5 replicate measurement.

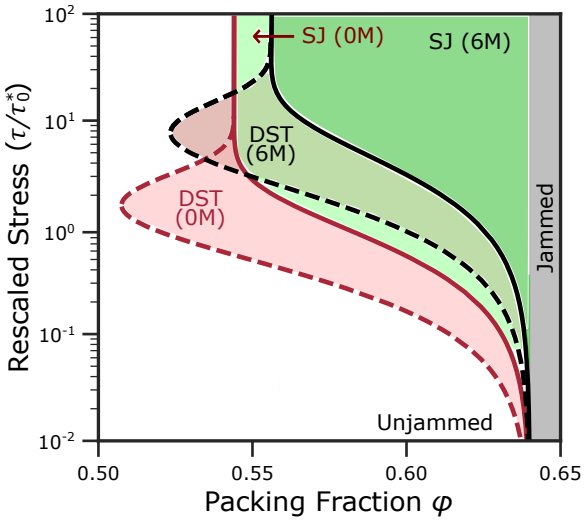

Figure 3.6: Complete state diagram with 0 M and 6 M urea. As in Figure 3.5, this state diagram contrasts the DST and SJ behavior of PMMA/ITA suspensions in water/glycerol mixtures with either 0 M or 6 M urea. In Figure 3.5, this regime is omitted for clarity. Here it is shown to illustrate that both the DST regime and the SJ regime are affected by sufficiently large urea concentration, which is consistent with the understanding that interparticle friction plays a role in both DST and SJ.

even fully lubricated (*i.e.*, frictionless) hard particles will jam, a key parameter setting the DST-SJ boundary is ϕ_{m}, the packing fraction at which the viscosity of frictional particles in suspension diverges. As the urea concentration is increased, we find that ϕ_{m} increases and the DST-SJ boundary is shifted up and to the right (Figure 3.5b). Thus, a $\phi = 56\%$ suspension that, without urea, exhibits SJ at the shear stress level exerted by the pull test, (*i.e.*, is inside the light green region in Figure 3.5c, indicated for example by the blue diamond) can find itself outside the SJ region once urea is introduced (dark green region). Since the DST-SJ boundary is very steep near ϕ_m, this makes the pull test a facile method for identifying the emergence, or demise, of SJ as suspension parameters are varied.

In the state diagram, the DST-SJ boundary can be crossed by varying the applied shear stress. Three illustrative points are labeled in Figure 3.5b by the blue circle, diamond, and square. They identify stress levels where, respectively, only DST is observed, SJ vanishes above 2M urea, and SJ survives at 6M urea, all without changing ϕ. In our tensile test this is verified by varying the pulling speed (Figure 3.5d). Tracking where the pulling force increases sharply provides a convenient means of locating the DST-SJ boundary and of quantifying its shift when urea has been added.

A central aspect of shear jamming is that the packing fraction ϕ_{m} depends on the interparticle friction [4, 9, 22]: a smaller coefficient of friction leads to a larger ϕ_{m} and thus to a smaller range, between ϕ_{m} and ϕ_{J}, over which the SJ regime can be achieved. As a result, the observed increase in ϕ_{m} with increasing urea concentration links the weakening of hydrogen bonding to a decrease in effective friction.

In cornstarch we can similarly manipulate the solvent to suppress SJ while leaving DST intact. Figure 3.7a shows the pulling response of $\phi = 43\%$ cornstarch in water/dimethylformamide (DMF) mixtures. Water is a polar protic solvent, capable of donating hydrogen bonds. DMF has a viscosity and density very similar to water (0.92 mPa·s and 0.944 g/mL at 20 °C) but is a polar aprotic solvent, which has no polar hydrogens and thus is not a hydrogen bond donor. By tuning the concentration of water in water/DMF mixtures, we tune the capacity

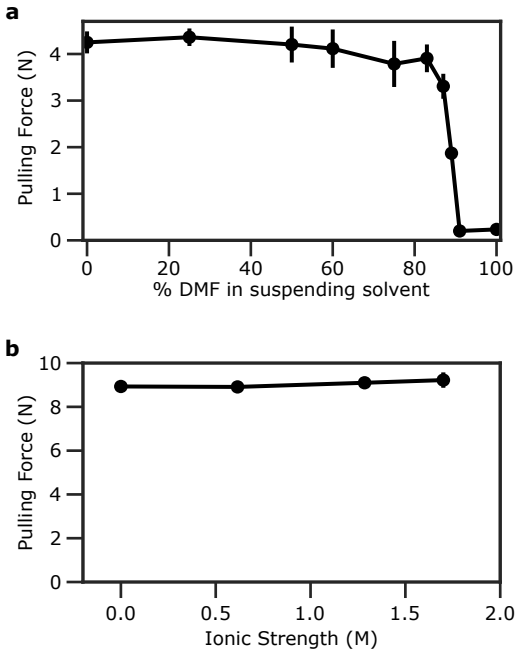

Figure 3.7: The effect of aprotic solvents and ionic strength on shear jamming. (a) Peak pulling force as a function of DMF concentration for $\phi = 43\%$ cornstarch in 50% aqueous glycerol. DMF is a polar aprotic solvent that can displace water and thereby reduce the likelihood of hydrogen bond formation. Steady-state flow curves for these suspensions, demonstrating that DST persists even though SJ has been suppressed, can be found in Figure 3.8. (b) Peak pulling force as a function of ionic strength by adjusting the NaCl concentration. The data are for $\phi = 43\%$ cornstarch in 50% aqueous glycerol, as in (a). The steady-state flow curves for these suspensions can be found in Figure 3.10. Error bars represent the standard deviation from 3-5 replicate measurements.

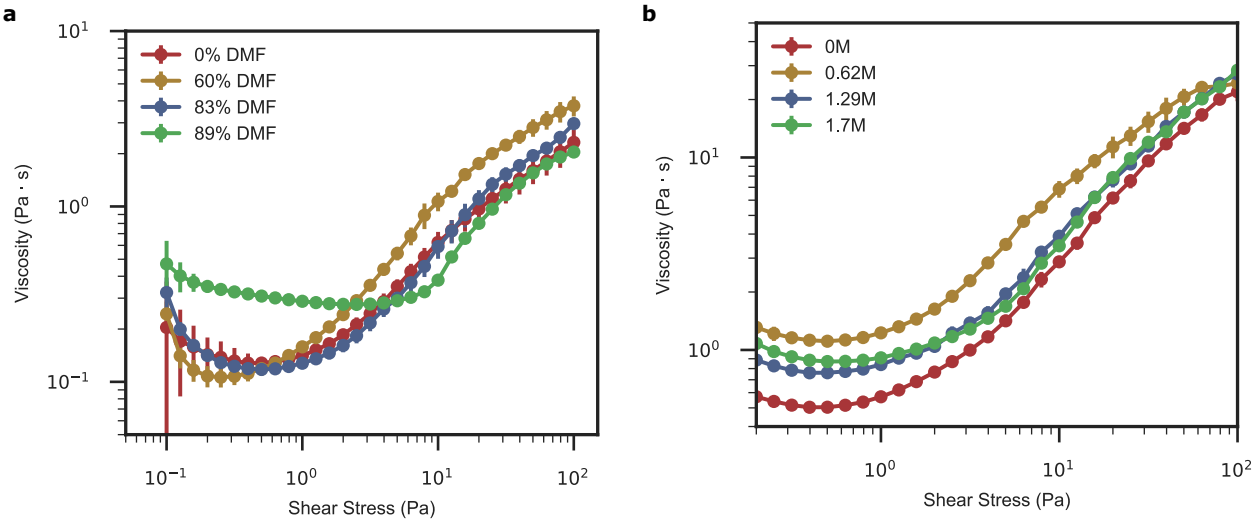

Figure 3.8: Steady state rheology of cornstarch as a function of solvent composition. (a) 43% Cornstarch in DMF/water mixtures. (b) 43% cornstarch in 50/50 water/glycerol, with ionic strength controlled by added NaCl. The minimum viscosity in these curves does not significantly decrease. This means the tensile test experiments, which are conducted as a function of pulling speed, are all performed at approximately constant applied shear stress and may be directly compared. Thus, the plots in Figure 3.7 are accurate representations of how the SJ boundary does or does not move over the point in the state diagram that corresponds to $\phi = 0.43\%$ and a pulling speed of 8 mm/s. Error bars indicate the standard deviation in 2-3 replicate trials.

of the suspending solvent to facilitate interparticle hydrogen bonds, particularly through donating hydrogens, as the particles come into contact under applied shear or separate after shear is released. As the DMF concentration is increased, no change in the pulling force is seen up until $\sim 80\%$ DMF, after which the pulling force abruptly drops below the detection threshold. Figure 3.8 shows the steady state rheology of the suspensions used in these tensile tests. These results show that the normal force decrease, indicating a reduction in the SJ response, could not be an artifact of decreasing suspension viscosity as the solvents are changed.

We interpret these results to indicate that as long as sufficient water is available to mediate interparticle hydrogen bonding, shear jamming remains unaffected. If the polar protic solvent activity drops too low, hydrogen bonding interactions between particles are insufficient, fewer interparticle hydrogen bonds may form, and shear jamming is suppressed.

Adding a salt to cornstarch suspensions does not change the SJ behavior (Figure 3.7b), even at ionic strengths around 1 M, where the screening length is reduced to less than 1 nm. The robust independence to ionic strength suggests that hydrogen bonding relevant for SJ behavior occurs at locations where particles come into effectively direct contact, as opposed to inducing a longer-range structuring of the surrounding solvent, *e.g.* via the creation of solvation shells. The latter has been associated with increased shear thickening in aqueous suspensions of fine silica particles [23, 24], but not shear jamming.

From these results a picture emerges in which shear jamming is activated when particles are forced sufficiently close that interparticle hydrogen bonds can create the equivalent of strong frictional interactions. To explore more directly the repercussions of hydrogen bonding on the friction between individual particles, we used colloidal-probe atomic force microscopy (AFM), using cantilevers equipped with $\sim 1\mu$m spheres functionalized with either carboxyl (COOH) or alkyl (RCH_3) surface groups (see Methods). This strategy allowed us to vary the chemistry of only one of the contacting surfaces, isolating its effect. Our AFM data are based on scans near the apex of the particles, 100nm in distance and sufficiently slow to avoid viscous drag contributions from hydrodynamic interaction with the solvent. This differs from recent work by Comtet *et al.* [25], who used a fast oscillatory method to probe friction much more locally. Figure 3.9a shows the topographical image and line-scan profile of PMMA/ITA particles glued to a substrate with epoxy. Through lateral force measurements (Figure 3.9b), we find that when the cantilever is COOH-terminated to enable hydrogen bonding, the result is a nearly two-fold enhancement of the average friction coefficient, μ, from 0.30 (CH termination) to 0.53 (OH termination). Recent simulations [22] also predict that such change in μ will generate changes on the order of a few percent in ϕ_{m}, consistent with how we observed SJ to be suppressed by urea.

The notion of hydrogen bonds providing strong frictional interactions introduces a perspective that connects macro-scale suspension behavior to molecular-scale particle surface properties. We envision the hydrogen bonds as direct, interparticle bonds or as short net-

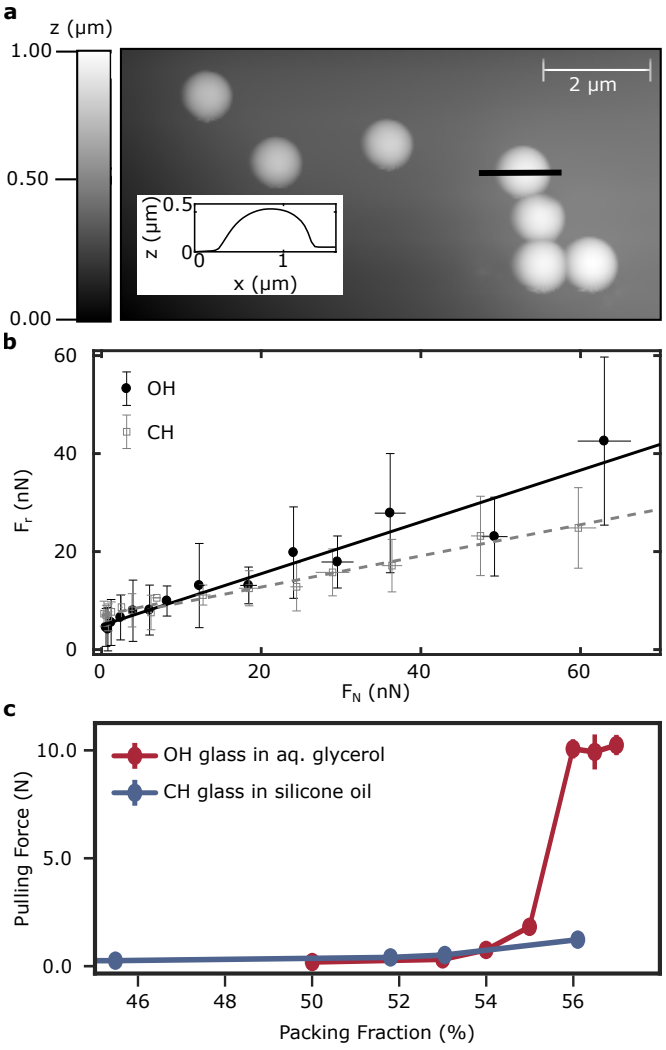

Figure 3.9: Connecting particle surface chemistry and interparticle friction. (a) AFM topography image of PMMA/ITA particles. The black bar indicates the location of the line scan plotted in the inset, which shows that particles protrude approximately 0.5 μm above the thin epoxy layer that embeds them. (b) Lateral force as a function of applied normal force, measured near the apex of PMMA/ITA particles. Data for COOH- and CH_3-functionalized colloidal cantilevers are shown, with error bars representing the standard deviation of 7-20 replicate measurements. Lines are linear fits. The friction coefficient is given by the slope of these lines (OH: 0.53 , CH: 0.3). (c) Pulling force as a function of packing fraction for 3-6 μm glass beads with different surface treatments. While hydrophobic, silanized soda-lime glass beads in 100 cSt silicone oil (blue) show no stronger force than a highly viscous fluid, shear jamming is observed in hydrophilic, silanol-terminated glass beads in aqueous glycerol (red). Error bars represent the standard deviation from 5 replicate measurements. Steady state rheological measurements for these suspensions are in Figure 3.10.

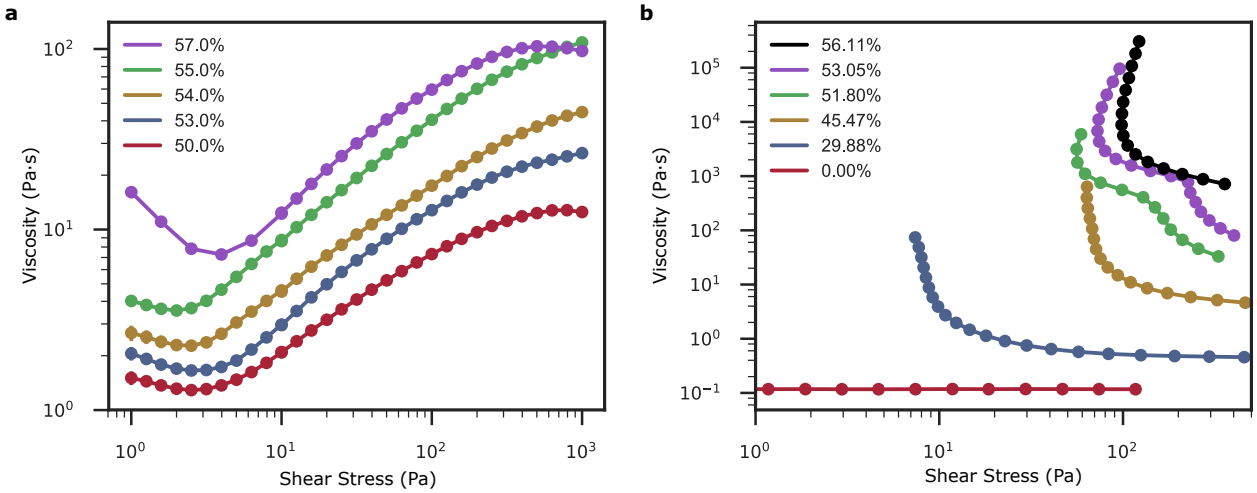

Figure 3.10: Steady-state rheology for 3-6μm diameter glass beads. (a) hydrophilic glass beads suspended in water/glycerol. (b) hydrophobic glass beads suspended in 100 cSt silicone oil. Error bars indicate the standard deviation in 1-3 replicate trials.

works spanning a nano-sized gap between surfaces. In polar protic solvents like water hydrogen bonds are reversible under thermal fluctuations, but the costs associated with bond stretching and bending provide a resistance to slipping. This resistance to tangential motion manifests as an increase in interparticle friction. Our findings in Figures 3.5-3.9 are in line with recent models where SJ emerges only once a sufficiently large fraction of particles have crossed over from interacting via frictionless hydrodynamic lubrication (where ϕ_0 is key) to undergoing enduring frictional contacts (where ϕ_m is key) so that the suspension solidifies and flow ceases [4, 9, 22]. By contrast, DST in dense suspensions can be observed as long as there is enough friction that steady-state shear will generate enhanced stress due to "frustrated dilation" [5, 17] or, equivalently, intermittent, partial jamming events [2, 3, 6].

We can take these results one step further and use them to rationally design systems that highlight or eliminate SJ behavior. For example, hydrophilic soda lime glass has surface silanol (Si-OH) groups, and thus can form interparticle hydrogen bonds. Therefore, suspensions of these particles in water/glycerol mixtures can be expected to shear jam. However, hydrophobic, silane-functionalized glass spheres of the same size are incapable of interparticle hydrogen bonding. When dispersed in an appropriate solvent (*e.g.* silicone oil),

the suspensions may display non-Newtonian behavior, but not SJ. We confirm this in Figure 3.9c with commercially-available, 3-6μm diameter glass spheres (Cospheric). Figure 3.10 shows the steady state rheology of the suspensions used in these tensile tests. These results show that the normal force response, indicating a reduction an SJ response for hydrophilic silica suspensions and no SJ response for hydrophobic silica suspensions, could not be an artifact of a reduction in suspension viscosity of the hydrophobic suspensions. Thus, by carefully considering the particle surface chemistry and solvent, we can tailor the capacity to shear jam.

3.3 Conclusions

Our work explains why suspensions of starch particles exhibit DST as well as SJ over an appreciable range of packing fractions below ϕ_J and under reasonable applied stress levels (or impact/pulling speeds), while (most) other particle systems under such conditions only show DST unless their surfaces are suitably conditioned. It also explains why we can suppress SJ by selectively preventing hydrogen bonding. A key aspect emerging from the data is that, while both DST and SJ rely on friction, the stress-activated solidification associated with SJ requires an enhanced particle-particle contact interaction. Geometric variables such as particle shape and size appear not to pose fundamental requirements for SJ, although they may affect details.

The ability to control SJ through particle surface chemistry provides a powerful tool for the design of suspension-based materials that can transform reversibly from fluid to solid-like behavior in response to applied stresses. At the same time, it points to opportunities for addressing issues that are just beginning to be explored, such as how the various time scales that characterize a jammed solid's relaxation [5, 26, 27] might depend on the surface-chemistry-mediated particle interactions.

3.4 Methods

3.4.1 Particle Synthesis

We synthesized micron-scale poly(methylmethacrylate)/itaconic acid (PMMA/ITA) particles according to the procedure reported by Appel *et al.* [18]. Briefly: methyl methacrylate (MMA), water, and itaconic acid are combined in a round-bottom flask. The flask is sealed with a septum and purged with nitrogen. After heating to 85 °C while stirring, 4,4'-Azobis(4-cyanovaleric acid) is injected to initiate the reaction. The reaction is allowed to proceed for 12 hours, after which the particles can be separated by centrifugation and dried. The precise particle size is controlled by the MMA/water ratio (55 g/125 g for 1 μm diameter particles). Particles were imaged with a Zeiss Merlin scanning electron microscope (SEM). Particle surface charge was obtained by dynamic light scattering (DLS) using a Malvern ZetaSizer Nano ZS. Particle sizes were obtained by DLS and SEM image analysis. To ensure all particle characteristics such as size distribution are the same for every experiment, multiple syntheses were conducted and all particles combined together. All PMMA/ITA experiments shown here were done using particles from this combined batch.

3.4.2 Suspension Preparation

PMMA and glass suspensions are reported as volume fractions: suspending solvent and dry particles were measured out by mass, and converted to volume through density (1.18 g/mL for PMMA/ITA and 2.5 g/mL for glass). To obtain precise packing fractions, suspending solvent was weighed first, and particles were added directly to solvent while recording mass. Suspensions were allowed to equilibrate for at least 45 minutes before use, and were used same-day to avoid solvent evaporation.

Cornstarch particles have a porosity around 30% and thus absorb solvent, which significantly raises the actual volume fraction of solids. Han *et al.* carefully characterized the solvent-dependent absorption to obtain corrected volume fractions [28]. Due to the variety

of solvents used in the experiments reported here, we do not perform these corrections and for cornstarch simply report the uncorrected solids fraction based on the dry material volume dispersed.

3.4.3 Tensile Test Protocol

For all tensile tests conducted at a pulling speed of $\leq$ 8 mm/s, we used an Anton Paar MCR301 rheometer to pull the suspension surface by withdrawing an 8 mm rod that was partially embedded to a depth of 1 mm in the sample. Simultaneously, we measured the normal force response on the rod. In these experiments, the rheometer only applied a normal extension; there was no rotation of the rod. A schematic of the apparatus with dimensions is shown in Figure 3.2a. To ensure the sample volume and contact with the rod was consistent between experiments, a 3-D printed cup was used to contain the sample. The cup was affixed to the bottom plate of the rheometer with double-sided tape, and the suspension was leveled to the top of the cup prior to lowering the rod.

For pulling speeds $>$ 8 mm/s, we used a computer controlled linear actuator (SCN5, Dyadic Systems). The experiments were performed with the same sample cup and the same procedure as those conducted with the rheometer. The rod head had the same diameter of 8 mm. The force applied on the rod was measured by a force sensor (DLC101, Omega) placed between the rod and the actuator. In contrast to the rheometer, this particular type of electromagnetic actuator produced a linear trajectory with added small oscillations along its axis, mainly as a result of the feedback mechanism controlling its motion. This accounts for the softening of the SJ state, seen in the slight mismatch between the rheometer and actuator data. However, the shift in the onset of shear jamming is clearly apparent.

With the exception of Figure 3.5d, all tensile test experiments were conducted at 8 mm/s using the Anton Par MCR301 rheometer.

3.4.4 Steady State Rheology

Steady-state rheological experiments were conducted using a stress-controlled Anton Paar MCR301 rheometer with parallel plate (25 mm diameter) geometry. Sample temperatures were maintained to within 1 °C for each run. All experiments were conducted within 22-25 °C. A solvent trap was used to mitigate sample evaporation.

3.4.5 State Diagram Preparation

From the steady state rheology experiments with PMMA suspensions, we obtained the stress-shear rate curves at different packing fractions ϕ, as shown in Figure 3.4. At each ϕ, we found the viscosity of the suspension in the Newtonian regime η_1 and the peak viscosity η_2 if the stress at the peak was below the limit set by the surface tension. By fitting the viscosities as functions of packing fraction $\eta_1(\phi)$ and $\eta_2(\phi)$ with $\eta_1 = \eta_0(1-\phi/\phi_0)^\alpha$ (we set $\phi_0 = 0.64$), and $\eta_2 = \eta_0(1-\phi/\phi_\mathrm{m})^\beta$, we obtained the frictional jamming packing fraction ϕ_m, the solvent viscosity η_0, and the powers $\alpha \approx \beta = -1.8$.

With ϕ_0, ϕ_m, η_0, and the powers determined, the last remaining parameter is the threshold stress τ^*. This was accomplished by calculating the η-$\dot{\gamma}$ relations ($\tau = \eta_0\dot{\gamma}(1-\frac{\phi}{\phi_\mathrm{eff}(\tau^*)})^\alpha$) at all experimentally-measured packing fractions, at various τ^*. At each τ^*, we calculated the difference between the experimental data and the prediction of the model, obtained the sum of squared differences, and took the τ^* at the minimum as the best fit. We performed this fitting procedure for data at 0 M and 6 M urea concentrations.

3.4.6 AFM Procedure

An Asylum Research MFP-3D-BIO atomic force microscope operating in lateral force mode was used to acquire frictional force images. Surface-modified colloidal cantilevers (Novascan Technologies, Ames, AI, USA; k = 0.6 N/m and k = 0.09 N/m; tip radius = 1 μm; surface modification: COOH and CH_3 groups) were calibrated for spring constant and sensitivity,

both in normal and lateral directions. Particles were immobilized in a thin layer of epoxy (Parbond 5105, Parson Adhesives) on top of a glass coverslide, and left to dry overnight. Images were acquired in deionized water at a 1 Hz line scan rate at different loads. The particles were first imaged in tapping mode with a silicon cantilever (ACTA, App Nano; k = 37 N/m) to verify that they were not completely submerged in the epoxy.

BIBLIOGRAPHY

[1] H A Barnes. Shear-Thickening ("Dilatancy") in Suspensions ofNonaggregating Solid Particles Dispersed in Newtonian Liquids. *The Journal of Rheology*, 33:329–367, 1989.

[2] Ryohei Seto, Romain Mari, Jeffrey F Morris, and Morton M Denn. Discontinuous Shear Thickening of Frictional Hard-Sphere Suspensions. *Physical Review Letters*, 111:218301, 2013.

[3] Nicolas Fernandez, Roman Mani, David Rinaldi, Dirk Kadau, Martin Mosquet, Hélè Ne Lombois-Burger, Juliette Cayer-Barrioz, Hans J Herrmann, Nicholas D Spencer, and Lucio Isa. Microscopic Mechanism for Shear Thickening of Non-Brownian Suspensions. *Physical Review Letters*, 111:108301, 2013.

[4] M Wyart and M E Cates. Discontinuous Shear Thickening without Inertia in Dense Non-Brownian Suspensions. *Physical Review Letters*, 112:098302, 2014.

[5] Eric Brown and Heinrich M Jaeger. Shear thickening in concentrated suspensions: phenomenology, mechanisms and relations to jamming. *Reports on Progress in Physics*, 77:046602, 2014.

[6] Romain Mari, Ryohei Seto, Jeffrey F Morris, and Morton M Denn. Nonmonotonic flow curves of shear thickening suspensions. *Physical Review E*, 91:52302, 2015.

[7] John R Royer, Daniel L Blair, and Steven D Hudson. Rheological Signature of Frictional Interactions in Shear Thickening Suspensions. *Physical Review Letters*, 116:188301, 2016.

[8] Scott R Waitukaitis and Heinrich M Jaeger. Impact-activated solidification of dense suspensions via dynamic jamming fronts. *Nature*, 487:205–209, 2012.

[9] Christopher Ness and Jin Sun. Shear thickening regimes of dense non-Brownian suspensions. *Soft Matter*, 12:914, 2016.

[10] Ivo R Peters, Sayantan Majumdar, and Heinrich M Jaeger. Direct observation of dynamic shear jamming in dense suspensions. *Nature*, 532:214–217, 2016.

[11] Endao Han, Ivo R Peters, and Heinrich M Jaeger. ARTICLE High-speed ultrasound imaging in dense suspensions reveals impact-activated solidification due to dynamic shear jamming. *Nature Communications*, 7:1–8, 2016.

[12] Sayantan Majumdar, Ivo R Peters, Endao Han, and Heinrich M Jaeger. Dynamic shear jamming in dense granular suspensions under extension. *Physical Review E*, 95:12603, 2017.

[13] B M Guy, M Hermes, and W C K Poon. Towards a Unified Description of the Rheology of Hard-Particle Suspensions. *Physical Review E*, 115:088304, 2015.

[14] Dapeng Bi, Jie Zhang, Bulbul Chakraborty, and R P Behringer. Jamming by shear. *Nature*, 480:355–358, 2011.

[15] A. Fall, F. Bertrand, D. Hautemayou, C. Meziere, P. Moucheront, A. Lemaitre, and G. Ovarlez. Macroscopic Discontinuous Shear Thickening versus Local Shear Jamming in Cornstarch. *Physical Review Letters*, 114:098301, 2015.

[16] J. John Soundar Jerome, Nicolas Vandenberghe, and Yoël Forterre. Unifying Impacts in Granular Matter from Quicksand to Cornstarch. *Physical Review Letters*, 117:098003, 2016.

[17] Eric Brown, Nicole A Forman, Carlos S Orellana, Hanjun Zhang, Benjamin W Maynor, Douglas E Betts, Joseph M Desimone, and Heinrich M Jaeger. Generality of shear thickening in dense suspensions. *Nature Materials*, 9:220–224, 2010.

[18] Jeroen Appel, Sabine Akerboom, Remco G Fokkink, and Joris Sprakel. Facile One-Step Synthesis of Monodisperse Micron-Sized Latex Particles with Highly Carboxylated Surfaces. *Macromolecular Rapid Communications*, 34:1284–1288, 2013.

[19] Erica E Bischoff White, Manoj Chellamuthu, Jonathan P Rothstein, E E Bischoff White, · M Chellamuthu, and · J P Rothstein. Extensional rheology of a shear-thickening cornstarch and water suspension. *Rheol Acta*, 49:119–129, 2010.

[20] M I Smith, R Besseling, E Cates, and V Bertola. Dilatancy in the flow and fracture of stretched colloidal suspensions. *Nature Communication*, 1:1–5, 2010.

[21] Loreto Oyarte Gálvez, Sissi De Beer, Devaraj Van Der Meer, and Adeline Pons. Dramatic effect of fluid chemistry on cornstarch suspensions: Linking particle interactions to macroscopic rheology. *Physical Review E*, 95:30602, 2017.

[22] Abhinendra Singh, Romain Mari, Morton M Denn, and Jeffrey F Morris. A constitutive model for simple shear of dense frictional suspensions. *Journal of Rheology*, 62:405, 2018.

[23] Jianbin Qin, Guangcheng Zhang, Zhonglei Ma, Jiantong Li, Lisheng Zhou, and Xuetao Shi. Effects of ionic structures on shear thickening fluids composed of ionic liquids and silica nanoparticles †. *RSC Advances*, 6:81913–81923, 2016.

[24] Justin Warren, Sean Offenberger, Hossein Toghiani, Charles U Pittman, Thomas E Lacy, and Santanu Kundu. Effect of Temperature on the Shear-Thickening Behavior of Fumed Silica Suspensions. *Applied Materials & Interfaces*, 7:18650–18661, 2015.

[25] Jean Comtet, Guillaume Chatté, Antoine Niguès, Lydéric Bocquet, Alessandro Siria, and Annie Colin. Pairwise frictional profile between particles determines discontinuous shear thickening transition in non-colloidal suspensions. *Nature Communications*, 8:1–7, 2017.

[26] François Boyer, Enrique Sandoval-Nava, Jacco H Snoeijer, J Frits Dijksman, and Detlef Lohse. Drop impact of shear thickening liquids. *Physical Review Fluids*, 1:13901, 2016.

[27] Rijan Maharjan and Eric Brown. Giant deviation of a relaxation time from general-

ized Newtonian theory in discontinuous shear thickening suspensions. *Physical Review Fluids*, 2:123301, 2017.

[28] Endao Han, Nigel Van Ha, and Heinrich M Jaeger. Measuring the porosity and compressibility of liquid-suspended porous particles using ultrasound. *Soft Matter*, 13:3506–3513, 2017.

CHAPTER 4

TUNING INTERPARTICLE HYDROGEN BONDING IN SHEAR-JAMMING SUSPENSIONS: KINETIC EFFECTS AND CONSEQUENCES FOR TRIBOLOGY AND RHEOLOGY

4.1 Introduction

In Chapter 3, we took a microstructural look into the prevailing phenomenological model for discontinuous shear thickening (DST) [1, 2], and shear jamming (SJ) [3, 4], which focuses on how DST and SJ depend on interparticle friction [5, 6]. While suspended particles can slide past another at low shear, beyond a critical shear stress the hydrodynamic lubrication layers between particles break and the resulting frictional contacts generate transient (DST) or stable (SJ) networks of force chains [7]. Increasing the effective friction coefficient characterizing these contacts is predicted to increase the range of particle packing fractions over which DST and SJ are observable. Chapter 3 showed that from an experimental standpoint, friction can be controlled through tuning the chemical interactions between particles, notably interparticle hydrogen bonding [13]. Other work has also shown that interparticle friction can be controlled by coating the particle surface with polymer layers of varying lubricity [8, 9, 5] or by modifying the surface topography, *e.g.* by controlling surface roughness [10, 11, 12]. Distinct from hese studies however, hydrogen bonding also introduces a short-ranged adhesion, or "sticking" force. This force differs from irreversible, longer-ranged attractive particle-particle interactions, which typically lead to shear-induced flocculation and the development of a yield stress [14], in that it is activated only when the lubrication

The research described in this chapter has been submitted for publication. A pre-print is available on arXiv: James, N. M., Hsu, C. P., Spencer, N. D., Jaeger, H. M., and Isa, L. Tuning Interparticle Hydrogen Bonding in Shear-Jamming Suspensions: Kinetic Effects and Consequences for Tribology and Rheology. arXiv:1901.04904 [cond-mat.soft]. C. P. Hsu conducted the AFM experiments.

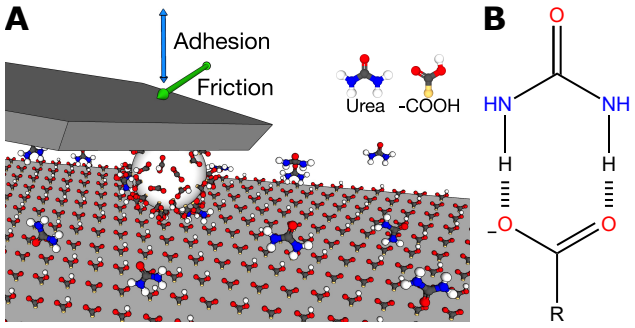

Figure 4.1: A. Schematic of a PMMA/ITA colloidal probe on a carboxylate-functionalized substrate in the presence of urea. The blue arrow indicates the cantilever movement while performing the adhesion measurements. The green arrow indicates the scanning direction while performing the friction measurements. B. Representation of a possible coordination structure between urea and a carboxyl group. The hashed bonds represent hydrogen bonding interactions.

layer is broken and is fully reversible when the local shear stress falls below the critical level. Such stress-dependent, reversible sticking is not accounted for in currently available models, and the manner in which it affects the inter-particle friction coefficient has remained an open question.

In this Chapter, we address this by conducting liquid cell, colloidal-probe atomic force microscopy (AFM) studies to measure friction and adhesion between PMMA/ITA colloids (diameter $d \approx 0.8$ μm), as a function of the solvent urea concentration, and connect these findings to both the chemical microstructure and the macroscopic flow behavior through NMR and and rheological studies, respectively.

4.2 Results and Discussion

A schematic of the AFM experimental setup is shown in Figure 4.1A. The PMMA/ITA colloidal probes used for friction and adhesion measurements are fabricated by attaching a PMMA/ITA particle to the end of a tip-less AFM cantilever (NSC36/Tipless, MikroMasch, Estonia) with a home-built micro-manipulator coupled to a microscope (BX 41, Olympus microscope, Japan). A small amount of epoxy glue is picked up with a sharpened tungsten wire (Wire.Co.UK, UK) and spread on the end of the tip-less AFM cantilever using a micro-

manipulator. After that, a PMMA/ITA particle is picked by another sharpened tungsten wire and is affixed precisely over the epoxy glue.

The substrate is a carboxylate-functionalized glass slide (AutoMate Scientific Inc.), selected to mimic the surface chemistry of the particle in order to provide a chemically symmetric contact. AFM measurements are conducted with the particle and substrate immersed in the same suspending solvent used for the rheological measurements, 69% aqueous glycerol (v/v), with urea concentration varied from 0-6 M.

As previously mentioned, urea interferes with the formation of hydrogen bonds between the scanning probe and the substrate, possibly following the scheme shown in Figure 4.1B [15, 16]. We hereby study how this bond formation affects adhesion and friction between carboxylated surfaces.

The friction measurements are carried out using lateral force microscopy by scanning the substrate in the direction orthogonal to the cantilever axis. The scan area and scan rate are fixed at 2 μm $\times$ 400 nm (128 px $\times$ 26 px) and 0.5 Hz, respectively. The corresponding scanning speed is 1 μm/s, in order to avoid that viscous drag had any impact on the lateral deflection of the cantilever. The friction measurements are performed 5, 15, and 25 minutes after the system was immersed in 69% glycerol/water (v/v), with urea concentration varied from 0-6 M. At every scanning area, the friction loops are recorded at different applied loads L from 10 nN to 60 nN.

The friction forces as a function of L, with and without urea present, are shown in Figure 4.2A for different waiting times prior to scanning. From the data, we see that the 0 M urea experiments lead to overall higher frictional forces compared to the 6M case and show no time dependence. Conversely, the 6M sample shows a history dependence. At short timescales ($<$ 5 min), the 6 M urea system yields similar results to the 0 M urea case, however, as time proceeds, the frictional force decreases, stabilizing after 15 minutes of exposure to the solvent. The relation between friction force, F_{friction}, and applied load L is described by a modified version of Amontons' Law [17] as:

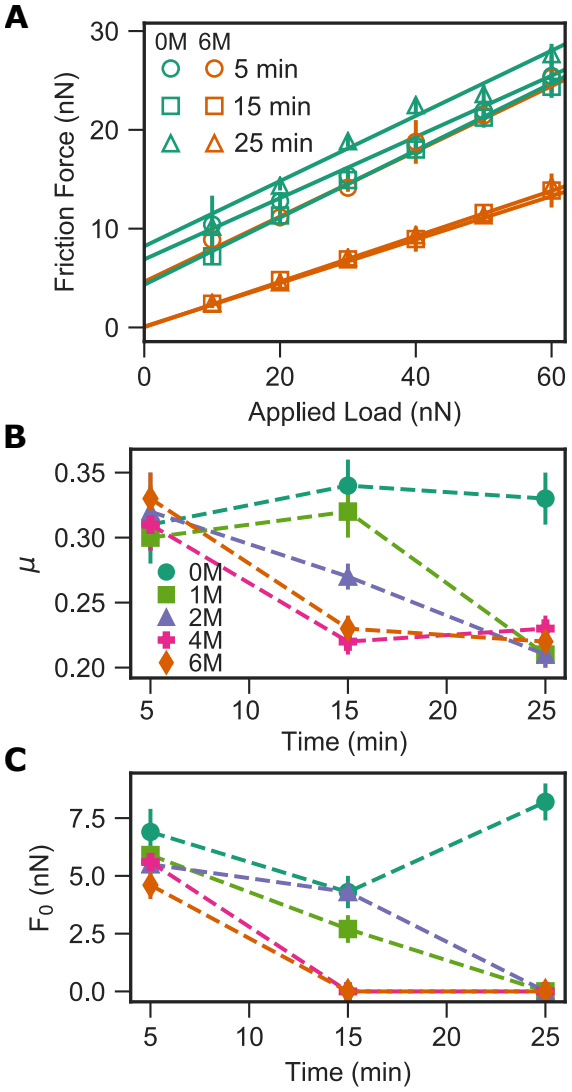

Figure 4.2: A. Friction measurements in 69% (v/v) glycerol/water at 0 M and 6 M urea concentration. Error bars represent the standard deviations across the scan area (26 data points). The legend indicates how long the particle on the cantilever has been immersed in the solvent. B. Evolution of the friction coefficients over time, for various concentrations of urea. Error bars represent the uncertainties in the calculated slope based on equation 4.1. C. Extrapolated force at 0 nN load, as a function of time for various concentrations of urea. Error bars represent the uncertainties in the calculated intercept based on equation 4.1.

$$F_{\text{friction}} = \mu \cdot (L_0 + L) = F_0 + \mu \cdot L, \tag{4.1}$$

where a constant internal load L_0 is added to the applied load L to account for the intermolecular adhesive forces. F_0 represents the friction force at 0 applied load for adhesive surfaces. The friction coefficient, μ, is defined as the slope of this equation, $dF_{\text{friction}}/dL = \mu$.

The friction coefficients as a function of time and urea concentration are shown in Figure 4.2B. From these data it is clear that, in the absence of urea, the friction coefficient is stable over time, with a value of 0.33 $\pm$ 0.02. In the presence of urea, the friction coefficient reduces to 0.22 $\pm$ 0.01, a significant reduction of 34%. This was previously reported to increase the particle volume concentration at which shear jamming is possible by $\sim$ 1% [13], and it is in line with simulations that found a $\sim$ 55% change in μ to result in a $\sim$ 3% shift in the minimum particle volume concentration required for shear jamming [5]. The speed with which the system equilibrates to this reduced μ value is highly dependent on urea concentration: the 1 M urea system takes between 15-25 minutes to equilibrate, whereas the 6 M urea system takes between 5-15 minutes.

In addition to the change in friction coefficient associated with urea concentration, here we also find a marked difference in adhesion, as implied by the non-zero value of the extrapolated friction force at 0 nN applied load, F_0 [18]. In Figure 4.2C, we show that F_0 bears the same urea- and time-dependence as that shown for μ in Figure 4.2B. This is consistent with the nature of the hydrogen bonding, which contributes an attractive interaction between surfaces that manifests as both resistance to sliding due to the constraints of bond lengths and bending, as well as interparticle adhesion. In this way, adhesion is coupled into the friction coefficient, giving rise to the similarity in the time dependence of μ and F_0 with increasing urea concentration. The dependence of this timescale on the urea concentration suggests a chemical kinetic process influencing this transition.

We directly connect this time-dependent change in friction and adhesion to the kinetics of urea sorption on carboxylated surfaces by quantifying the change in urea concentration of the

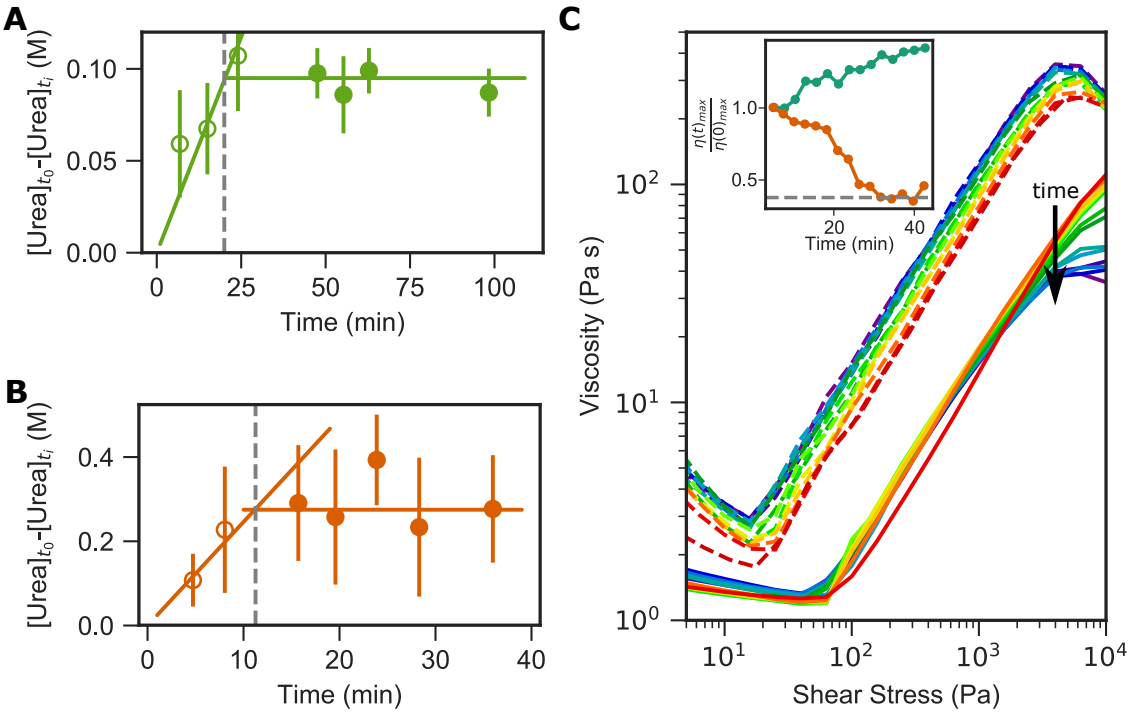

Figure 4.3: A. Equilibration timescales estimated by monitoring the magnitude of the change in urea concentration in the suspending solvent (69% glycerol), as a function of particle immersion time. The initial urea concentration $[\text{Urea}]_{t_0}$ is 1 M. The open circles show the initial sorption period, where the concentration of urea is changing as urea molecules sorb to the particle surface; the closed circles show the steady state where the particle surface is saturated. The intersection of these two regimes suggests a timescale of $\sim$ 20 minutes (indicated by the gray dashed line) for the sorption process of dilute particles in 1 M urea. B. Equilibration timescales of dilute particles in 6 M urea. The intersection of the initial and steady state regimes suggests a timescale of $\sim$ 11.25 minutes (indicated by the gray dashed line). C. Rheology data as a function of time for 56% PMMA/ITA microspheres in 69% glycerol with 0M urea (dashed lines) and 6M urea (solid lines). Flow curves are taken sequentially over time ($\sim$2.5 minutes per flow curve); time increases from red to purple. Inset: the maximum viscosity at the peak of shear thickening, normalized by the initial (red) maximum viscosity, as a function of time, for 69 % glycerol with 0 M urea (teal) and 6 M urea (orange).

suspending solvent over time. From an initial exposure to urea at $t = t_0$, the concentration of urea in the suspending solvent decreases as it binds to the particle surface. When a dynamic equilibrium is reached, the urea concentration in the suspending solvent stabilizes over time. We measure this by exposing $\sim$ 1 g of PMMA/ITA particles to $\sim$ 5 mL of suspending solvent, under vigorous stirring. At various timepoints, we withdraw $\sim$ 0.1 mL of suspending solvent and filter out the PMMA/ITA particles using a sterile, polyvinylidene fluoride syringe filter with a pore size of 0.22 μm (Fisher). Approximately 0.03 g of suspending solvent is recovered, which is then diluted with 0.4 mL of deuterated dimethyl sulfoxide (DMSO-d_6), and 20 μL of 1,2-dichlorobenzene is added as an internal standard. Urea is quantified by ^{1}H NMR (number of acquisitions = 16, relaxation delay = 20 sec). These results are shown in Figure 4.3 for 1 M urea (Figure 4.3A) and 6 M urea (Figure 4.3B). Error bars indicate propagated uncertainties. We identify the system as equilibrated when the the change in urea concentration, $[\text{urea}]_{t_0} - [\text{urea}]_{t_i}$ has stabilized (indicated by filled circles). Time points before this point indicate states where urea continues to sorb onto the particle surface (indicated by open circles). By estimating the intersection of these regimes we identify an estimated timescale associated with the equilibration of the sorption process. This timescale is $\sim$ 20 minutes for 1 M urea, and $\sim$ 11.25 minutes for 6 M urea. These values are in good agreement with the timescales for the stabilization of μ and F_0, identified to be between 15-25 minutes and 5-15 minutes, respectively. Thus, we conclude that the time-dependent evolution of the friction coefficient and the adhesion in the system is due to the sorption kinetics of urea on the PMMA/ITA particle surface.

We connect this with the macroscopic rheological properties of the suspension by rapidly measuring sequential flow profiles with and without urea present. These results are shown in Figure 4.3C. As time proceeds (from red to purple), the 0 M suspension (dotted lines) shows only a slight increase in baseline viscosity over all shear stresses, attributed to solvent evaporation [19]. Solvent evaporation increases the suspension packing fraction, resulting in a higher viscosity. Thus, we conclude that there is no significant change in the flow behavior

of the 0 M urea suspension over time.

In contrast, the 6 M urea suspension (solid lines) shows marked differences. First, we see no evaporation for the 6 M urea suspension, which we attribute to the reduction in solvent vapor pressure due to the presence of concentrated urea. Additionally, in the presence of urea, the shear-thinning branch is suppressed, and the thickening onset shifts to higher stresses. Both these effects show no time dependence, so we attribute them to solvated (not sorbed) urea. The presence of urea in solution can screen interparticle attractions that result in shear thinning. Additionally, as we discuss later, the presence of solvated urea could increase the force necessary to push particles into contact, increasing the stresses necessary to achieve direct contact and thus increasing the stress onset of shear thickening.

In addition to these immediate, time-independent repercussions of the urea presence, we also see a striking time-dependence of the high-shear rheology: as time proceeds, the upper branch of the shear thickening regime decreases in viscosity. This is particularly important as the high-shear behavior is understood to result directly from the frictional interparticle interactions after hydrodynamic lubrication has broken down. Thus time-dependent changes in interparticle friction will be expected to result selectively in changes to the high-shear rheology. Indeed, the upper Newtonian plateau predicted by the Wyart-Cates model [20] decreases as time proceeds. The upper viscosity, $\eta_{\max}$, is plotted relative to the first time-point (red curves) for both systems in the inset to Figure 4.3C. Here we can see that for 0 M urea, the upper viscosity increases over time, consistent with evaporation. In contrast, for 6 M urea, the upper viscosity decreases by nearly 60% over time, stabilizing around $t = 25$ min. The viscosity is determined by the proximity of the suspension packing fraction ϕ to the relevant jamming packing fraction, ϕ_J, as described by the Krieger-Dougherty relation [21]:

$$\eta = \eta_0(1 - \frac{\phi}{\phi_J})^{-\beta}, \tag{4.2}$$

where η is the suspension viscosity, η_0 is the pure solvent viscosity, and β is a parameter

typically close to 2 [22, 23]. In the case of the higher-shear, friction-dominated rheology, the relevant jamming packing fraction is the frictional packing fraction ϕ_m. A lower maximum viscosity indicates ϕ is farther from ϕ_m. Since ϕ is held constant, this indicates that ϕ_m must be increasing over time. Since an increasing friction coefficient μ reduces the frictional jamming point ϕ_m, we interpret this *increase* in ϕ_m to be the result of a *decrease* in the friction coefficient μ.

It is important to note that we do not anticipate the time dependence of the rheology (*i.e.* an equilibration time of 25 minutes) to match those measured in AFM and NMR studies ($\sim$ 11 min). For the AFM and NMR experiments, the concentration of particles is low enough compared to the volume of suspending solvent that the change in the background urea concentration is negligible. In the rheology experiments, where 56% of the volume of the suspension is occupied by particles, the change in the background urea concentration is no longer negligible and thus the sorption rate will slow down as the urea concentration decreases with time.

To characterize the role of urea in modifying the interparticle adhesion directly, we conduct AFM experiments to measure the adhesion between the PMMA/ITA particle and the carboxylate-functionalized substrate by measuring the pull-off force in a force-vs-distance curve. The force-vs-distance curves are recorded after 1 hour equilibration in 69% (v/v) glycerol/water at 0 M and 6 M urea concentration . At each urea concentration, 200 curves are recorded across a 20 μm $\times$ 20 μm area with the approach and retraction speed set at 500 nm/s.

Representative force-distance curves in 0 M and 6 M urea are shown in Figure 4.4A. The 0 M urea retraction curve shows the adhesion forces between the PMMA/ITA particle and the carboxylate-functionalized substrate. This adhesion is due to the hydrogen bonding between the two surfaces [18, 24]. However, the 6 M urea retraction curve shows a massive reduction in the adhesion force. This demonstrates that the presence of urea can effectively deactivate the hydrogen bonding between the surfaces. Additionally, the 6 M urea approach

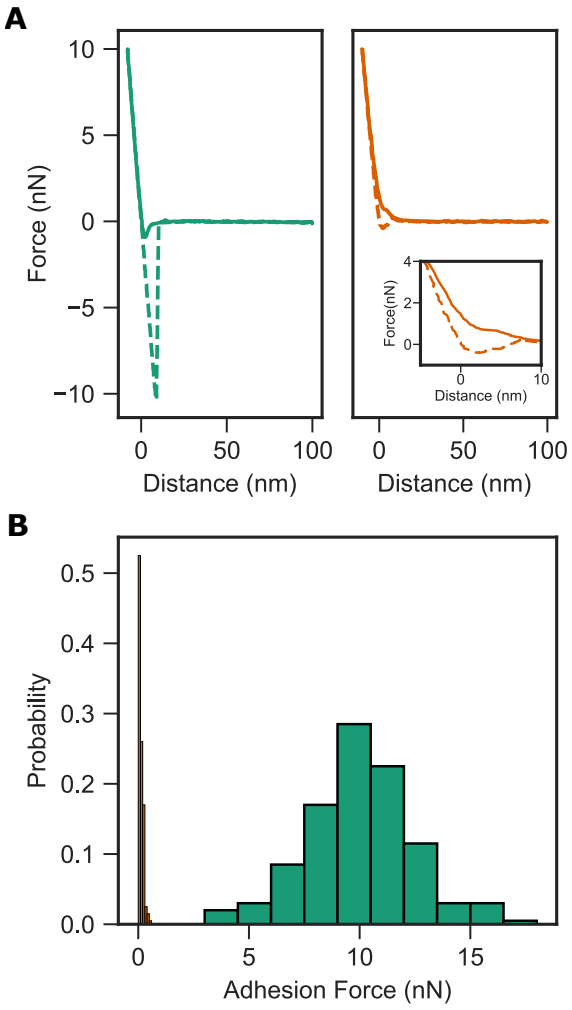

Figure 4.4: A. Approach (solid line) and retraction (dashed line) of the force-distance curves after 1 hour equilibration in 0 M urea (left) and 6 M urea (right) solutions. Inset: Zoomed-in view to visualize the repulsive shoulder at small approach distances in 6 M urea. B. Adhesion forces measured after 1 hour in 69% (v/v) glycerol/water at 0 M (teal) and 6 M (orange) urea concentration. The bin width is 1.5 nN for 0 M and 0.1 nN for 6 M.

curve shows a small repulsive shoulder when pushing the two surfaces into contact. We attribute this repulsive shoulder to the presence of solvated urea that needs to be squeezed out from the region of contact. Figure 4.4B quantitatively compares the adhesion in these systems, showing that the average adhesion of 10.0 ± 2.5 nN for 0 M urea is reduced to 0.1 nN (95% confidence interval [0.09, 0.12]) for 6 M urea.

4.3 Conclusions

From these results, a picture emerges in which PMMA/ITA particles in suspension experience hydrogen bonding-induced adhesion and enhanced friction. Urea can sorb to the particle surface and reduce this interparticle friction and adhesion. The kinetics associated with equilibration of the sorption process result in time-dependent decreases in the interparticle friction and adhesion, which induce a time-dependent decrease in the upper Newtonian viscosity. These results allow us to pinpoint urea sorption as the driving factor in the reduction of interparticle friction and adhesion, and in turn the shifted SJ regime reported in prior work [13]. We emphasize the reversible nature of this adhesion generated by particle-particle hydrogen bonds, lest aggregation and shear thinning would overwhelm the rheological response and result in a yielding-to-jamming transition as recently predicted by numerical simulations [25].

In conclusion, we presented direct evidence that chemical processes at the particle surfaces and their kinetics influence the interparticle friction and adhesion that drive the macroscopic flow behavior in dense suspensions, specifically shear jamming. The finding that large, stress-activated friction and adhesion can work in concert introduces a new aspect that so far has not been taken into account in the literature, although recent work has started to look into different kinds of constraints that contribute to the general mechanisms responsible for DST and SJ [25, 26]. This points to a need for more detailed modeling to map out how adhesion modifies the state diagram that delineates DST and SJ regimes as a function of packing fraction and applied shear stress. Our results also open up new avenues for controlling

shear jamming behavior via tuning the particle surface chemistry, in particular developing responsive systems where friction and adhesion can be engineered on demand.

BIBLIOGRAPHY

[1] H A Barnes. Shear-Thickening ("Dilatancy") in Suspensions of Nonaggregating Solid Particles Dispersed in Newtonian Liquids. *The Journal of Rheology*, 33:329–367, 1989.

[2] Eric Brown, Nicole A Forman, Carlos S Orellana, Hanjun Zhang, Benjamin W Maynor, Douglas E Betts, Joseph M Desimone, and Heinrich M Jaeger. Generality of shear thickening in dense suspensions. *Nature Materials*, 9:220–224, 2010.

[3] M I Smith, R Besseling, E Cates, and V Bertola. Dilatancy in the flow and fracture of stretched colloidal suspensions. *Nature Communication*, 1:1–5, 2010.

[4] Ivo R Peters, Sayantan Majumdar, and Heinrich M Jaeger. Direct observation of dynamic shear jamming in dense suspensions. *Nature*, 532:214–217, 2016.

[5] Nicolas Fernandez, Roman Mani, David Rinaldi, Dirk Kadau, Martin Mosquet, Hélè Ne Lombois-Burger, Juliette Cayer-Barrioz, Hans J Herrmann, Nicholas D Spencer, and Lucio Isa. Microscopic Mechanism for Shear Thickening of Non-Brownian Suspensions. *Physical Review Letters*, 111:108301, 2013.

[6] Ryohei Seto, Romain Mari, Jeffrey F Morris, and Morton M Denn. Discontinuous Shear Thickening of Frictional Hard-Sphere Suspensions. *Physical Review Letters*, 111:218301, 2013.

[7] Romain Mari, Ryohei Seto, Jeffrey F Morris, and Morton M Denn. Shear thickening, frictionless and frictional rheologies in non-Brownian suspensions. *Journal of Rheology*, 58:1693–1724, 2014.

[8] M. K. Vyas, K. Schneider, B. Nandan, and M. Stamm. Switching of friction by binary polymer brushes. *Soft Matter*, 4(5):1024–1032, 2008.

[9] A. Dedinaite, E. Thormann, G. Olanya, P. M. Claesson, B. Nystrom, A. L. Kjoniksen, and K. Z. Zhu. Friction in aqueous media tuned by temperature-responsive polymer layers. *Soft Matter*, 6(11):2489–2498, 2010.

[10] D. Lootens, H. van Damme, Y. Hemar, and P. Hebraud. Dilatant flow of concentrated suspensions of rough particles. *Physical Review Letters*, 95(26):268302, 2005.

[11] Lilian C. Hsiao, Safa Jamali, Emmanouil Glynos, Peter F. Green, Ronald G. Larson, and Michael J. Solomon. Rheological state diagrams for rough colloids in shear flow. *Physical Review Letters*, 119(15):158001, 2017.

[12] Chiao-Peng Hsu, Shivaprakash N. Ramakrishna, Michele Zanini, Nicholas D. Spencer, and Lucio Isa. Roughness-dependent tribology effects on discontinuous shear thickening. *PNAS*, 115(20):5117–5122, 2018.

[13] Nicole M James, Endao Han, Ricardo Arturo Lopez De La Cruz, Justin Jureller, and Heinrich M Jaeger. Interparticle hydrogen bonding can elicit shear jamming in dense suspensions. *Nature Materials*, 17:965–970, 2018.

[14] Alessio Zaccone, Hua Wu, Daniele Gentili, and Massimo Morbidelli. Theory of activated-rate processes under shear with application to shear-induced aggregation of colloids. *Phys. Rev. E*, 80:051404, Nov 2009.

[15] Benjamin P Hay, Timothy K Firman, and Bruce A Moyer. Structural Design Criteria for Anion Hosts: Strategies for Achieving Anion Shape Recognition through the Complementary Placement of Urea Donor Groups. *Journal of the American Chemical Society*, 127:1810–1819, 2005.

[16] Martin Patrick Hughes and Bradley D Smith. Enhanced Carboxylate Binding Using Urea and Amide-Based Receptors with Internal Lewis Acid Coordination: A Cooperative Polarization Effect. *J. Org. Chem*, 62:4492–4499, 1997.

[17] B. Derjaguin. Molecular theory of outer friction. *Zeitschrift Fur Physik*, 88(9-10):661–675, 1934.

[18] A. Noy, C. D. Frisbie, L. F. Rozsnyai, M. S. Wrighton, and C. M. Lieber. Chemical force microscopy - exploiting chemically-modified tips to quantify adhesion, friction, and functional-group distributions in molecular assemblies. *Journal of the American Chemical Society*, 117(30):7943–7951, 1995.

[19] Eric Brown and Heinrich M Jaeger. The role of dilation and confining stresses in shear thickening of dense suspensions. *Journal of Rheology*, 56:875–923, 2012.

[20] M Wyart and M E Cates. Discontinuous Shear Thickening without Inertia in Dense Non-Brownian Suspensions. *Physical Review Letters*, 112:098302, 2014.

[21] Irvin M Krieger and Thomas J Dougherty. A Mechanism for Non-Newtonian Flow in Suspensions of Rigid Spheres. *Transactions of the Society of Rheology*, 3:137–152, 1959.

[22] D Quemada. Rheology of concentrated disperse systems and minimum energy dissipation principle I. Viscosity-concentration relationship. *Rheologica Acta*, 16:82–94, 1977.

[23] E Degiuli, G Düring, E Lerner, and M Wyart. Unified theory of inertial granular flows and non-Brownian suspensions. *Physical Review E*, 91:62206, 2015.

[24] S. K. Sinniah, A. B. Steel, C. J. Miller, and J. E. ReuttRobey. Solvent exclusion and chemical contrast in scanning force microscopy. *Journal of the American Chemical Society*, 118(37):8925–8931, 1996.

[25] Abhinendra Singh, Sidhant Pednekar, Jaehun Chun, Morton M. Denn, and Jeffrey F. Morris. From yielding to shear jamming in a cohesive frictional suspension. *arXiv:1809.06020*, 2018.

[26] B. M. Guy, J. A. Richards, D. J. M. Hodgson, E. Blanco, and W. C. K. Poon. Constraint-based approach to granular dispersion rheology. *Phys. Rev. Lett.*, 121:128001, Sep 2018.

CHAPTER 5

DISCONTINUOUS SHEAR THICKENING AND SHEAR JAMMING IN ANISOTROPIC SYSTEMS

5.1 Introduction

As discussed previously, shear jamming (SJ) [1, 2] and discontinuous shear thickening (DST) [3] are both understood to depend heavily on interparticle friction [4, 5, 6, 7, 8, 9]. To summarize, the prevailing models [10, 11, 12] provide a stress-dependent mechanism that drives these phenomena: at low applied shear, most particles in the suspension are lubricated by solvent layers, thus only weak thickening is observed. As more particles are added the frictionless jamming packing fraction ϕ_0 governs the onset of rigidity. At high applied shear, a large fraction of particles are forced into close proximity, such that the lubrication layer ruptures or is reduced to molecular length-scales, at which point the continuum models describing lubrication break down. As a result, particles are effectively in direct contact and experience friction. In the presence of frictional interactions, jamming can now occur at a minimum jamming packing fraction ϕ_m less than ϕ_0. In this way, a suspension that is fluid-like at rest or low applied shear, *i.e.*, has a packing fraction $\phi < \phi_0$, can be sheared into a jammed state as long as $\phi > \phi_m$. In other words, shear jamming can be observed for any ϕ such that $\phi_0 > \phi > \phi_m$. In contrast to shear-induced aggregation [13], the stress dependence of the frictional interactions means that shear jamming is reversible [14, 15]: when the applied stress is removed, the suspension relaxes back to the fluid state.

Shear thickening and shear jamming make dense suspensions are challenging for industrial

The research described in this chapter has been submitted for publication. A preprint is available on arXiv: James, N. M., Xue, H., Goyal, M., and Jaeger, H. M. Controlling Shear Jamming in Dense Suspensions via The Particle Aspect Ratio. arXiv:1901.04051 [cond-mat.soft]. H. Xue and M. Goyal assisted with the particle synthesis; H. Xue performed the particle size and shape comparison.

processing, which frequently involves anisotropic particles. Additionally, shear thickening and shear jamming are also of particular interest for protective wear applications that rely on the material's unique dynamic response [16, 17, 18, 19, 20]. In all these cases, it is highly desirable to control the onset of thickening or jamming, which involves an understanding of how the key parameters ϕ_0 and ϕ_m depend on particle-level properties such as interparticle friction and particle shape. On geometric grounds, we can expect that increasing the particles' aspect ratio by elongating them into rods will increase the number of (frictionless) contacts with neighboring particles and therefore reduce ϕ_0. This is borne out by prior work on rod-shaped colloids [21] and dry granular materials [22], which investigated the limit of low applied stress up to yielding or the shear thinning regime just beyond yielding. Due to the velocity gradient under shearing, however, rod-like particles will tend to align and *a priori* it is not clear whether shear thickening will be enhanced or diminished as particle aspect ratio increases. Nevertheless, increasing aspect ratio has been found to lower the particle concentration at which shear thickening becomes observable [23, 24, 25]. Still, as far as control over the shear jamming regime is concerned, the understanding of the interplay of particle friction and shape remains very much incomplete. In particular, while strong frictional interactions appear to be required in order to observe shear jamming across an appreciable packing fraction interval $[\phi_m, \phi_0]$, how particle shape can affect ϕ_m has not been investigated in either simulations or experiments.

Here we report on experiments that aim to disentangle the effects of friction and anisotropic particle shape. We recently demonstrated that the high degree of friction required for suspension shear jamming can be introduced through the interparticle hydrogen bonding capacity [26]. This allows us to intentionally design shear jamming behavior into a model system where shape can be altered by changing the particle synthesis conditions, while fixing the surface chemistry to insure that particles retain the same frictional interactions.

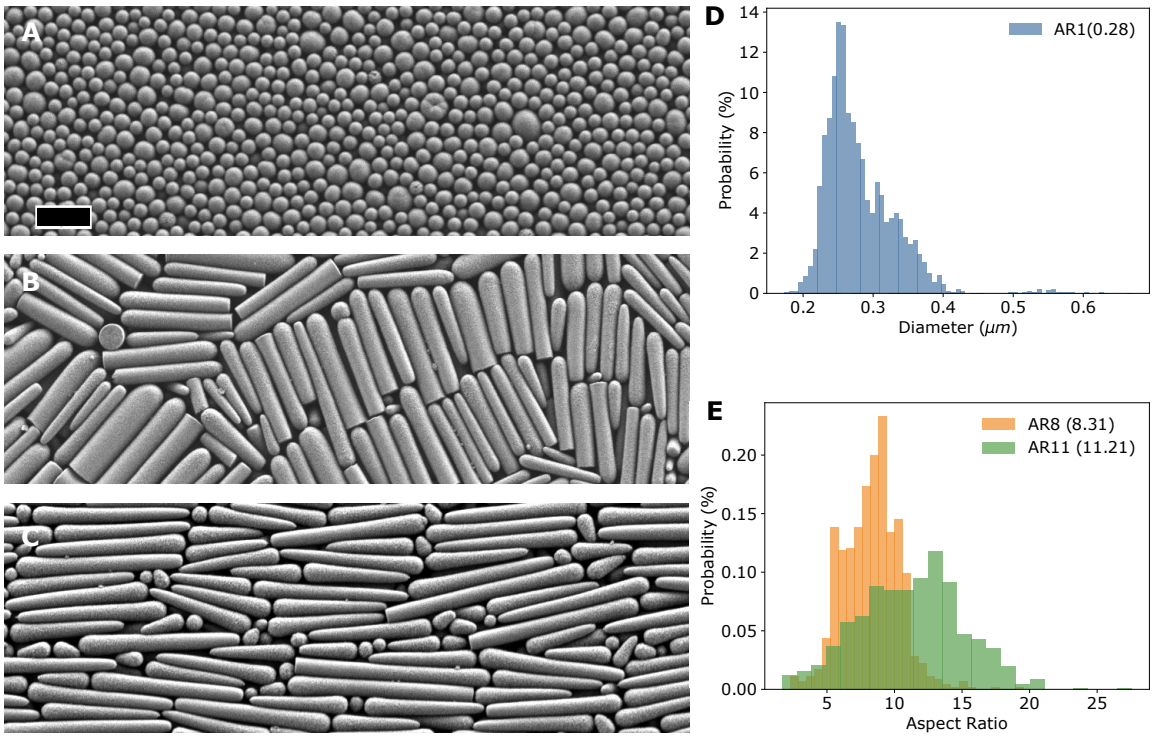

Figure 5.1: SEM images and characterization for AR1, AR8 and AR11 particle systems. A. AR1 spheres (scale bar indicates 1 μm), B. AR8 rods, and C. AR11 rods. The scale bar in A. applies to subplots A-C. D. Diameter distribution for AR1 spheres. E. Aspect ratio distribution for AR8 rods and AR11 rods. The mean aspect ratio for each system is stated in parentheses.

5.2 Results and Discussion

We employ an emulsion-based synthesis of silica rods [27]. This synthesis results in bullet-shaped rods of ∼250 nm diameter and controllable length, In aqueous solvents the silanol (Si-OH) surface groups enable strong frictional interactions via particle-particle hydrogen bonding [26]. Particle sizes and shapes are characterized by scanning electron microscopy and image analysis. Here we discuss results for three characteristic systems, each with a different aspect ratio Γ (length-to-diameter): $\Gamma \approx 1$ spheres (AR1), $\Gamma \approx 8$ rods of average length 2.0 μm (AR8), and $\Gamma \approx 11$ rods of average length 2.8 μm (AR11), shown in Figure 5.1. Above an aspect ratio of roughly 11, this synthesis produces irregularly shaped or wavey rods [27].

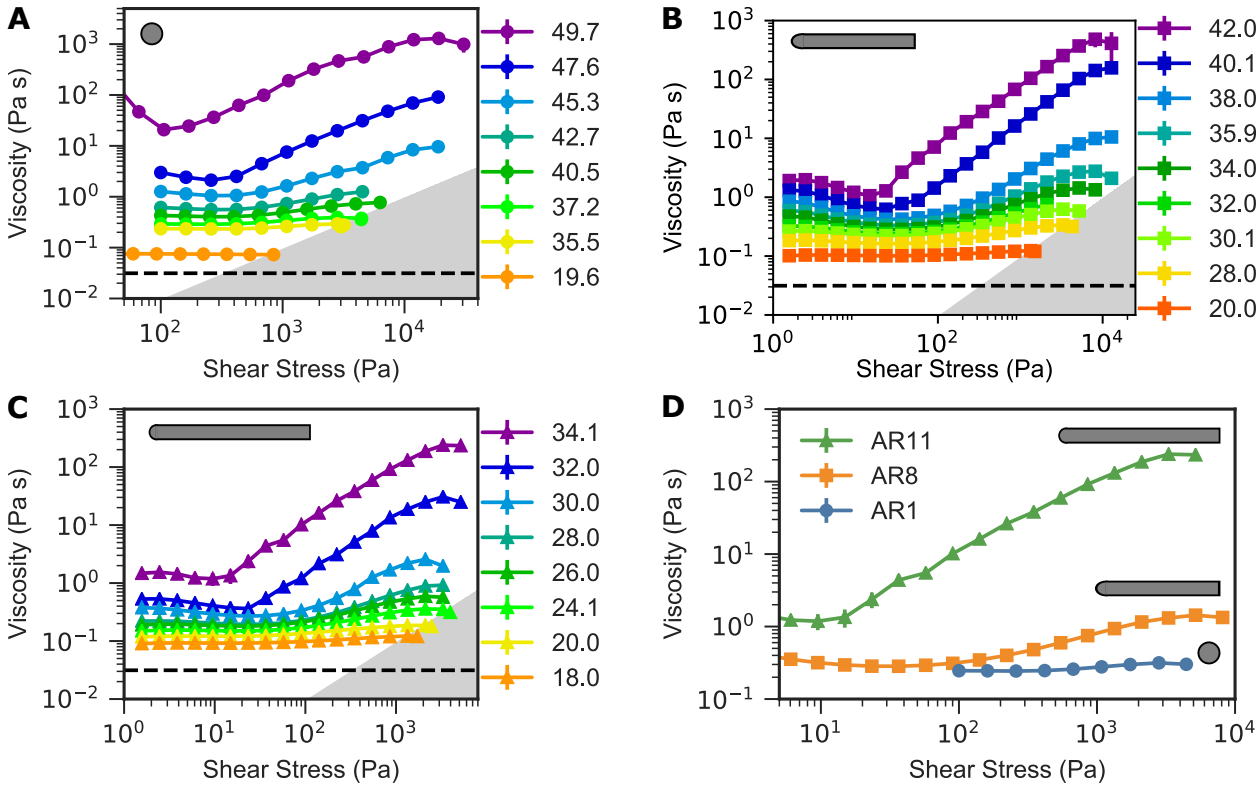

Figure 5.2: Rheological flow curves for A. spheres (AR1), B. aspect ratio 8 rods (AR8), and C. aspect ratio 11 rods (AR11), at various packing fractions ϕ (%) in 70% aqueous glycerol (v/v) with 15 mM NaCl. The dashed black line indicates the suspending solvent viscosity. Gray shaded regions indicate the rheometer's rate limit. Gray icons indicate the relative difference in aspect ratio (to scale) among the systems. D. Comparison of flow curves at ϕ=34.1 $\pm$ 0.1%, highlighting the enhancement of shear thickening with increasing aspect ratio.

We perform stress-controlled rheological measurements on suspensions of these particles. Lack of hysteresis between increasing and decreasing stress ramps was used to determine shear protocols and ensure a steady state had been adequately established. In all cases, the suspending solvent was 70% glycerol in water (v/v) with 15 mM NaCl. This solvent was selected to elicit suspension shear thickening and ensure the flow curves could be well resolved within the rheometer rate limit, indicated by the gray region in the lower-right of each plot in Figure 5.2. The AR1 system of spheres (Fig. 5.2a) shows mild shear thickening at $\phi = 35.5\%$ and strong, discontinuous shear thickening (DST) at $\phi = 47.6\%$. Note that a slope of 1 on log-log plots of viscosity versus stress as in Fig. 5.2 implies a vertical, discontinuous jump

if the same data are plotted versus shear rate. Concentrated packing fractions approaching $\phi = 50\%$ can be prepared and remain fluid-like. In contrast, the AR8 system (Fig. 5.2b) exhibits mild shear thickening as early as $\phi = 28.0\%$, and strong DST that spans over two orders of magnitude in viscosity, at only $\phi = 40.1\%$. Following this trend, the AR11 system (Fig. 5.2c) shows mild shear thickening at $\phi = 18.0\%$, and DST at only $\phi = 30.0\%$. To highlight the significance of this, DST with spheres typically requires packing fractions in excess of $\phi = 50\%$.

The drastic enhancement of thickening behavior with aspect ratio at a given packing fraction is in agreement with prior studies [23, 24, 25] and is shown in Figure 5.2d by comparing the three systems at $\phi = 34.1 \pm 0.1\%$. While the AR1 system only very slightly shear thickens, the AR11 system already shows DST.

We now analyze the flow curves in Fig. 2 to extract the stress-dependent jamming packing fractions as a function of aspect ratio. To do this, we follow prior work [10, 11, 28] and employ a Krieger-Dougherty-type relation [29] between suspension viscosity and packing fraction

$$\eta_r = (1 - \frac{\phi}{\phi_J})^{-\beta}, \tag{5.1}$$

where η_r is the suspension viscosity rescaled by the suspending solvent's viscosity, ϕ_J is the jamming packing fraction of interest: ϕ_0 in the frictionless low-shear limit or ϕ_m in the frictional high-shear limit. The exponent β is a fitting parameter that is generally taken to be ≈ 2 [30, 31, 11, 28].

We identify ϕ_0 as the particle concentration at which the low-shear Newtonian viscosity (taken to be the minimum viscosity if shear thinning is present) diverges as a function of packing fraction. From graphs as in Fig. 5.3a, where we plot ${\eta_r}^{-1/\beta}$ as a function of ϕ, we can read off ϕ_0 as the intercept with the horizontal axis. Using $\beta = 2$ as the value that best linearized the data in such plot, this leads to $\phi_0(\text{AR1}) = 55.7\%$. Upon increasing the aspect ratio of the particles eight-fold, this decreases to $\phi_0(\text{AR8}) = 50.6\%$. Increasing aspect ratio

further to 11 decreases ϕ_0 again by nearly 5 points, to $\phi_0(\mathrm{AR11}) = 45.2\%$.

Similarly, we use Equation 1 to extract the frictional jamming packing fraction ϕ_m by considering the high-shear viscosity at the upper end of shear thickening (5.3b), taking the maximum viscosity. In this case, $\beta = 1.8$ best linearized the data. For some of the highest packing fractions the suspensions were so easily driven into the shear jammed state that it was experimentally unclear if shear jamming, together with slip, occurred already just beyond the viscosity minimum (note that a solid-like, fully shear jammed state cannot be probed reliably with a steady-state viscosity measurement [32, 28]. Therefore, to obtain ϕ_m via extrapolation we only use data for $\phi(\mathrm{AR1}) < 45.3\%$, $\phi(\mathrm{AR8}) < 38.0\%$, and $\phi(\mathrm{AR11}) < 30.0\%$. As the aspect ratio Γ increases from 1 to 8 to 11, ϕ_m is found to decrease from 48.8% to 38.6% to 32.8%, respectively. This large reduction by 16 percentage points in ϕ_m from changing particle anisotropy stands in stark contrast to the small, $\sim$1% shift in ϕ_m observed when the effective, hydrogen-bonding-induced interparticle friction was changed by a factor 2 [26].

The packing fraction range over which shear jamming is observable is given by the interval from ϕ_m to ϕ_0. Figure 5.3c shows that this range nearly doubles as the aspect ratio Γ is increased from 1 to 8. A further increase from 8 to 11 delivers only a modest enhancement.

To show these changes with aspect ratio more directly, we construct state diagrams that delineate the regimes for discontinuous shear thickening (DST) and shear jamming (SJ) as a function of packing fraction ϕ and applied shear stress τ. We base these diagrams on the model by Wyart and Cates [10], assuming infinitely hard particles and taking as input parameters the values of ϕ_m and ϕ_0, obtained from Fig. 3, as well as the characteristic stress τ^* at which the lubrication layers between particles break down and frictional interactions switch on. This stress value is obtained by quantitatively matching flow curves predicted by the Wyart-Cates model with data from Fig. 2, as was done in Ref. [24]. In these state diagrams, shown in Fig.4, ϕ_0 is the left boundary of the regime (grey) where jamming occurs in the absence of shear simply by increasing particle density, while ϕ_m is the leftmost boundary of the SJ regime (green). The DST regime is indicated by the red color.

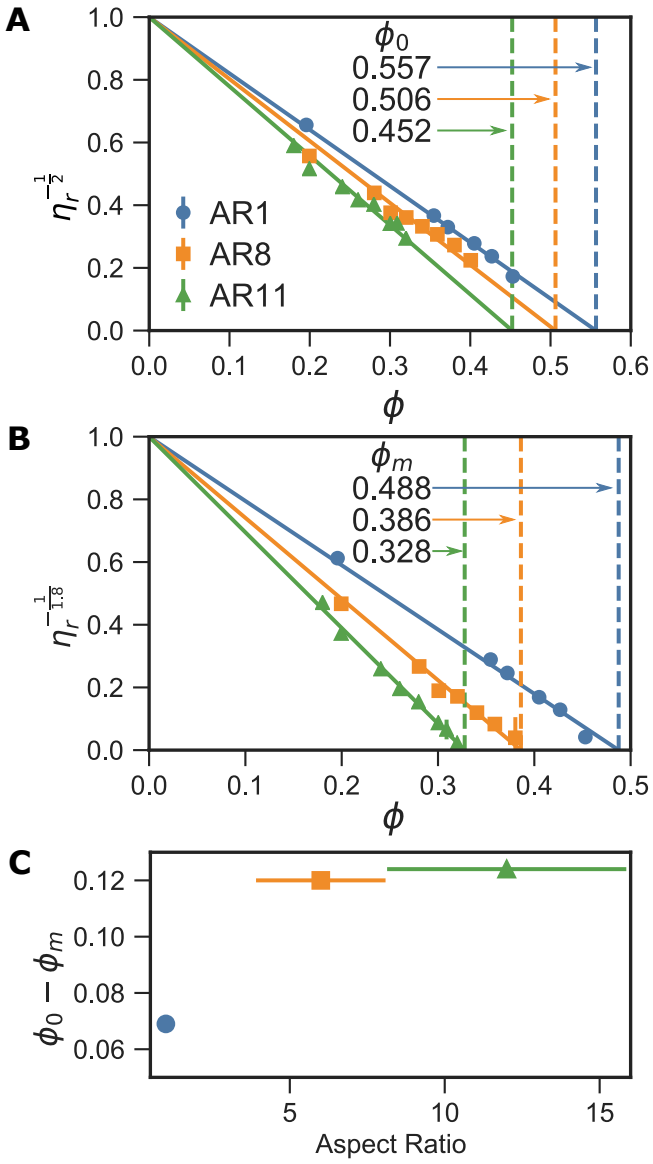

Figure 5.3: A. Rescaled minimum low-shear viscosities as a function of packing fraction, enabling the determination of the frictionless jamming point ϕ_0 from linear least squares analysis. B. Rescaled maximum high-shear viscosities as a function of packing fraction, enabling the determination of the frictional jamming point ϕ_m from linear least squares analysis. In both A and B the exponent β was chosen to optimize the fit for all three curves. C. Dependence of the shear jamming packing fraction range, $\phi_0 - \phi_m$, on particle aspect ratio.

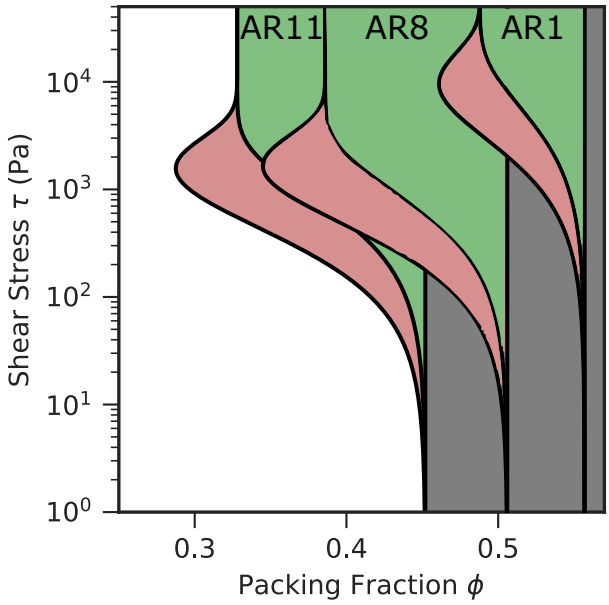

Figure 5.4: State diagrams for the AR11, AR8, and AR1 systems, showing regions that exhibit DST (red), shear jamming (green), or jammed-at-rest (gray) behavior.

In many suspensions of spherical particles that exhibit pronounced DST, an SJ regime is not readily observed [26]. This is either because the frictional interactions are weak, so that ϕ_m is extremely close to ϕ_0 and it becomes difficult to prepare a suspension that is not already jammed a rest, or because τ^* is so large that the stress required for SJ at any concentration ϕ less than ϕ_0 becomes prohibitive. As Fig. 4 shows, the frictional interactions produced via the surface functionalization of the particles in this work, by contrast, generate a wide packing fraction interval for SJ already at aspect ratio Γ=1. Referring back to the flow curves in Fig. 2 we note that, beyond increasing the effective friction via short-range, stress-dependent hydrogen bonding, this surface functionalization does not also introduce significant longer-ranged attractive forces, which would have led to large yield stresses and a pronounced shear thinning regime [33, 25].

The state diagrams highlight that increasing Γ not only shifts ϕ_0 and ϕ_m to lower values and enlarges the packing fraction range for DST and SJ, but also lowers the shear stress required to enter the DST and SJ regimes by almost a factor of 10. Since all particles have the same surface functionalization this clearly demonstrates the independent role of

the aspect ratio and the possibilities this opens up to control the location and extent of the DST and SJ regimes as a function of ϕ and τ. In fact, compared to tuning the frictional interactions for fixed spherical shape, [26] the effect achievable by changing the aspect ratio Γ is strikingly large. Interestingly, most of this effect occurs up to Γ=8, while further increase of the aspect ratio does not appear to reduce the onset stress for SJ in any significant way and simply shifts the $[\phi_m, \phi_0]$ interval to lower values.

5.3 Conclusion

In summary, building off of recent work [26], we synthesize smooth silica particles and design the particle surface chemistry to generate strong frictional interactions such that dense, aqueous suspensions exhibit pronounced shear jamming. We then vary particle aspect ratio from $\Gamma = 1$ (spheres) to $\Gamma = 11$ (slender rods), and perform rheological measurements to determine the effect of particle anisotropy on the onset of shear jamming and its precursor, discontinuous shear thickening. In this way we keep the surface and frictional particle interactions constant, and isolate the role of particle shape, in the form of aspect ratio.

Due to how the number of potential particle contacts varies with increasing aspect ratio, increasing aspect ratio may be expected to reduce ϕ_0. However, under shearing particles experience a velocity gradient which typically works to align particles to eachother. Particle alignment reduces opportunities for interparticle contact, and generally results in shear thinning. Thus, it is not necessarily obvious whether shear thickening will be enhanced or diminished as particle aspect ratio increases. Here we find that increasing aspect ratio significantly reduces ϕ_m, enhancing SJ such that it may be observed at packing fractions as low as $\phi = 33\%$ for $\Gamma = 11$. Similarly, DST can be observed as low as $\phi = 30\%$ for $\Gamma = 11$, a concentration often considered to be 'semi-dilute' rather than dense. These results stand in stark contrast to recent work [33, 25] with similar rodlike particles, which shows shear thinning of gel behavior for similar particles. This highlights the importance of the particle surface and suspending solvent in enabling DST and SJ behavior that is then highly tunable

with particle shape.

These findings provide an important experimental baseline for extending current models and simulations of dense suspensions to anisotropic particle shapes. They also provide new opportunities to design and optimize stress-adaptive materials that take advantage of DST and SJ, as used for example in protective wear or personal protective equipment that reduce injury due to impact [17, 16, 20, 18, 19]. In such applications, it can be advantageous to obtain pronounced shear thickening and reversible, jamming-induced solidification with only a small amount of added particles.

BIBLIOGRAPHY

[1] Eric Brown and Heinrich M. Jaeger. Dynamic jamming point for shear thickening suspensions. *Phys. Rev. Lett.*, 103:086001, 2009.

[2] Ivo R Peters, Sayantan Majumdar, and Heinrich M Jaeger. Direct observation of dynamic shear jamming in dense suspensions. *Nature*, 532:214–217, 2016.

[3] R.L. Hoffman. Discontinuous and dilatant viscosity behavior in concentrated suspensions . i. observation of a flow instability. *Trans. Soc. Rheol.*, 166:155–173, 1972.

[4] Nicolas Fernandez, Roman Mani, David Rinaldi, Dirk Kadau, Martin Mosquet, Hélène Lombois-Burger, Juliette Cayer-Barrioz, Hans. J Herrmann, Nicholas D. Spencer, and Lucio Isa. Microscopic mechanism for shear thickening of non-brownian suspensions. *Phys. Rev. Lett.*, 111:108301, 2013.

[5] Neil Y C Lin, Ben M Guy, Michiel Hermes, Chris Ness, Jin Sun, Wilson C K Poon, and Itai Cohen. Hydrodynamic and Contact Contributions to Continuous Shear Thickening in Colloidal Suspensions. *Physical Review Letters*, 115:228304, 2015.

[6] John R Royer, Daniel L Blair, and Steven D Hudson. Rheological Signature of Frictional Interactions in Shear Thickening Suspensions. *Physical Review Letters*, 116:188301, 2016.

[7] Romain Mari, Ryohei Seto, Jeffrey F. Morris, and Morton M. Denn. Shear thickening, frictionless and frictional rheologies in non-brownian suspensions. *J. Rheol.*, 58:1693–1724, 2014.

[8] Abhinendra Singh, Romain Mari, Morton M. Denn, and Jeffrey F. Morris. A constitutive model for simple shear of dense frictional suspensions. *J. Rheol.*, 62:457–468, 2018.

[9] Ryohei Seto, Romain Mari, Morris F. Jeffrey, and Morton M. Denn. Discontinuous shear thickening of frictional hard-sphere suspensions. *Phys. Rev. Lett.*, 111:218301, 2013.

[10] M. Wyart and M. E. Cates. Discontinuous shear thickening without inertia in dense non-brownian suspensions. *Phys. Rev. Lett.*, 112:098302, 2014.

[11] Abhinendra Singh, Romain Mari, Morton M Denn, and Jeffrey F Morris. A constitutive model for simple shear of dense frictional suspensions. *Journal of Rheology*, 62:405, 2018.

[12] Jeffrey F Morris. Lubricated-to-frictional shear thickening scenario in dense suspensions. *Physical Review Fluids*, 3:110508, 2018.

[13] Pramukta Kumar, David Gold, Daniel L Blair, Aparna Baskaran, and Jeffrey S Urbach. Shear-driven aggregation of SU-8 microrods in suspension. *Soft Matter*, 10:6514–6519, 2014.

[14] Bin Liu, Michael Shelley, and Jun Zhang. Focused Force Transmission through an Aqueous Suspension of Granules. *Physical Review Letters*, 105:188301, 2010.

[15] Scott R. Waitukaitis and Heinrich M. Jaeger. Impact-activated solidification of dense suspensions via dynamic jamming fronts. *Nature*, 487(7406):205–9, 2012.

[16] Y.S. Lee, E.D. Wetzel, and N.J. Wagner. The ballistic impact characteristics of kevlar woven fabrics impregnated with a colloidal shear thickening fluid. *J. Mater. Sci.*, 38:2825, 2003.

[17] R.G. Egres, M.J. Decker, C. J. Halbach, Y.S. Lee, N.J. Kirkwood, J.E. Wagner, and E.D. Wetzel. Stab resistance of shear thickening fluid (stf)–kevlar composites for body armor applications. *Sel. Top. Electr. Syst.*, 42:264–271, 2006.

[18] Abhijit Majumdar, Bhupendra Singh Butola, and Ankita Srivastava. Optimal designing of soft body armour materials using shear thickening fluid. *Materials and Design*, 46:191–198, 2013.

[19] Paul T Nenno and Eric D Wetzel. Design and properties of a rate-dependent 'dynamic ligament' containing shear thickening fluid. *Smart Materials and Structures*, 23:125019, 2014.

[20] Colin D Cwalina, Charles M Mccutcheon, Richard D Dombrowski, and Norman J Wagner. Engineering enhanced cut and puncture resistance into the thermal micrometeoroid garment (TMG) using shear thickening fluid (STF) – Armor^{TM} absorber layers. *Composites Science and Technology*, 131:61–66, 2016.

[21] S.R. Williams and A.P. Philipse. Random packings of spheres and spherocylinders simulated by mechanical contraction. *Phys. Rev. E.*, 67:051301, 2003.

[22] K. Desmond and Scott V. Franklin. Jamming of three-dimensional prolate granular materials. *Phys Rev E*, 73:031306, 2006.

[23] Ronald G Egres and Norman J Wagner. The rheology and microstructure of acicular precipitated calcium carbonate colloidal suspensions through the shear thickening transition. *Journal of Rheology*, 49:719–746, 2005.

[24] Eric Brown, Hanjun Zhang, Nicole A. Forman, Benjamin W. Maynor, Douglas E. Betts, Joseph M. DeSimone, and Heinrich M. Jaeger. Shear thickening and jamming in densely packed suspensions of different particle shapes. *Phys. Rev. E.*, 84:031408, 2011.

[25] Yilan Ye, Han Xiao, Kelley Reaves, Billy McCulloch, Jared F. Mike, and Jodie L. Lutkenhaus. Effect of nanorod aspect ratio on shear thickening electrolytes for safety-enhanced batteries. *Appl. Nano Mater.*, 1:2774–2784, 2018.

[26] Nicole M James, Endao Han, Ricardo Arturo Lopez De La Cruz, Justin Jureller, and Heinrich M Jaeger. Interparticle hydrogen bonding can elicit shear jamming in dense suspensions. *Nat. Mat.*, 17:965–970, 2018.

[27] Anke Kuijk, Alfons van Blaaderen, and Arnout Imhof. Synthesis of monodisperse, rodlike silica colloids with tunable aspect ratio. *J. Am. Chem. Soc.*, 133(8):2346–2349, 2011.

[28] Endao Han, Nicole M James, and Heinrich M Jaeger. Stress controlled rheology of dense suspensions using transient flows. *arXiv:1810.11887v1*, 2018.

[29] Irvin M Krieger and Thomas J Dougherty. A Mechanism for Non-Newtonian Flow in Suspensions of Rigid Spheres. *Trans. Soc. Rheol.*, 3:137–152, 1959.

[30] Samuel Maron and Percy Pierce. Application of Ree-Eyring Generalized Flow Theory To Suspensions Of Spherical Particles. *J. Coll. Sci.*, 11:80–95, 1956.

[31] D Quemada. Rheology of concentrated disperse systems and minimum energy dissipation principle I. Viscosity-concentration relationship. *Rheol. Acta.*, 16:82–94, 1977.

[32] Michiel Hermes, Ben M Guy, Wilson C K Poon, Guilhem Poy, Michael E Cates, and Matthieu Wyart. Unsteady flow and particle migration in dense, non-Brownian suspensions. *Journal of Rheology*, 60:905–916, 2016.

[33] Ryan P Murphy, Kunlun Hong, and Norman J Wagner. Thermoreversible Gels Composed of Colloidal Silica Rods with Short-Range Attractions. *Langmuir*, 32:8424–8435, 2016.

CHAPTER 6

CONCLUSION

6.1 Summary

In this work, we have contributed a microstructural understanding that complements the phenomenological model of shear jamming in dense suspensions. By examining discontinuous shear thickening (DST) and shear jamming (SJ) from a chemical perspective, we have identified and characterized a parameter through which DST and SJ can be tuned: interparticle hydrogen bonding. The phenomenological understanding of DST and SJ states that interparticle friction plays a key role in the shear-induced development of anisotropic particle force chains that provide rigity at particle concentrations ϕ below that needed for isotropic, density-induced jamming and solidification, ϕ_0. However, previous work struggled to use this model to explain why some concentrated suspensions, such as cornstarch and water, readily exhibit DST and SJ at low ϕ (*i.e* $\gtrsim 5\%$ below ϕ_0), while others do not. Here we demonstrated the importance of considering the chemical structure of the solvated particle-particle interface as particles come into close contact.

We apply the understanding that chemical surface interactions can enhance the friction between surfaces. DST and SJ require a shear-activated interparticle interaction that enhances friction, but is readily reversible when shearing forces are removed. In this work we hypothesized that interparticle hydrogen bonding, such as that likely to be encountered in sheared aqueous cornstarch suspensions, may be a promising chemical route to this effect. We proved this by synthesizing PMMA/ITA particles with high carboxylic acid surface density. We rheologically characterized the flow behaviors of these suspensions, and found they showed DST significantly more strongly than even the prototypical cornstarch suspensions. To characterize the jamming behavior of these particles, we employed 3 distinct techniques: aligned with previous efforts to distinguish SJ from DST, we performed ultrasound imaging of bulk flow under transient extension. This is an ambitious experiment requiring over 30

g of in-house synthesized particles. We then developed much more facile tensile test for SJ which allows the rapid characterization of jamming behavior with small sample sizes (< 1 g). This experiment allowed us to rapidly test the effect of a variety of solvent and particle conditions. After key control parameters were identified with this method, we performed careful rheological experiments and employed the Wyart-Cates model to analytically characterize the DST and SJ state diagram. This constituted the first experimental work to successfully employ theoretical models and rheological data to generate a state diagram of this type. A central finding is that reducing the hydrogen bonding capacity by introducing urea moves the boundary between the DST and SJ regimes in a manner that corresponds to reducing the effective, stress-dependent interparticle friction.

Through these experiments, we confirmed that interparticle hydrogen bonding capacity is indeed a key control parameter in DST and SJ. Through AFM measurements we showed that this is entirely consistent with the phenomenological model, as the chemical surface treatments also result in changes in the friction coefficient.

The new conceptual understanding that we contribute is that DST and SJ can be enhanced by interparticle hydrogen bonding as particles approach each other. We showed that this is a near-surface effect, where water facilitates the interaction, as shown in Figure 6.1. This understanding provides a powerful framework through which to engineer strong SJ behavior into new systems. This paves the way for advancements in impact mitigation and protection equipment, such as stab-resistant liquid armor and needlestick-proof medical gloves.

Following these insights, we examined a unique repercussion of the chemical nature of hydrogen bonding's contribution to friction in these suspensions: adhesion. In the "roughess" picture of friction, surface asperities provide a steric resistance to tangential sliding. They do not, however, provide any resistance to particles moving directly away from each other. There can be friction completely separate from attractive or adhesive interactions. If, however, the friction comes as a result of chemical interactions such as hydrogen bonding, friction

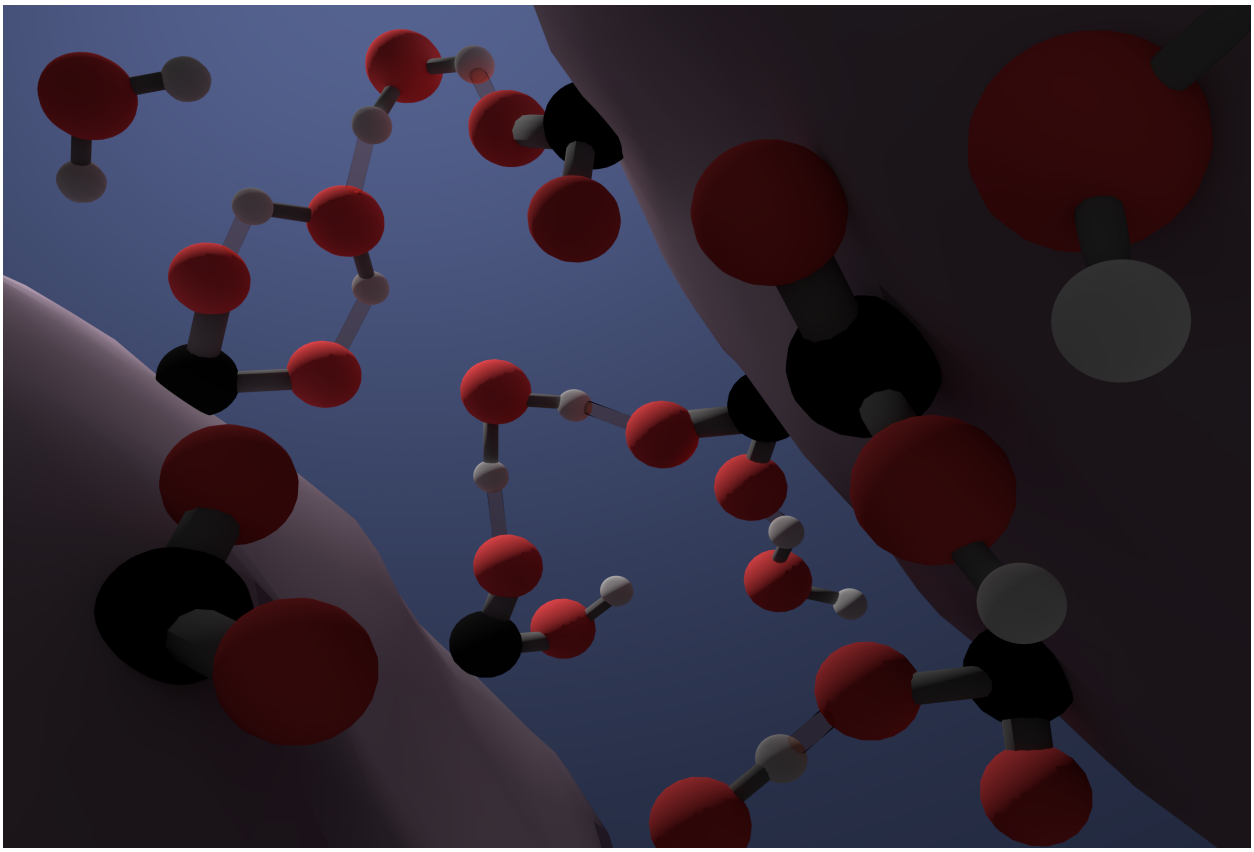

Figure 6.1: Conceptual, computer-generated representation of the chemical perspective of how interparticle hydrogen bonding manifests as particles come into close contact, increasing the resistance to tangential motion and thus friction. Black spheres represent carbon, red spheres represent oxygen, white spheres represent hydrogen. Translucent bonds represent hydrogen bonding interactions.

and adhesion are inherently coupled. By performing colloidal probe AFM measurements and integrating rheology, surface functionalization, and sorption kinetics experiments, we directly showed that the adhesion associated with interparticle hydrogen bonding couples with sliding resistance, leading to heightened friction that enhances both DST and SJ. This provides a new insight into the mechanistic picture of DST and SJ that has thus far been neglected in simulations.

Lastly, we took these results one step further and used them to engineer a system that is chemically designed to exhibit highly enhanced DST and SJ: silica particles with highly hydroxylated surfaces. We took advantage of the understanding from dry granular physics that particles of increased aspect ratio exhibit jamming at reduced concentrations. Therefore, we held the particle surface chemistry constant and tuned the aspect ratio of the resulting rods. Here we showed that by combining these effects, the concentrations required for DST and SJ can become staggeringly low: we showed DST at $\phi = 30.0\%$ and SJ at $\phi = 32.8\%$, which are concentrations low enough that they are sometimes not even considered to be "dense." Yet, the suspensions show significant DST and SJ, which is typically associated with much denser systems.

Overall, this work integrates the chemical perspective of solvated solid interfaces with granular and soft matter physics. With this approach we provide a fundamental, conceptual understanding for what governs the highly non-Newtonian flow behaviors of DST and SJ in dense suspensions. These findings provide a framework to anticipate and prevent unwanted flow behaviors in *e.g.* industrial processing applications, and contribute design recommendations for how to engineer DST and SJ at desired stresses and particle loadings for innovative, dynamically-responsive material applications.

6.2 Outlook

These contributions have addressed a bottleneck in studying shear jamming systems. Before this work, shear jamming was generally reserved to aqueous cornstarch suspensions.

Cornstarch is a delicate particle system because of its gelation, dissolution, and degradation properties. By investigating what contributes to cornstarch suspensions' ability to exhibit such strong shear jamming, we identified the important surface chemistry contributions so that we can now easily design shear jamming into new model systems.

In Chapter 5 we demonstrated how powerful this can be by studying the repercussions of particle shape on shear jamming using colloidally synthesized rods of variable length. In this direction, there are many further questions that can now be explored. For example: How can particle surface chemistry, shape, and roughness be combined to elicit DST and SJ at even lower particle loadings to facilitate protective material applications? How does particle size and shape dispersity affect the behavior? Is shear jamming possible in oily systems using other surface interactions such as pi stacking? Can a switchable system be developed where SJ behavior is activated through an external electric or magnetic field?

In addition to exploring the control parameter landscape, the ability to design pronounced, easily observable shear jamming into a variety of systems allows us to now target a fundamental attribute of the physics of this phenomenon: what sets the relaxation timescale of the shear thickened or jammed solid? The relaxation of shear jammed cornstarch suspensions has been observed [1], and the peculiarity of the relaxation timescales of the DST states in cornstarch suspensions has been reported [2]. To what extent do these relaxation timescales depend on the interparticle chemistry? How does it change between different particle systems? Can it be finely tuned by solvents?

Armed with the ability to intentionally design SJ into new systems, we can begin to answer these questions. The next few years promise to be very interesting.

BIBLIOGRAPHY

[1] Bin Liu, Michael Shelley, and Jun Zhang. Focused Force Transmission through an Aqueous Suspension of Granules. *Physical Review Letters*, 105:188301, 2010.

[2] Rijan Maharjan and Eric Brown. Giant deviation of a relaxation time from generalized Newtonian theory in discontinuous shear thickening suspensions. *Physical Review Fluids*, 2:123301, 2017.